Università degli Studi di Ferrara

DOTTORATO DI RICERCA IN
FISICA

CICLO XXVIII

COORDINATORE Prof. Guidi Vincenzo

From Dye to Hybrid Perovskite Solar Cells: Device and Material Investigation

Settore Scientifico Disciplinare FIS/01 Fisica Sperimentale

Dottoranda
Dott. Ivanovska Tanja

Tutore Interno
Prof. Guidi Vincenzo

Tutore Esterno
Dott. Ruani Giampiero

Anni 2012/2015

ACKNOWLEDGEMENTS

I would like to thank the Abdus Salam International Centre for Theoretical Physics for awarding me a TRIL Programme Fellowship at the Institute of Nanostructured Materials (ISMN) at the National Research Council (CNR) in Bologna, Italy, where the PhD research was performed. I would like to acknowledge further funding provided in the framework of the Progetto premiale CNR: Energia da Fonti Rinnovabili (EFOR).

I would like to thank my PhD supervisor Professor Vincenzo Guidi, for overviewing my work and guiding me through the doctorate school at the University of Ferrara. Furthermore, I would like to acknowledge Professor Alberto Quaranta and Dr. Isabella Concina for their review of the Thesis and their valuable comments and suggestions.

I am outmost grateful to my mentor Dr. Giampiero Ruani for giving me the opportunity to study, learn and develop as a researcher, investigating in the field of hybrid organic-inorganic solar cells and allowing me to broaden my knowledge and expertise in the field of vibrational spectroscopy. I am thankful for the trust, time, support and patience he demonstrated regarding both my professional and personal development during the years under his mentorship.

I would like to thank Dr. Chiara Dionigi, for all the valuable scientific contribution to my work, for all the knowledge that she transferred to me and especially for being an amazing support and friend in difficult times.

I would like to thank and acknowledge all the collaborators and colleagues that scientifically contributed to the work presented in the thesis. All the people from ISMN-CNR in Bologna, especially Dr. Margherita Bolognesi, Dr. Mario Prosa, Dr. Giovanni Donati, Dr. Mirko Seri, Dr. Stefano Toffanin and Dr. Michele Muccini, for their contribution to the light beam induced scanning techniques investigation. Dr. Caterina Soldano (ETC) for her help with the OCVD software and Paolo Mei and Vincenzo Ragona for all the technical support through the PhD research. I would like to thank Dr. Zoran Saponjic and Dr. Marija Radojcic from the Vinca Institute in Belgrade, Dr. Fabiola Liscio for the XRD analysis, Dr. Luca Ortolani, Dr. Vittorio Morandi and Dr. Franco Corticelli for the SEM investigations, from IMM-CNR Bologna. I would like to express gratitude for valuable scientific discussions and contribution to Dr. Giulia Grancini, Dr. Claudio Quarti, Dr. Edoardo Mosconi, Dr. Annamaria Petrozza and Dr. Filippo De Angelis. I would also like to thank Professor Hristina Spasevska for introducing me to the TRIL Programme and world of dye sensitized solar cells.

I am grateful to Susanna Cavallini and Marta Tessarolo for being wonderful friends and supportive colleges both scientifically and personally.

Last but not the least, thanks to my mom, grandparents and Ivo!

LIST OF PUBLICATIONS

Tanja Ivanovska, Zoran Saponjic, Marija Radoicic, Luca Ortolani, Vittorio Morandi and Giampiero Ruani, IMPROVEMENT OF DYE SOLAR CELL EFFICIENCY BY PHOTOANODE POST-TREATMENT. *International Journal of Photoenergy*, Volume 2014, Article ID 835760, 10 pages. doi:10.1155/2014/835760.

Chiara Dionigi, **Tanja Ivanovska**, Fabiola Liscio, Silvia Milita, Franco Corticelli and Giampiero Ruani, FABRICATION AND PROPERTIES OF NON-ISOLATING γ-ALUMINA MESO-FOAM. *Journal of Alloys and Compounds*, 2016, 666, 101-107. doi:10.1016/j.jallcom.2016.01.075.

Edoardo Mosconi, Claudio Quarti, **Tanja Ivanovska**, Giampiero Ruani and Filippo De Angelis, STRUCTURAL AND ELECTRONIC PROPERTIES OF ORGANO-HALIDE LEAD PEROVSKITES: A COMBINED IR-SPECTROSCOPY AND AB INITIO MOLECULAR DYNAMICS INVESTIGATION. *Physical Chemistry Chemical Physics*, 2014, 16, 16137. doi: 10.1039/c4cp00569d

LIST OF ABBREVATIONS

CB	conduction band
CuSCN	copper(I) thiocyanate
CIGS	copper indium gallium (di)selenide
CNT	carbon nanotubes
c.w.	continuous wave
CZTS	copper zinc tin sulfide
DSC	dye sensitized solar cell
E_f	Fermi level energy
E_g	band gap energy
FF	fill factor
FTO	fluorine doped tin dioxide
FWHM	full width half maximum
HCM	hole conducting material
HDPE	high density polyethylene
HOMO	highest unoccupied molecular orbital
I_{SC}	short circuit current
J_{SC}	short circuit current density
LBIC	laser beam induces photocurrent
LHE	light harvesting efficiency
LO	longitudinal optical
LSCM	laser scanning confocal microscopy
LUMO	lowest occupied molecular orbital
MAPI	methyl ammonium lead iodide
MWCNT	multi-wall carbon nanotubes
OCVD	open circuit voltage decay
OPV	organic photovoltaics
PCE	photon conversion efficiency
PL	photoluminescence
PSC	perovskite solar cell
PV	photovoltaic cell
QD	quantum dot
R_S	series resistance
R_{SH}	shunt resistance
S/V	surface/volume ratio
SDSC	solid state dye sensitized solar cell
SEM	scanning electron microscopy
SWCNT	single wall carbon nanotubes
TCO	tin conducting oxide
UV-Vis	ultra violet-visible
VB	valence band
V_{OC}	open circuit voltage
η	solar cell conversion efficiency

Table of Contents

CHAPTER I:

OBJECTIVES OF THE STUDY AND THESIS OUTLINE. INTRODUCTION AND BACKGROUND OF DYE SENSITIZED AND PEROVSKITE SOLAR CELLS.

1. Aim and Objectives of the Thesis

The principal research objective of the Thesis was based on experimental material and device investigation dedicated on further improvement of the dye sensitized solar cells and subsequently the perovskite solar cells.

Chapter I presents a short introduction to the incentive for solar cell research, brief overview of basics operational principle of the dye sensitized solar cell and optimization issues which lead to the development of the solid state dye sensitized solar cell and the perovskite solar cell.

Initially the Thesis investigation was focused on engineering of the TiO_2 photoanode for subsequent reduction of interfacial charge recombination and improvement of electron transport.

Two pathways were undertaken to achieve the photoanode optimization; reducing surface recombination by photoanode post-treatment and development of modified single wall carbon nanotube/TiO_2 photoanode.

Efficiency improvement of 10% by employing a simple photoanode post-treatment method for the dye sensitized solar cell was achieved. Furthermore, research into the photoanode modification, both implementing carbon nanotubes and post-treatment, was performed with respect to all three solar cell concepts investigated during the PhD research; dye sensitized solar cell, solid state dye sensitized solar cell and perovskite solar cell. Efficiency improvement with respect to reference devices was obtained for all cell types. The experimental methods for the photoanode and device preparation and characterization and the discussion of the obtained results are presented in **Chapter II**.

Further device investigation and optimization is focused on the perovskite solar cell and is presented in the next chapter, **Chapter III**. Investigation of the perovskite active material Cl-doped $CH_3NH_3PbI_3$ is presented in various solar cell configurations, by employing light induced scanning techniques. The dependence of the perovskite crystallization upon deposition on different photoanode scaffolds, as well as in planar configuration, is examined and discussed. The photovoltaic properties of low and high temperature processed planar perovskite solar cells were investigated. The obtained results indicate that the low temperature processed solar cell has negligible inferiority with respect to the high temperature processed counterpart. By utilization of light induced scanning techniques the aging process of the perovskite solar cell, varying different parameters upon device preparation, such as oxygen exposure and atmospheric conditions, is studied.

One of the most important issues for the optimization of the perovskite solar cell is in fact connected to the intrinsic properties of the methylammonium lead iodide $CH_3NH_3PbI_3$ material. To contribute in understanding of the physical mechanisms that determine the high mobility of both electron and holes in the same system as well as other fundamental optoelectronic properties of the perovskite material, a complete and profound study of the

$CH_3NH_3PbI_3$ vibrational properties was carried out. These novel results are presented in **Chapter IV** and currently represent new and unique insight into cation dynamics and phonon-phonon and electron-phonon interactions which are discussed in connection to possible implications on electron transport properties in solar cell devices.

The last, **Chapter V**, discusses the main results and important conclusions of the work presented in the Thesis, and sets an overview of further investigation and future prospects.

A short description and theoretical background of the main experimental techniques employed during the research presented in the Thesis can be found in the **Appendix** section.

The majority of the material and device preparation and characterization were performed at the Institute of Nanostructured Materials (ISMN) at the National Research Council (CNR) in Bologna. The synthesis of the TiO_2 nanoparticle colloidal solution was prepared by collaborators from the Vinca Institute in Serbia and the SEM and XRD measurements were conducted in collaboration with the Institute for Microelectronics and Microsystems (IMM-CNR) in Bologna.

All the work conducted at ISMN was performed by the PhD candidate. Specifically, all material and device preparation and electrical (I-V, OCVD and conductivity), and spectroscopic (optical UV-Vis and IR absorption, Raman and PL measurement) characterization, whereas, the candidate did not physically perform, however is competent and was directly involved in the preparation of O-benzyl tyrosine SWCNT dispersion, Al_2O_3 scaffold and the light induced scanning measurements.

2. Introduction

The global energy consumption in the world is rising every year with the increased scientific and technological development of humanity. The energy demand is exhausting the conventional energy sources (natural gas, coal and oil) and increasing the need for alternative *sustainable* power supply. Environmental studies in recent decades have shown that the increased energy consumption has a tremendous negative impact on the eco system of our planet due to CO_2 and particulate matter emissions endangering our very existence.[1,2] In order to control and ensure the development of all living beings on our planet, the power supply needs to be not only sustainable but moreover *environmentally friendly*. Sadly, due to the current global social-economic situation in the world, the "above all" characteristic of any new power source is to be *cost-efficient*.

Fortunately, the laws of physics granted us the possibility to exploit a potent power source, the *Sun*. The Sun which radiates electromagnetic energy, provides clean, sustainable, renewable and free energy available for us to harvest, transform and utilize for all means and applications.

Thus far, technologically, the solar energy can be collected and directly converted into two main forms of energy: thermal and electrical. Electrical energy is one of the principal energy forms used in everyday life. Conveniently easy to transport, convert and control it essentially "powers our civilization".

A photovoltaic or solar cell is a device for collection and direct conversion of solar into electrical energy. Currently the yearly world energy consumption is around 17.7 TW and the contribution of photovoltaic systems to the energy production in 2013 was 0.077%.[3] However, increased economical incentives and changing governmental policies have made

possible for the increase in the photovoltaic system installations to reach a capacity of 178 GW at the end of 2014, thus having the potential to supply 1% of the global energy demand.[4,5]

Even though the advances in the solar cell technology have managed to even the cost of electricity production from photovoltaics with electricity production from fossil fuels in certain regions of the world, still the major incentives for utilization of solar cells are the sustainability of the energy production and the reduction of CO_2 emissions. The trend in increasing the installation and utilization of photovoltaics has been particularly evident in the past 10 years and is predicted to continue; with certain forecast scenarios reporting between 400-700 GW installed capacity by 2020.[4,6] However, one of the key factors in these scenarios is advancing the photovoltaic technology by reducing the production price and increasing the efficiency of the solar cells.

3. Short History of Solar Cells

The starting point of conversion of light to electricity began with the discovery of the photovoltaic effect by Becquerel in 1839. He observed a continuous current from brass plates immersed in liquid after exposure to sunlight. In 1876 Adams and Day observed the photovoltaic effect in selenium in a "cell configuration". The first functional photovoltaic cell was constructed by Fritts in 1883 with the use of amorphous selenium. Another notable discovery in this period was the photoelectrochemical cell by Moser in 1887.[7,8]

It took almost a century for the modern era of photovoltaic to begin. The physics behind the solar cell technology of today needed to develop; from quantum mechanics, to single crystal semiconductor and p-n junction behavior. In 1954 researches in the Bell Laboratories in USA, discovered that the p-n junction of a diode generates voltage when exposed to light. A year later the first silicon solar or photovoltaic cell (PV) with 6% efficiency was reported.[9]

After more than 50 years of research and development of solar cell technologies a significant improvement of efficiency has been established. Latest certified efficiencies for single junction Si and GaAs solar cells reach above 35%.[10]

The evolution of the technology starts with crystalline Si solar cells which represent the first generation. These types of solar cells currently represent 90% of the market.[11] However technologically proven (efficiency of around 25% and stability of 20 years), silicon solar cells are heavy, brittle and most importantly have high energy consumption production.

The second generation of solar cells was developed to reduce the production cost by employing thin film technologies. These solar cells are based on amorphous silicon, CdTe and CIGS, reducing the quality and the amount of material. The thin film deposition technologies enable production of lighter and more flexible solar cells and propose similar efficiency and stability in comparison to the crystalline Si, for a lower price.[12,13] However, the initial estimations of cost reduction are not proving correct and the assumption that absorption of the active material can be improved to counteract the reduction in thickness and quality yields cells which are still not able to compete, efficiency wise, with the first generation technologies, resulting in market contribution of only 10% of this generation.

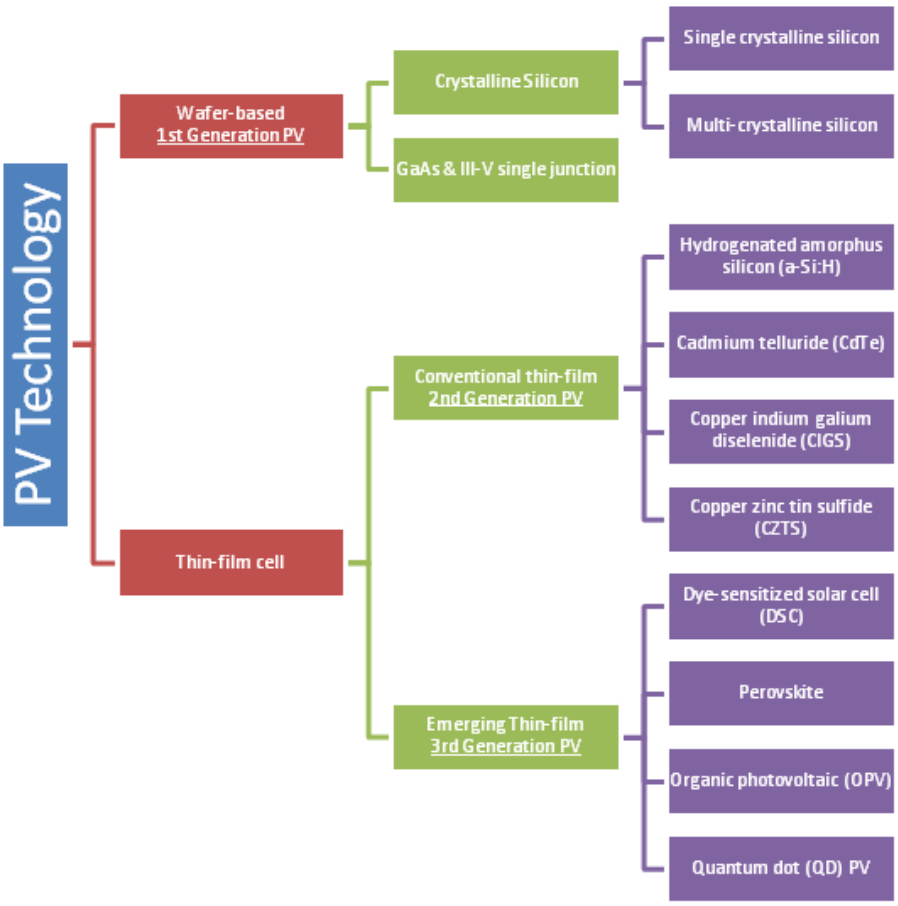

Figure 1. Schematic representation of the development of the PV technology.

3.1. Third Generation Solar Cells

Third generation of solar cell technologies emerged in the past 25 years from the imperative to solve both the cost and the efficiency deficits of the first and second generation PVs. The use of nanotechnology and organic semiconductor materials led to a development of organic photovoltaics, dye-sensitized solar cells and quantum dot solar cells (Figure 1). Additionally tandem and multijunction technologies based on second generation inorganic semiconductor materials, as well as, hybrid organic-inorganic concepts were developed.[12] Regardless of the significant production cost reduction by employing inexpensive materials, and materials such as nanocrystalline films and organic semiconductors, and low energy deposition techniques, the third generation hasn't managed to make a breakthrough in the PV market essentially due to two main problems: relatively low efficiency (10%) and long term stability issues.[14]

It is especially important to highlight that in the past four years the third generation of photovoltaics experienced a significant technological advance with the development of the perovskite solar cell.[15] The perovskite solar cells were designed as an evolutionary step of the dye sensitized solar cells and managed to skyrocket, efficiency wise, reaching a 20% efficiency in just few years.[16] Undoubtedly, the perovskite solar cells appear to be the most promising low cost solar cell technology of today, showing real potential to challenge the silicon solar cells on the market. The huge potential in the perovskite solar cell technology lies in the fact that is still very new and already huge advances were made in material engineering and device optimization. However, there is still a way to go before introducing the first commercial products on the market with the main issue being the stability of the

cell. One of the reasons is the novelty of this technology which is still much unexplored in the sense of the basic physical properties of the perovskite materials employed, which are currently one of the hottest research topics in the solar cell materials and devices community.

4. General Principles of Solar Cell Operation

4.1. Semiconductors

The basic electronic properties of inorganic semiconductors can be explained through the band theory. The allowed energy states for the electrons are represented through energy bands. The energy difference between the occupied band (valence) and the unoccupied band (conduction) is the band gap of the semiconductor. When electrons are excited through photon (light) absorption from the valence band (VB) to the conduction band (CB), both the electrons in the conduction band and the holes left behind in the valance band contribute to the electrical conductivity. In a direct absorption process a photon of energy $E_g = hv$, where h is the Planck's constant and v is the frequency of the photon, is absorbed by the crystal with the creation of an electron and a hole (Figure 2a). The indirect absorption process involves both a photon and a phonon because the band edges of the conduction and valence bands are widely separated in k space (Figure 2b). If a phonon is created (emitted) the energy of the incident photon needs to be greater than the true band gap E_g for the indirect process. However, at higher temperatures phonons are already present thus, if a phonon is absorbed along with a photon, the energy of the photon needed to create an electron and hole will be smaller than the E_g.[17]

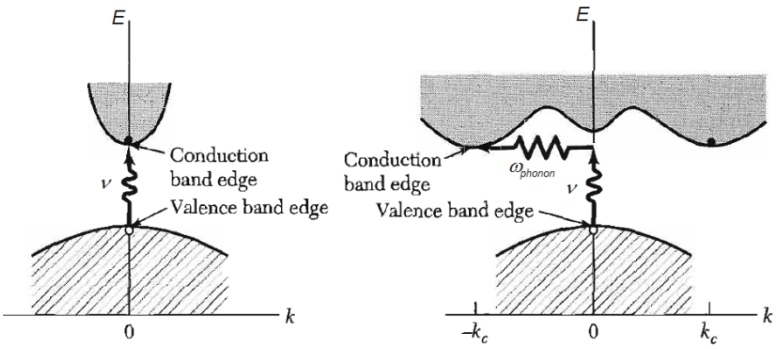

Figure 2. Schematic representation of a) direct absorption process; b) indirect absorption process.

Organic semiconductors are conjugated systems with a structure characterized by a sp^2 hybridized carbon atoms and un-hybridized p_z atomic orbitals. These atomic orbitals give rise to molecular σ and π electronic orbitals, respectively. The bonding (π) and antibonding (π^*) orbitals of molecules compose the valence and conduction bands of the organic semiconducting material, identified as the highest occupied and lowest unoccupied molecular orbitals respectively (HOMO and LUMO). In this case the charge transport process occurs by hopping between localized states rather than transport within a band. As a result the charge carrier mobility in organic semiconductors is smaller than that in inorganic semiconductors.

Another important difference in the charge generation between organic and inorganic semiconductors is that by photon absorption the inorganic semiconductor produces free electrons and holes, whereas photon absorption in organic semiconductors produces excitons, i.e. electron bound to a hole. The free charge pair needs to be produced by this neutral state. The charge separation is more difficult in organic semiconductors due to their low dielectric constant. Upon light absorption, molecules are excited from the ground state S_0 to an excited state S_1 (in the case of singlet transition). Singlet-singlet transitions are very efficient similar to direct transitions in inorganic semiconductors. They have short lifetime. They can go back to the ground state through luminescence or phonon emission. Therefore luminescence is a loss mechanism in photovoltaic cells. Another exciton decay channel is through a lower triplet state, which have an increased lifetime (μs) because they cannot deexcite radiatively, similar to indirect transition.[18]

4.2. Photovoltaic Effect and Solar Cell Operation

Solar cells are devices where basic operation is based on the physics of the photovoltaic effect and electron conductivity. When semiconductors are illuminated they generate free electrons and holes. Photons of specific energy are absorbed in the material and excite electrons which have enough energy to pass from the valence to the conduction band and create a hole in the valence band. The minimum energy that a photon needs to posses in order to promote an electron into the conduction band is equal to the energy of the band gap. Once the charge is separated it needs to be collected by selective contacts and transported to the external circuit before it recombines. A simplified scheme of the photovoltaic conversion is reported in Figure 3.

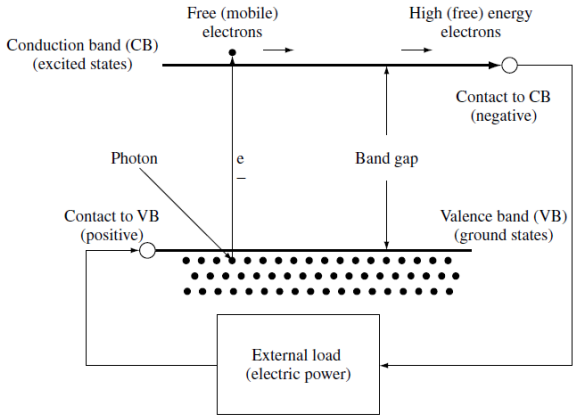

Figure 3. Scheme of photovoltaic conversion.[9]

The manner by which the charge is separated and transported depends on the solar cell technology; the former depends on whether we are discussing an organic or inorganic semiconductor.[9]

4.3. Solar Cell Parameters

The basic parameters of a solar cell can be defined with the help of an equivalent circuit as represented in Figure 4.

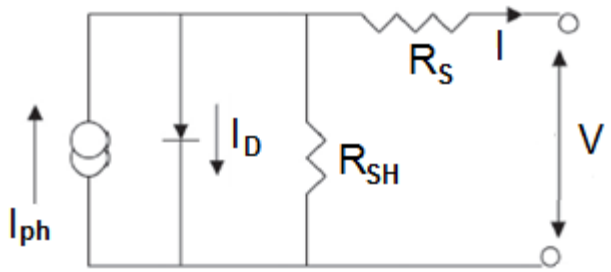

Figure 4. One diode equivalent circuit of solar cell operation.

The ideal solar cell in the dark can be interpreted as a diode. Connected to an external load a potential difference is created and the current generated through the diode I_D is described by the Shockley diode equation.

$$I_D = I_0\left\{\exp\left[\frac{qV_D}{nk_bT}\right]-1\right\} \tag{1}$$

where I_0 is the diode saturation current, q is the elementary charge, V_D is the potential difference at the diode terminals, n is the ideality factor of the diode, k_b is the Boltzmann constant and T is the absolute temperature.

However, when a solar cell is illuminated the photogenerated current I_{ph} has opposite direction than the dark diode current and the net current generated by the solar cell I will be:

$$I = I_{ph} - I_D \tag{2}$$

As in every real electrical circuit, certain internal resistive elements will dissipate the final power output thus we have to take into account also the elements of series R_S and parallel (shunt) resistance R_{SH},[19] which according to the equivalent circuit in Figure 4 results in the following equations:

$$V_D = V + IR_S \tag{3}$$

$$I = I_{ph} - I_0\left\{\exp\left[\frac{q(V+IR_S)}{nk_bT}\right]-1\right\} - \frac{V+IR_S}{R_{SH}} \tag{4}$$

where V is the solar cell voltage. When a cell is connected to an infinite resistance i.e. open circuit conditions the potential difference generated at the contacts is called open circuit voltage V_{OC}. In this situation no current flows through the solar cell. If we suppose that the parallel resistance is high enough, we can neglect the last part of equation 4 and the V_{OC} is equal to:

$$V_{OC} \approx \frac{k_bT}{q}\ln\left(\frac{I_{ph}}{I_0}+1\right) \tag{5}$$

Generally in single junction inorganic solar cells the V_{OC} is roughly determined by the band gap of the absorbing semiconductor, however this approximation is limited by recombination of charges through radiative processes, as firstly hypothesized by Shockley and Queisser in 1961.[20]

5. Dye Sensitized Solar Cells

The dye sensitized solar cell (DSC or dye cell) represents a third generation photovoltaic cell based on a mesoscopic network of interconnected organic and inorganic semiconductors. The DSC was invented at the Ecole Polytechnique Federale de Lausanne in 1991 by Gratzel and O'Regan and the discovery was published in Nature the same year.[21] The dye sensitized solar cell is a unique photovoltaic concept which incorporates nanocrystalline inorganic semiconductors, organic dyes and semiconductors and ionic liquids, thus for the first time the basic concept of a semiconductor junction was left behind and a specific organic-inorganic solar cell with a liquid component was constructed.

Several attractive properties of the construction and application of the DSC concept secured a milestone in the research of the dye cell in the past 20 years. Mainly the use of abundant materials with low purification and the low energy-consumption manufacturing process made possible for a low cost production. The materials and deposition methods enabled compatibility with different types of substrates, which expanded the possibilities for application. The large utilization possibilities arose due to the option to prepare the cells in variety of shapes and colors.[22] Several companies such as MKE, Fujikura and G24 have already commercialized products for indoor application as well as small powering solutions such as phone chargers. The specific optoelectronic characteristics and morphology of the DSC are suitable for implementation in large window integrated transparent modules, such as the facade of the Swiss-Tech Convention Center in Lausanne Switzerland which is entirely covered with an electricity producing glass made of dye cells.

5.1. DSC Advantages and Disadvantages

The market advantages of the DSC clearly lie in the low cost production and easy up-scaling of the production process, which doesn't require specific production line, instead can be easily modified from printing techniques. Their incorporation into interior and exterior makes them additionally attractive for the end consumer. The ability to work in diffuse light conditions from the engineering point of view contributes to the appeal of these cells for building integrated applications and continues to fuel up scientific interest into further improvement of the DSC technology.[23]

Despite several small commercially available market applications, the DSC hasn't lived up to its potential. As previously mentioned the main reason is the stability of the dye cell. Despite the relatively low efficiency achieved for submodule applications in comparison to Si technology,[24] these cells can still have a market impact for applications that tradeoff high efficiency for commodity. However, the stability problem significantly reduces the lifetime prognosis for the cells, essentially labeling them a high risk investment. The two essential points to review when discussing the improvement of the DSC are:

- Efficiency improvement
- Long term stability under atmospheric conditions – solid electrolyte.

5.2. Construction and Operational Principle

The basic construction scheme is reported in Figure 5. The DSC is constructed with two glass electrodes coated with a crystalline conducting layer of fluorine doped tin dioxide (FTO). One of the electrodes is covered with a mesoporous film of titanium dioxide TiO_2 and represents the photoanode of the dye cell. The photoactive material is an organic dye adsorbed on top of the mesoporous titania. The second FTO glass is covered with a thin film of platinum and represents the counter electrode. This "sandwich type" design is than filled with liquid electrolyte and sealed with a transparent plastic film.

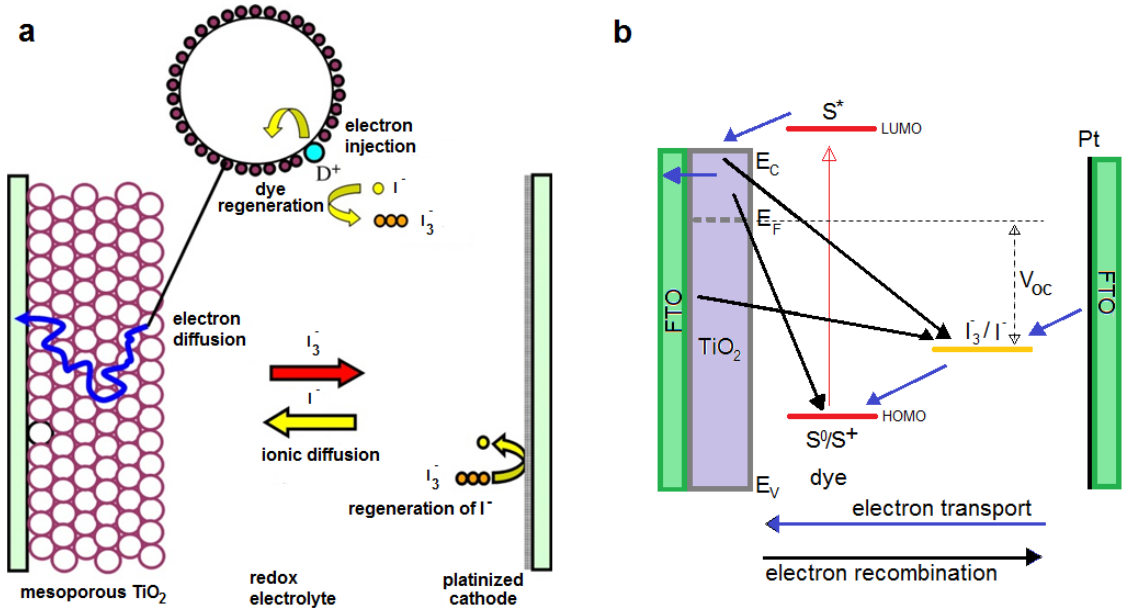

Figure 5. a) Scheme of construction and basic operation of DSC;[25] b) energy diagram, excitation and recombination processes in DSC.

The operation principle of the dye cell can be reviewed through a simple energetic diagram as presented in Figure 5b. The light falls and passes through the photoanode and is absorbed by the dye molecules. Since TiO_2 is a wide band gap semiconductor ($E_g > 3.2$ eV) the photoanode is essentially transparent in the visible part of the solar spectrum. The absorbed photon excites the dye molecule from the ground S to an excited state S^*:

$$S + h\nu \rightarrow S^* \tag{6}$$

In the excited state the molecule oxidizes by injecting electrons in to the conduction band of the TiO_2.

$$S^* \rightarrow S^+ + e^- \tag{7}$$

The electrons are transported through the nanoparticles of the TiO_2 to the FTO and into the external circuit. Meanwhile the oxidized state S^+ of the dye returns to the ground state by accepting an electron from the electrolyte.

$$S^+ + e^- \rightarrow S \tag{8}$$

At the same time the iodide is stripped from an electron and oxidizes into triiodide:

$$3I^- - 2e^- \rightarrow I_3^- \tag{9}$$

which diffuses to the counter electrode and by accepting an electron regenerates into iodide.

$$I_3^- + 2e^- \rightarrow 3I^- \quad (10)$$

This process forms a closed, fully regenerative electrical cycle of a direct conversion of solar to electrical energy without any permanent chemical transformation.[26]

The specific construction of the DSC enables minimization of the solar cell thickness by employing nanocrystalline mesoporous material, and in turn, maximization of the effective active surface which significantly increases the light harvesting efficiency (LHE). Contrary to first and second generation solar cells based on a p-n junction, in the dye cell the two basic mechanisms of solar cell operation, the optical absorption and the charge separation and transport, are separated.

The basic operational principle of the DSC is based on four energy levels of the system components (Figure 5b); the HOMO and LUMO levels of the dye, the Fermi level (E_F) of the TiO_2 and the redox potential of the iodide/triiodide redox couple in the electrolyte. The photocurrent generated from the dye cell is determined from the energy difference between the HOMO and LUMO levels of the dye. The smaller energy gap between the levels ensures absorption of low energy photons from the solar spectrum. The energy difference between the LUMO and the Fermi level is essential since the LUMO has to be higher in order to effectively inject electron into the conduction band of the TiO_2, whereas the HOMO has to be lower compared the redox potential of the electrolyte to ensure effective electron acceptance. An appropriate electronic pairing of the LUMO and the Fermi level leads to effective electron injection.[26,27]

5.3. Charge Recombination Dynamics

The operational mechanism of charge separation and transport in the dye solar cell is subjected to a dynamical competition. The electron injection in the TiO_2 is a fast process happening on a picosecond scale, however the dye regeneration process is few orders of magnitude slower thus giving opportunity for the injected electron to recombine with the oxidized state of the dye. Even though this reaction for certain dyes is quite slow at short circuit conditions (μs-ms), as the potential increases this process speeds up and at open circuit conditions all carriers recombine through each of the 3 main mechanisms as depicted in Figure 5b.

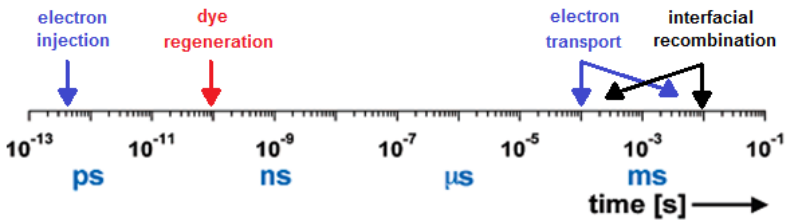

Figure 6. Time scale of charge transport and regeneration processes.

The other two main recombination mechanisms relate to the electrolyte. Figure 6 represents the timescale on which the recombination and transport process occur. Namely, electrons can recombine with the electrolyte both though the TiO_2 and the FTO layers of the photoanode.[28] The former case is affected by the large active surface of the mesoporous TiO_2 film which is in contact with the electrolyte due to insufficient coverage by the dye molecules. Contributing factor is also the reduced diffusion coefficient of the electrolyte ions within the pores of the TiO_2 film, which are not able to diffuse to the counter electrode

and regenerate fast enough. The latter recombination reaction is a direct result of a large electron concentration on the substrate surface with respect to the TiO_2.[29] The relative rate of these reactions will depend of the chemical composition of the electrolyte.

If we review these two reactions taking into account the equivalent circuit schematics of a solar cell (Figure 4), the electron recombination corresponds to parallel resistive elements i.e. shunt resistance. Higher reaction rate reduces the shunt resistance and in turn reduces the cell efficiency.

5.4. Efficiency Improvement

The efficiency improvement of the dye cell can be addressed from several viewpoints. The main steps are to increase the LHE, increase the efficiency of the electron transport and reduce the electron recombination. Increasing the LHE can be accomplished either through increasing the active area of the photoanode or by employing dyes with broader absorption intervals. On the other hand, promoting the electron transport and reducing the recombination can be achieved by carefully combining or engineering semiconductors and organic components (dye and electrolyte) for a superior energy level alignment (Fermi level, HOMO and LUMO of the dye and the redox potential). In the case of the dye cell the potential difference between the Fermi level and the redox potential determines the maximum open circuit voltage of the system. As mentioned previously the optimal energy level differences for efficient charge separation require that both E_g - LUMO and HOMO - redox potentials to differ by at least 200 mV, furthermore the HOMO-LUMO difference needs to be as small as possible to insure absorption of larger wavelengths in the infrared. The Fermi level of the inorganic semiconductor depends on the electrolyte components and their concentration, and thus it is evident that with careful molecular modeling and chemical manipulation both the dye and the electrolyte can be engineered to ensure efficiency improvement.

Another way to think is not only of improvement and engineering of new DSC elements but of enhancing the already established system. Improving the charge transport through the TiO_2, and photoanode modification can significantly reduce the recombination of the electrons with the electrolyte. The advances in efficiency improvement, as in optimization of any energy production device, are based on continuous research and development of all DSC elements. Numerous publications are made on modification of electrodes, mesoporous photoanode film, sensitizers and electrolytes. Each of these specific research lines has contributed to significant versatility of dye solar cell devices (regarding flexibility, color, liquid-solid state and efficiency).[30]

5.5. Stability Improvement

One of the major disadvantages of the DSC in up-scaling and taking a significant market contribution is the instability of the liquid component.[31] Even though the unique construction properties enable effectively the charge separation and transport to occur in different materials, the inclusion of the liquid electrolyte causes serious problems for industrialization. The sealing process becomes particularly challenging since it needs to prevent evaporation and leakage of the electrolyte under various atmospheric conditions, further more the electrolyte needs to be chemically stable under extreme temperatures (high and low) and ultraviolet radiation. Considering the suitable design of the solar cell and its advantages, instead of abandoning the concept, efforts are made not only to

engineer a stabile liquid component but moreover to replace the liquid electrolyte with polymer gel electrolytes, solid electrolytes and solid polymeric hole conductive materials.[32–34] Introducing solid organic semiconductors resulted in a new breed of dye cell, the so called solid state dye sensitized solar cell (SDSC).[35]

6. Solid State Dye Sensitized Solar Cells

One of the basic approaches in exchanging the liquid electrolyte in the construction of a functional dye cell is to implement a material which is an effective hole conductor. Generally the choice of material has to be bounded by certain properties:

- It has to posses structural properties which will allow for certain methods of deposition in order to achieve effective interconnection and coverage of the sensitized mesoporous TiO_2 photoanode film.
- The deposition method has to ensure that there will be no chemical degradation of the dye molecules.
- The material has to be transparent in the visible part of the spectrum (to prevent competition for light absorption with the dye). If there is certain absorption, the kinetics of the hole transport from the dye to the hole conducting material (HCM) has to be at least in the same order of magnitude as the injection of the electron from the dye into the TiO_2.
- Support the concept of low cost fabrication and energy consumption.
- Posses "electronic" compatibility with the rest of the SDSC components.

All these characteristics are applicable to a variety of organic semiconductor materials.[36] Their deposition can be solution processed to ensure interconnection and coverage of the mesoporous film, the deposition techniques such as spin coating or blade casting are low cost and low energy techniques and the kinetics of hole transport through dye/HCM interface can be at least one order of magnitude faster than that of the iodide/triodide redox couple.

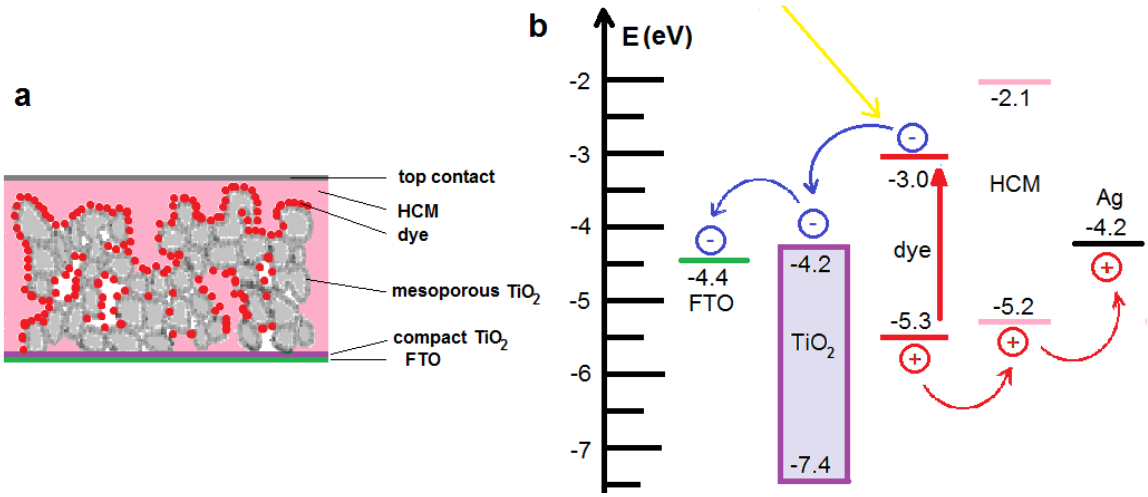

Figure 7. Schematic representation of SDSC; a) cross section of a solar cell; b) energy level alignment and charge transport (the HOMO/LUMO values depicted correspond to the N719 dye and the spiro-OMeTAD HCM).

The operational principle of the solid state dye cell remains in essence, the same;[37] however it is important to note that the charge transport is fundamentally different, diffusion controlled ionic transport in the DSC vs. electronic transport governed by conductivity and charge mobility in the SDSC.[38] One has to additionally take into consideration the electronic levels of the semiconductor or hole conducting material, and their alignment with respect to the HOMO/LUMO of the dye. A schematic representation of the cross section of a SDSC, and the energy level alignment and general charge transport pathways are presented in Figure 7**.**

Parallel to the research of the liquid dye cell another strong branch of investigation is focused on the solid state dye cell. Drawing experience from other thin film concepts as well as organic photovoltaics, the development of the SDSC led to the construction of efficient devices. The most utilized HCM with highest published efficiencies for the solid state cells are spiro-OMeTAD and CuSCN and CuI.[39] The main issue in these devices is poor infiltration and contact of the HCM to the photoanode matrix. Increasing the infiltration of the HCM in the TiO_2 matrix is one of the basic physical requirements.[40] However this proved to be a major setback. For the spiro-OMeTAD reducing the viscosity of the polymer solution in order to increase infiltration resulted in reduced hole conducting properties. A tradeoff between concentration and infiltration was made which lead to significant decrease of TiO_2 photoanode thickness to only a few microns. This represents a major reduction in active area and consequently light absorption. Therefore, the efficiency of these devices never reached the liquid device (to date the most efficient SDSC is around 7%).[41] Although, the reactions of charge separation and transport are favorable, this solid state concept is prone to high recombination due to insufficient contact between the hole conductor and the sensitized photoanode. To decrease the recombination several steps are reviewed, such as: reducing the interfacial recombination between the TiO_2 and the HCM and increasing the conductivity of both the electron and hole conductors.

7. Perovskite Solar Cells

The efficiency improvement of DSC can be obtained by employing suitable sensitizing materials, with high absorption coefficients in the visible and especially in the near infrared region, with respect to the available terrestrial solar radiation. In 2009 Kojima and coworkers used a hybrid organic-inorganic perovskite materials, methylammonium lead iodide $CH_3NH_3PbI_3$ and methylammonium lead bromide $CH_3NH_3PbBr_3$ as light absorbing materials and reported of DSC with conversion efficiency of 3.8% for the iodine based perovskite, and a high photovoltage of 0.96 V was obtained for the bromide based perovskite.[42] However, this concept didn't rise to fame due to the relatively low efficiency (the record efficiency for DSC is already established at around 11%).[24] In 2011 this concept was revisited by Im *et al*. reporting on a perovskite quantum dot sensitized device of 6.5% efficiency, even though this was a significant improvement, these type of materials are ionic crystals which when in contact with polar liquid based electrolytes are highly prone to degradation.[43] Considering this, it became obvious that liquid dye cells were not the suitable solar cell concept, on the other hand the high absorption coefficient of the $CH_3NH_3PbI_3$ which was reported to be 10 times higher than that of standard ruthenium based dyes, intrigued the research community in incorporating this material into a solution processable solid state dye solar cell concept.

Park's group was the first to publish a solid state perovskite sensitized device in 2012 with astonishing efficiency of 9,7%.[41] The same year Lee *et al*. reported on a Cl doped

$CH_3NH_3PbI_3$ deposited on a dielectric Al_2O_3 mesoporous scaffold reaching 10.9%.[44] After this publication the photovoltaic community became the living witness to the fastest efficiency rise of a solar cell technology, which established itself as a separate solar cell technology within the 3rd generation PVs, the perovskite solar cells (PSC).

In the following three years up to date there have been significant advances both in device and material optimization as well and fundamental material research and investigation. Due to the convenient band gap energy and device efficiency the $CH_3NH_3PbI_3$ and its chlorine doped counterpart emerged as the leading perovskite materials for solar cell application, however high efficiency devices were reported for both TiO_2 and Al_2O_3 photoanode scaffolds which prompted investigation in to essential charge generation, separation and transport of the material. Investigation showed good mobilities and long diffusion lengths for both electrons and holes;[45] the electron diffusion length of Cl-doped $CH_3NH_3PbI_3$ reaching 1 µm.[46] The ambipolarity of these materials suggested that a planar perovskite (p-i-n) junction device would be able to achieve high conversion efficiencies which prove to be correct.[47] The architecture evolution of the perovskite solar cell is illustrated in Figure 8.

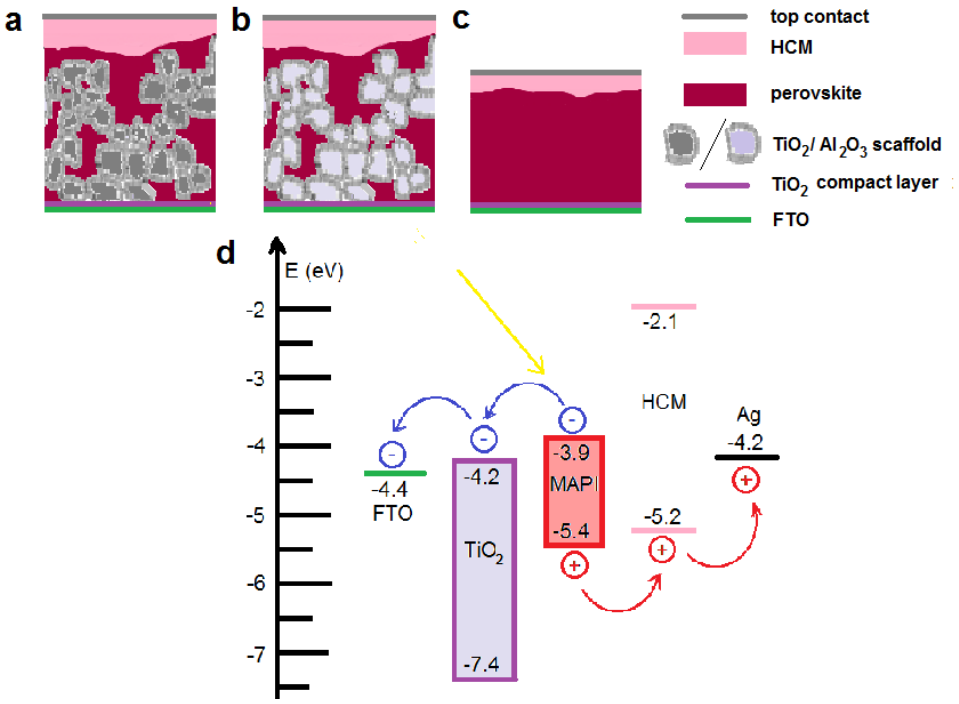

Figure 8. Top part: Structural evolution of the perovskite solar cell to date; cross section of PSC in a) mesoporous configuration (TiO_2 scaffold); b) meso-superstructured configuration (Al_2O_3 scaffold); c) planar configuration (no scaffold). Bottom part: d) Schematic representation of energy level alignment and charge transport in PSC employing TiO_2 and methylammonium lead iodide (MAPI) and spiro-OMeTAD. Note that in all three cases TiO_2 compact layer is present, thus, although in the meso-superstructured solar cell there is no injection of the electron in the scaffold, the electron transport still occurs through a thin TiO_2 layer.

The fascinating optoelectronic properties of the $CH_3NH_3PbI_3$ (and Cl-doped $CH_3NH_3PbI_3$) gave rise to fast efficiency improvement for every device concept employing this active material, currently reaching 20.1% (see Figure 9a).[24] However, the above mentioned device concepts have different charge transport kinetics, which in turn suggested that the material properties governing the device efficiency "boom" were poorly understood. While the research was initially focused on efficiency improvement by optimizing device structure, taking into account different mesoporous scaffolds and hole conducting

materials, in parallel, fundamental research into the material properties began to rise (Figure 9b). The $CH_3NH_3PbI_3$ has been successfully incorporated on flexible substrates,[48] into existing organic photovoltaic technologies and further more tandem solar cells have already been reported.[49] The research of the material led to applications in light emitting diodes and transistors,[50,51] and initial lasing prospects.[52]

Several characterization results have been quite puzzling for interpretation.

The structural properties of the perovskite active material prove to be essential for operation regardless of the device architecture.[53,54] The crystallization dynamics and grain boundaries of the perovskite active layer instigated research in several deposition methods from single and two step sequential spin and dip coating techniques to vapor deposition and evaporation methods.[55] Furthermore the deposition method greatly influences formation of traps and defects whose contribution has yet to be qualitatively explained.

The current voltage response of the perovskite solar cell under illumination shows a hysteresis behavior with respect to forward (I_{SC} to V_{OC}) and backward (V_{OC} to I_{SC}) scan, additionally the *I-V* response depends on scan rate as well as on pre-measurement conditions such and light soaking and constant bias.[56] Two main theories have been proposed to be responsible for this behavior, one is a ferroelectric polarization of the working device and the other has been connected to ion migration with the latter gaining more scientific evidence in recent months.

As in any new material and technological concept there is still much to learn.

Charge career dynamics of the $CH_3NH_3PbI_3$ are still being rigorously studied to provide a more complete understanding of the solar cell device photophysics.[57] Within the past year more attention has been focused on the vibrational properties as a key to unlocking phonon and charge interaction and coupling effects as basics in explaining several material and device phenomena such the long diffusion length and long charier lifetime, relatively good mobilities despite the unavoidable presence of defects/traps, the low electron−hole recombination rates which are in the order of magnitude of some of the best are single-crystalline inorganic semiconductors,[58] the hysteresis behavior in the current voltage characteristics, the high dielectric constant, as well the possible presence of spontaneous polarization and ferroelectricity due to the specific material structure.[59]

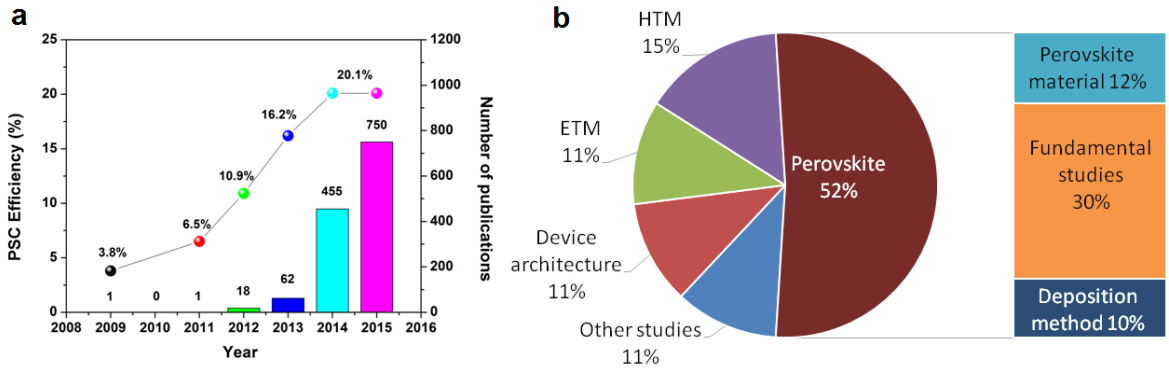

Figure 9. a) Increase of number of publication with respect to increase in reported efficiency of perovskite solar cells in the past 6 years.[55] In 2015 according to a key word search "perovskite solar cells" on web of science the number of publications is 750; b) Interest in different research topics according to published articles.[60]

This technology has reached certain maturity in device preparation and optimization which has inevitably led to establishing the next technological step towards scaling up and industrialization.

Most recent cost estimations for the market production of the perovskite solar cells employing spiro-OMeTAD as HCM reach a cost of 0.3USD per peak Watt taking into consideration only the cost of the material (the majority going to organic semiconductors). Even though the current market price of the Si and CdTe solar cells reach a market low of 0.3USD per peak Watt, estimations of perovskite solar cells employing specific low-cost organic semiconductors reach remarkable material cost contribution of only 0.004 W_p^{-1} in the final device.[61] Furthermore employing Si/perovskite tandem cell has proven to enhance the efficiency of the standalone devices by 50%,[62] thus estimating the prices of technologies utilizing perovskite solar cells to drop as low as 0.2-0.1USD per W_p.[63]

However, as for any third generation PV technology, the question of the perovskite solar cell, i.e. perovskite material, stability rises. Due to the structure of the $CH_3NH_3PbI_3$ it has already been shown that high humidity atmospheric conditions are fast degrading the material, and with it the device,[64,65] however an encapsulated device essentially has the potential to meet the operational standards of commercially available solar cells. It must however be pointed out that the device stability under full sunlight operational conditions is far different from the chemical stability of a standalone (or even in device configuration) perovskite material. Extensive research in this field is currently undergoing not only on a laboratory scale, but also on an industrial scale in several newly formed companies such as Oxford Photovoltaics.

Another serious concern towards industrialization is the environmental impact of the lead component, thus efforts have been made in replacing the Pb with Sn and other potentially non-toxic metals for optoelectronic applications.[66,67] Several environmental studies have already been published on the possible toxicity form the Pb based perovskite materials,[68,69] as well as non encapsulated PSC.[70] However, having in mind that CdTe solar cells have been commercially available for more than 10 years, and even though environmental concerns exist due to the toxicity of the CdTe material,[71] studies have shown that sealed devices show no leaching.[72] Regardless of already existing technologies, the introduction of the Pb-based perovskite solar cells need to be further investigated.

The distinctive properties of the methylammonium lead iodide for solar cell application and the superior power conversion efficiency within light absorbing materials employed in the 3rd generation PVs, outweigh the possible technological setback issues and not only withhold the $CH_3NH_3PbI_3$ in the research focus, but generate further interest in the material and the perovskite solar cells.

8. Bibliography

1. McGlade, C. & Ekins, P. The geographical distribution of fossil fuels unused when limiting global warming to 2°C. *Nature* **517,** 187–190 (2015).
2. Pieprzyk, B., Kortluke, N. & Rojas Hilje, P. *The impact of fossil fuels*. *Bee* (2009).
3. REN21. *Renewables Global Status Report 2014*. (2014). at <http://www.ren21.net/wp-content/uploads/2015/07/GSR2015_KeyFindings_lowres.pdf>
4. Solar Power Europe. *Global Market Outlook for Solar Power 2015-2019*. (2014).
5. IEA. *Snapshot of Global PV Markets 2014, Report IEA PVPS T1-26:2015*. (2015). at <http://www.iea-pvps.org/fileadmin/dam/public/report/technical/PVPS_report_-_A_Snapshot_of_Global_PV_-_1992-2014.pdf>
6. Growth of photovoltaics - Wikipedia, the free encyclopedia.
7. Gratzel, M. & Durrant, J. R. in *Nanostructured and Photoelectrochemical Systems for Solar Photon Conversion* 503–536 (2008). doi:10.1142/9781848161542_0008
8. Fraas, L. & Partain, L. in *Solar Cells and their Applications* 1–15 (John Wiley & Sons, Inc., 2010). doi:10.1002/9780470636886.ch1
9. Hegedus, S. S. & Luque, A. in *Handbook of Photovoltaic Science and Engineering* (eds. Luque, A. & Hegedus, S.) **1,** 1–43 (John Wiley & Sons, Ltd, 2005).
10. NREL. *Efficiency_Chart*. *Nrel* (2015). at <http://www.nrel.gov/ncpv/images/efficiency_chart.jpg>
11. IEA. *Technology Roadmap Solar Photovoltaic Energy*. *IEA* (2014). at <http://www.springerreference.com/index/doi/10.1007/SpringerReference_7300>
12. Jayawardena, K. D. G. I. *et al.* 'Inorganics-in-Organics': recent developments and outlook for 4G polymer solar cells. *Nanoscale* **5,** 8411 (2013).
13. Bagher, A. M., Vahid, M. M. A. & Mohsen, M. Types of Solar Cells and Application. *Am. J. Opt. Photonics* **3,** 94–113 (2015).
14. Elliott, C. M. Dye-sensitized solar cells: Out with both baby and bathwater. *Nat. Chem.* **3,** 188–189 (2011).
15. Snaith, H. J. Perovskites: The Emergence of a New Era for Low-Cost, High-Efficiency Solar Cells. *J. Phys. Chem. Lett.* **4,** 3623–3630 (2013).
16. He, X. Perovskite photovoltaics: current status and outlook. *Transl. Mater. Res.* **2,** 030301 (2015).
17. Kittel, C. in *Introduction to Solid State Physics 8th Edition* (ed. Stuart, J.) 185–220 (John Wiley & Sons, Inc., 2005).
18. Bernede, J. C. Organic Photovoltaic Cells: History, Principle and Techniques. *J. Chil. Chem. Soc.* **53,** 1549–1564 (2008).
19. Nelson, J. in *The Physics of Solar Cells* 1–16 (Imperial College Press (Distributed by World Scientific Publishing Co.), 2003). doi:10.1142/9781848161269_0001
20. Shockley, W. & Queisser, H. J. Detailed Balance Limit of Efficiency of p-n Junction Solar Cells. *J. Appl. Phys.* **32,** 510 (1961).
21. O'Regan, B. & Grätzel, M. A low-cost, high-efficiency solar cell based on dye-sensitized colloidal TiO_2 films. *Nature* **353,** 737–740 (1991).
22. Ebrahim, K. in *Solar Cells - Dye-Sensitized Devices* (InTech, 2011). doi:10.5772/19749
23. Kawakita, J. Trends of research and development of dye-sensitized solar cells. *Sci Technol Trends* **35,** 70–82 (2010).
24. Green, M. A., Emery, K., Hishikawa, Y., Warta, W. & Dunlop, E. D. Solar cell efficiency tables (version 46). *Prog. Photovoltaics Res. Appl.* **23,** 805–812 (2015).
25. Peter, L. M. Towards sustainable photovoltaics: the search for new materials. *Philos. Trans. R. Soc. A Math. Phys. Eng. Sci.* **369,** 1840–1856 (2011).

26. Grätzel, M. in *Thin Film Solar Cells* **1,** 363–385 (John Wiley & Sons, Ltd, 2006).
27. Boschloo, G. & Hagfeldt, A. Characteristics of the Iodide/Triiodide Redox Mediator in Dye-Sensitized Solar Cells. *Acc. Chem. Res.* **42,** 1819–1826 (2009).
28. Grätzel, M. Solar Energy Conversion by Dye-Sensitized Photovoltaic Cells. *Inorg. Chem.* **44,** 6841–6851 (2005).
29. Gregg, B. A., Pichot, F., Ferrere, S. & Fields, C. L. Interfacial Recombination Processes in Dye-Sensitized Solar Cells and Methods To Passivate the Interfaces. *J. Phys. Chem. B* **105,** 1422–1429 (2001).
30. Ye, M. *et al.* Recent advances in dye-sensitized solar cells: from photoanodes, sensitizers and electrolytes to counter electrodes. *Mater. Today* **18,** 155–162 (2015).
31. Sauvage, F. A Review on Current Status of Stability and Knowledge on Liquid Electrolyte-Based Dye-Sensitized Solar Cells. *Adv. Chem.* **2014,** 1–23 (2014).
32. Dong, R.-X. *et al.* A novel polymer gel electrolyte for highly efficient dye-sensitized solar cells. *J. Mater. Chem. A* **1,** 8471–8478 (2013).
33. Wu, J. *et al.* Progress on the electrolytes for dye-sensitized solar cells. *Pure Appl. Chem.* **80,** (2008).
34. Han, L., Wang, Y. F. & Zeng, J. H. Effective Solid Electrolyte Based on Benzothiazolium for Dye-Sensitized Solar Cells. *ACS Appl. Mater. Interfaces* **6,** 22088–22095 (2014).
35. Nanu, M., Schoonman, J. & Goossens, A. Inorganic Nanocomposites of n- and p-Type Semiconductors: A New Type of Three-Dimensional Solar Cell. *Adv. Mater.* **16,** 453–456 (2004).
36. Leijtens, T. *et al.* Hole Transport Materials with Low Glass Transition Temperatures and High Solubility for Application in Solid-State Dye-Sensitized Solar Cells. *ACS Nano* **6,** 1455–1462 (2012).
37. Karthikeyan, C. S. & Thelakkat, M. Key aspects of individual layers in solid-state dye-sensitized solar cells and novel concepts to improve their performance. *Inorganica Chim. Acta* **361,** 635–655 (2008).
38. Peng, B. *et al.* Systematic investigation of the role of compact TiO_2 layer in solid state dye-sensitized TiO_2 solar cells. *Coord. Chem. Rev.* **248,** 1479–1489 (2004).
39. Yum, J.-H., Chen, P., Grätzel, M. & Nazeeruddin, M. K. Recent Developments in Solid-State Dye-Sensitized Solar Cells. *ChemSusChem* **1,** 699–707 (2008).
40. Melas-Kyriazi, J. *et al.* The Effect of Hole Transport Material Pore Filling on Photovoltaic Performance in Solid-State Dye-Sensitized Solar Cells. *Adv. Energy Mater.* **1,** 407–414 (2011).
41. Kim, H. *et al.* Lead Iodide Perovskite Sensitized All-Solid-State Submicron Thin Film Mesoscopic Solar Cell with Efficiency Exceeding 9%. *Sci. Rep.* **2,** 1–7 (2012).
42. Kojima, A., Teshima, K., Shirai, Y. & Miyasaka, T. Organometal Halide Perovskites as Visible-Light Sensitizers for Photovoltaic Cells. *J. Am. Chem. Soc.* **131,** 6050–6051 (2009).
43. Im, J.-H., Lee, C.-R., Lee, J.-W., Park, S.-W. & Park, N.-G. 6.5% efficient perovskite quantum-dot-sensitized solar cell. *Nanoscale* **3,** 4088 (2011).
44. Lee, M. M., Teuscher, J., Miyasaka, T., Murakami, T. N. & Snaith, H. J. Efficient Hybrid Solar Cells Based on Meso-Superstructured Organometal Halide Perovskites. *Science.* **338,** 643–647 (2012).
45. Xing, G. *et al.* Long-Range Balanced Electron- and Hole-Transport Lengths in Organic-Inorganic $CH_3NH_3PbI_3$. *Science.* **342,** 344–347 (2013).
46. Stranks, S. D. *et al.* Electron-Hole Diffusion Lengths Exceeding 1 Micrometer in an Organometal Trihalide Perovskite Absorber. *Science.* **342,** 341–344 (2013).
47. Liu, M., Johnston, M. B. & Snaith, H. J. Efficient planar heterojunction perovskite solar cells by vapour deposition. *Nature* **501,** 395–398 (2013).
48. Susrutha, B., Giribabu, L. & Singh, S. P. Recent advances in flexible perovskite

solar cells. *Chem. Commun.* **51,** 14696–14707 (2015).
49. Park, N.-G. Perovskite solar cells: an emerging photovoltaic technology. *Mater. Today* **18,** 65–72 (2015).
50. Tan, Z.-K. *et al.* Bright light-emitting diodes based on organometal halide perovskite. *Nat Nano* **9,** 687–692 (2014).
51. Chin, X. Y., Cortecchia, D., Yin, J., Bruno, A. & Soci, C. Lead iodide perovskite light-emitting field-effect transistor. *Nat. Commun.* **6,** 7383 (2015).
52. Xing, G. *et al.* Low-temperature solution-processed wavelength-tunable perovskites for lasing. *Nat. Mater.* **13,** 476–480 (2014).
53. Grancini, G. *et al.* The Impact of the Crystallization Processes on the Structural and Optical Properties of Hybrid Perovskite Films for Photovoltaics. *J. Phys. Chem. Lett.* **5,** 3836–3842 (2014).
54. D'Innocenzo, V. *et al.* Excitons versus free charges in organo-lead tri-halide perovskites. *Nat. Commun.* **5,** 3586 (2014).
55. Zheng, L. *et al.* Morphology control of the perovskite films for efficient solar cells. *Dalt. Trans.* **44,** 10582–10593 (2015).
56. Snaith, H. J. *et al.* Anomalous Hysteresis in Perovskite Solar Cells. *J. Phys. Chem. Lett.* **5,** 1511–1515 (2014).
57. Milot, R. L., Eperon, G. E., Snaith, H. J., Johnston, M. B. & Herz, L. M. Temperature-Dependent Charge-Carrier Dynamics in CH 3 NH 3 PbI 3 Perovskite Thin Films. *Adv. Funct. Mater.* **25,** 6218–6227 (2015).
58. Zhu, X.-Y. & Podzorov, V. Charge Carriers in Hybrid Organic–Inorganic Lead Halide Perovskites Might Be Protected as Large Polarons. *J. Phys. Chem. Lett.* **6,** 4758–4761 (2015).
59. Stroppa, A., Quarti, C., De Angelis, F. & Picozzi, S. Ferroelectric Polarization of $CH_3NH_3PbI_3$: A Detailed Study Based on Density Functional Theory and Symmetry Mode Analysis. *J. Phys. Chem. Lett.* **6,** 2223–2231 (2015).
60. Dupuis, A.-C. Perovskite solar cell. 1–6 (2014).
61. Docampo, P. & Bein, T. A Long-Term View on Perovskite Optoelectronics. *Acc. Chem. Res.* **49,** 339–346 (2016).
62. Bailie, C. D. *et al.* Semi-transparent perovskite solar cells for tandems with silicon and CIGS. *Energy Environ. Sci.* **8,** 956–963 (2015).
63. Bullis, K. a. A Material That Could Make Solar Power 'Dirt Cheap'. *MIT Technology Review* 8–10 (2013).
64. Yang, J., Siempelkamp, B. D., Liu, D. & Kelly, T. L. Investigation of $CH_3NH_3PbI_3$ Degradation Rates and Mechanisms in Controlled Humidity Environments Using in Situ Techniques. *ACS Nano* **9,** 1955–1963 (2015).
65. Tong, C.-J. *et al.* Uncovering the Veil of the Degradation in Perovskite $CH_3NH_3PbI_3$ upon Humidity Exposure: A First-Principles Study. *J. Phys. Chem. Lett.* **6,** 3289–3295 (2015).
66. Hao, F., Stoumpos, C. C., Cao, D. H., Chang, R. P. H. & Kanatzidis, M. G. Lead-free solid-state organic–inorganic halide perovskite solar cells. *Nat. Photonics* **8,** 489–494 (2014).
67. Wang, K., Liang, Z., Wang, X. & Cui, X. Lead Replacement in $CH_3NH_3PbI_3$ Perovskites. *Adv. Electron. Mater.* **1,** (2015).
68. Babayigit, A. *et al.* Assessing the toxicity of Pb- and Sn-based perovskite solar cells in model organism Danio rerio. *Sci. Rep.* **6,** 18721 (2016).
69. Benmessaoud, I. R. *et al.* Health hazards of methylammonium lead iodide based perovskites: cytotoxicity studies. *Toxicol. Res.* In press (2016). doi:10.1039/C5TX00303B
70. Hailegnaw, B., Kirmayer, S., Edri, E., Hodes, G. & Cahen, D. Rain on Methylammonium Lead Iodide Based Perovskites: Possible Environmental Effects

of Perovskite Solar Cells. *J. Phys. Chem. Lett.* **6,** 1543–1547 (2015).
71. Fthenakis, V. M., Morris, S. C., Moskowitz, P. D. & Morgan, D. L. Toxicity of cadmium telluride, copper indium diselenide, and copper gallium diselenide. *Prog. Photovoltaics Res. Appl.* **7,** 489–497 (1999).
72. Fthenakis, V. & Zweibel, K. *CdTe PV: Real and Perceived EHS Risks*. *National Center for Photovoltaics and Solar Program Review Meeting* (2003). at <http://www.nrel.gov/docs/fy03osti/33561.pdf>

CHAPTER II:
PHTOANODE MODIFICATION

1. TiO_2 Photoanode for Dye Sensitized and Perovskite Solar Cells

Titanium dioxide represents a chemically stabile, non toxic, inexpensive semiconducting material that crystallizes in three crystal phases: anatase, rutile and brookite. The specific optoelectronic properties have made the anatase TiO_2 (band gap energy between 3.2 - 3.6 eV) the most widely used material in DSC configuration, regardless of the sensitizing material.[1,2] The specific values of the electron diffusion length and lifetime are tightly bonded with the structural properties and morphology of the TiO_2 films.[3,4] One of the most appealing properties of the material is the possibility to tailor the shape and the size of the TiO_2 nanoparticles giving the opportunity to optimize important structural, optical and electronic characteristics that have to be satisfied for a mesoporous photoanode film.[5,6]

The porosity of the TiO_2 photoanode is an essential property in dye cell configuration. In order to achieve high light harvesting efficiency (LHE), it is essential to have a large amount of dye absorber. However, since only a monolayer of dye adsorbed on the TiO_2 surface is photoactive (only the first layer of dye will absorb the incident light), it is essential to engineer a system in which the amount of active material (dye) will be increased, but not at the cost of increasing the device size (thickness).

This implication leads to the construction of mesoporous photoanode which increases the effective surface of the TiO_2 and in turn the surface of the dye active layer.

Intuitively it can be assumed that increasing the thickness of the TiO_2 film can largely improve the photon absorption, however due to the nature of the electron transport within the TiO_2 (electron diffusion length and trap states),[7] the thickness increase leads to increased recombination. Therefore the thickness of the photoanode and its porosity are subjected to a tradeoff in order to optimize and achieve not only best dye loading conditions, but efficient electron transport and charge extraction as well.

The efficiency of the dye cell is associated with several recombination mechanisms as described in Chapter I. The kinetics of the charge separation, injection and transport in the photoanode play a crucial role in developing the photoanode film morphology and choosing the semiconducting material.

The dynamics of electron injection and transport through anatase have been widely investigated with respect to other contender materials with optoelectronic properties suitable for DSC.[8] It has been reported that the electron injection efficiency of 1; and the electron mobility of 0.017 cm^2/Vs are most efficient (fastest) in the anatase TiO_2 in comparison with other materials such as ZnO and SnO_2; and thus the TiO_2 has remained the photoanode material of choice.

The transport of injected electrons through the TiO_2 nanoparticle layer, to the external circuit is believed to occur by diffusion, since the macroscopic electric field across the film is negligible, at solar light intensities up to one sun, due to screening by the high ionic strength electrolyte. Several studies have examined the influence of film morphology and traps and defects on electron transport.[9] Figure 1a shows one of the models for electron transport and recombination within the TiO_2. It has been found that electron transport in rutile TiO_2 layers is about an order of magnitude slower than transport in anatase TiO_2.

This difference in transport rate is attributed to a smaller number of interconnections between particles as a result to the more rod-like morphology of the rutile layers. The influence of the overlap between neighboring particles on electron transport is of great importance. Namely, the electron transport through a string of spheres was modeled as a function of the interconnecting areas between the spheres. The findings indicated that if the area of interconnection between the particles is smaller the electron transport was slower.[4] The electron transport dynamics have been modeled using simulated mesoporous random nanoparticle TiO_2 films and the random-walk approach.[10]

The charge transport in the TiO_2 photoanode has great implications on the morphology of the photoanode in the SDSC, and perovskite solar cell configuration as well. Since infiltration of the active material is the main issue, intuitively a higher porosity photoanode could solve the problem. However, it was found that higher porosity films have lower number of interconnections between the nanoparticles, thus there are more isolated areas in the film that are only connected to the rest of the film by a single particle that acts as a nexus. These isolated areas act as spatial electron traps that slow electron transport.[4]

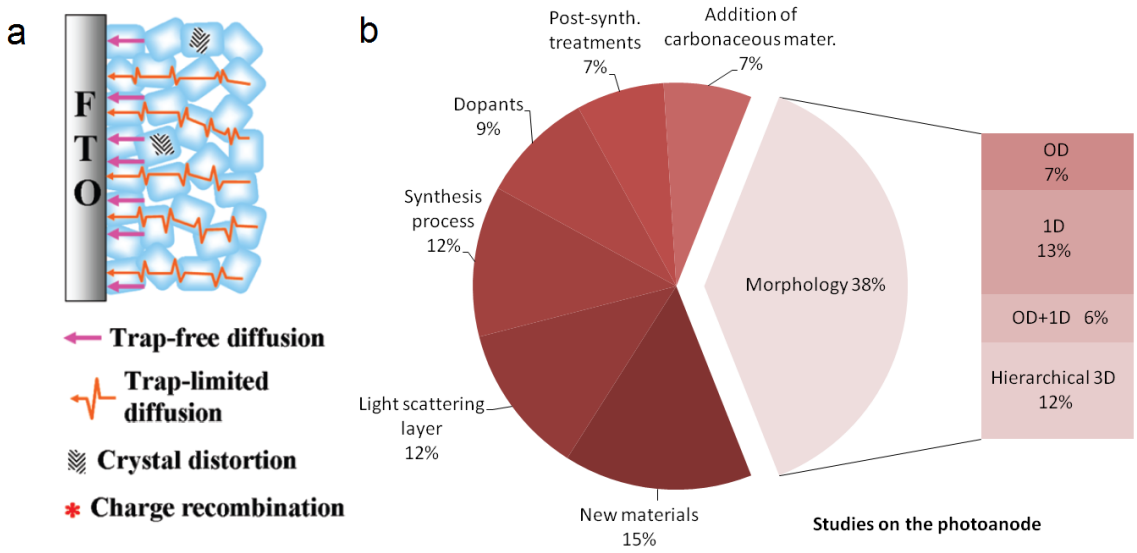

Figure 1. a) Model of electron transport mechanism in nanocrystalline TiO_2 film;[9] b) Photoanode research lines according to 1105 scientific publications.[11]

Since the first publication on DSC it was observed that electron transport depends strongly on light intensity. This dependence was attributed to a broad distribution of traps in the TiO_2. Thus the light-intensity dependence has been explained it in terms of a multiple electron trapping model. The modeled electron transport in the TiO_2 is a random walk diffusion driven, trap assisted mechanism.[7] The trapping sites of electrons are described, based on their energy position with respect to the conduction band of the TiO_2, as ‘‘shallow’’ and ‘‘deep’’ traps. The deep traps are consensually associated to oxygen defect sites, namely vacancies which are more abundant on TiO_2 surface due to unsaturated coordination related to crystal termination. The shallow traps on the other hand are a matter of intense discussion and to date there is not an unambiguous structural feature associated with them that is consensual.[12]

Since establishing the TiO_2 as the prime photoanode semiconductor in the DSC a large number of publications have been reporting on efforts to further optimize the mesoporous film.[13] Figure 1b presents the various research lines reported in various publications for photoanode optimization.[11] Considering the optimization of the TiO_2 photoanode few essential pathways have to be taken into consideration.

Increase of the film effective surface for an amplified dye loading. This methodology has been employed by manipulating the shape and size of titania nanoparticles. This type of photoanode engineering gains particular importance for solid state and perovskite solar cells since the photoanode thickness has to be largely reduced due to insufficient infiltration of the HCM and the perovskite. Additionally, manipulating the size and the interconnectivity of the nanoparticles can have great implication on the electron transport and recombination properties. This brings us to another important photoanode modification;

Enhance electron transport through the film. Reducing the resistivity of the mesoporous titania in order to improve the photogenerated electron mean free path and consequently reduce the electron-hole recombination probability is extremely important for effective device operation. Since the mesoporosity of the anatase titania is essential for achieving a high surface area, the most reported methods of improving the conductivity have been the incorporation of carbon nanotubes (CNT) in the matrix,[14,15] changing the shape or the surface area of the TiO_2 nanocrystals, employing TiO_2 nanotubes[16] or even the growth of mesoporous TiO_2 single crystals.[17]

Improving charge separation and reducing the charge recombination dynamics. There have been investigations in using thin layers of insulating metal oxides on top of the surface of the mesoporous TiO_2 photoanode in order to block the recombination and favorably change in the electronic properties of the photoanode.[18–20] The mechanism of surface passivation of the photoanode has also been used in order to reduce recombination by minimizing the effect of surface traps states. A common practice of surface treatment in highly efficient DSC has been the $TiCl_4$ post-treatment.[21,22]

2. Post-Treatment Modification of TiO_2 Photoanode

One of the basic concepts for efficiency improvement in dye-sensitized solar cells is limiting the electron-hole recombination. One way to approach the problem is to improve the photogenerated charge carriers lifetime and consequently reduce their recombination probability.

Surface post-treatments of the titania photoanode by using $TiCl_4$ treatment have been reported to achieve a series of beneficial effects on the recombination and the surface electric field. There has also been a correlation in the change of the surface morphology as a result of the surface treatment with change in light harvesting and change in transport and recombination dynamics.[23,24] Additionally, reports show that the surface treatment is in fact affecting the porosity of the photoanode, thus there is fine tuning between the porosity of the treated film and the concentration of the $TiCl_4$ solution.[21] The $TiCl_4$ is a volatile chemical and the post-treatment of the photoanode is experimentally demanding,[25] the common practice of the treatment is dipping each electrode in a $TiCl_4$ water solution held at 70–80°C for 30 min, furthermore the standard dipping procedure requires larger amounts of material to be used, since in order to ensure the quality and the reproducibility of the post-treatment reusing the same dipping solution is not recommended.[22,25] Additionally, the strong hydrolysis reaction of $TiCl_4$ when in contact with water causes formation of HCl fumes.

In collaboration with colleges from Vinca Institute in Belgrade, Serbia, and colleagues from IMM-CNR in Bologna, it was established that employing simple *surface treatment via colloidal solution of TiO_2 nanoparticles,* an appropriate substitute of the $TiCl_4$

treatment can be achieved. The results of this investigation are already published (see List of publications) and the following section gives an overview of the study.

Indeed, by drop casting colloidal solution of 5 nm TiO_2 nanoparticles and performing post-treatment of the TiO_2 photoanode, efficiency improvement of 10% with respect to devices with untreated photoanodes was achieved. Moreover, the improvement of the efficiency of the DSC was accomplished by using a time-efficient and low material consumption technique. The outcome of the different sintering temperature of the post-treated photoanodes on their morphology, as well as on the conversion efficiency of the DSC, was investigated. The DSC composed of post-treated photoanodes at 450°C showed an increase in J_{SC} and consequently an increase in efficiency of 10%. Spectroscopic and morphological characterizations were performed to investigate the morphological changes of the photoanode. Electrical characterization was performed by means of solar cell current-voltage characterization and open circuit voltage decay measurements. The next section presents the effects of surface trap states modification as the main reason behind the efficiency changes of the solar cells.

2.1. Experimental – Materials and Methods

All chemicals except for the ones stated otherwise, were acquired from Aldrich, Fluka and used without further purification.

2.1.1. Photoanode Preparation and Characterization

Synthesis of TiO_2 colloidal solution. The Colloidal solution of TiO_2 nanoparticles was prepared according to adapted procedure of Rajh *et al.*[26] 6 ml of $TiCl_4$ was cooled to -20°C and added drop-wise to 200 ml Milli-Q deionized water. The solution was then held at 4°C under vigorous stirring and kept at this temperature for half an hour. By applying dialysis for 3 days of the obtained solution against water, which was changed daily, the pH increased to pH~3 and slow particle growth was achieved (d~4.5 nm). The final concentration of TiO_2 colloids was determined from Ti(IV)-peroxide complex.[27,28]

TiO_2 photoanode preparation. Fluorine doped tin oxide (FTO) substrates (Solaronix TCO 22-7, 7 Ω/sq) were cut in size 1,8x2 cm, washed in successive ultrasonic baths of deionized water, acetone and isopropanol and dried with N_2 gas flow. The TiO_2 mesoporous films were deposited by doctor blade technique. The TiO_2 paste was made suspending P25 nanoparticles and PEG 2000 in water, adding Triton X100 to adjust the viscosity and improve adhesion to the substrate. The thickness of the films was measured by step profilometer. The mesoporous films were kept in air, in dark and prior to colloidal treatment or before dipping in dye for the untreated electrodes, the films were reburned at 450°C for 15 min to remove any moisture. The colloidal nanoparticle solution of 0.12 M was drop casted on to the films, after 1 min the excess was removed and the films were left to dry in air. After drying the photoanodes were sintered at different temperatures, 150, 350 and 450°C in air for 20 min.

Raman spectroscopy. Samples were prepared by drop casting a 0.12 M of TiO_2 colloidal solution onto clean glass slides and sintering on a hot plate in air for 20 min at different temperatures of 150, 350 and 450°C. The Raman measurements were performed with a Micro-Raman Renishaw 1000 system with λ_{ex}=632.8 nm in confocal mode. The acquisition time was 40 s in order to achieve a relatively good signal to noise ratio using a power

density of $2x10^3$ W/cm^2. A TiO_2 mesoporous film made from colloidal paste of P25 nanocrystals was prepared and used as a control sample.

Absorption measurements were performed on dye solutions desorbed from films prepared in a photoanode configuration with and without post-treatment using a JASCO V-550 UV-Vis spectrometer. FTO substrates coated with mesoporous TiO_2 films of 1 cm^2 were post-treated and the films with the matching thickness were dipped and left overnight in a 9 mM ethanol solution of N3 dye (Solaronix). After removing the substrates from the solution and washing off the excess dye with ethanol the films were left to dry in dark and then the dye was desorbed from the films placing the samples in sealed containers with equal volumes of a 0.1 M solution of NaOH in water.

Thickness measurements were conducted using a step profilometer. Investigation of the thickness and roughness change after colloidal treatment and sintering procedure at 150, 350 and 450°C was performed on samples prepared in photoanode configuration, i.e., mesoporous TiO_2 films of 1 cm^2 deposited onto FTO substrates. The thickness was measured before and after the colloidal treatment.

Scanning Electron Microscope (SEM) imaging was made to study the surface of the films. The experiments were performed using a LEO 1530 FE-SEM, with a Schottky emitter, operated at 10 keV accelerating voltage, equipped with Everhart-Thornley and In-lens detectors for secondary electrons and Oxford INCA EDS X-Ray spectrometer.

2.1.2. DSC Preparation and Characterization

The TiO_2 photoanodes without and with post-treatment at different temperatures were prepared as described in Section 2.1.1. The size of the mesoporous film was 1 cm^2. After post-treatment sintering, the photoanodes were subsequently cooled down to 80°C and dipped in 9 mM solution of N3 dye (Solaronix) in ethanol.

The substrates were left overnight in the dye solution in dark, after which they were washed with ethanol and dried for few minutes in air. The counter electrode was a FTO glass substrate coated with platinum precursor solution (Platisol T, Solaronix) which was burned at 450°C for 20 min. The cell was assembled using 60 μm Surlyn spacer. Ionic liquid electrolyte consisting of 0.6 M BMII (1-butyl-3-methylimidazolium iodide), 0.1 M LiI, 0.05 M I_2 and 0.5 M TBP (4-tert-Butylpyridine) in acetonitrile was inserted in to the cell before complete sealing. To ensure reproducibility, for each batch of cells, at least 2 identical cells with the respective post-treatment were made. Investigation was also made on cells prepared using a Solaronix AN-50 electrolyte, with mesoporous photoanode thickness around 8 μm. Where stated, a compact TiO_2 layer was deposited via spin coating a precursor solution of 0.25 M TAA (Diisopropoxytitanium bis (acetylacetonate) solution) in ethanol. The compact films were formed by burning the coated substrates at 490°C for 1 hour.

Current-voltage characteristics of the cells were measured with Keithley 236 source-measure unit under simulated AM1.5 illumination of 100 mW/cm^2 Abet Technologies Sun 2000 Solar Simulator. The simulator was calibrated using a silicon reference cell with KG5 filter, and the cells were masked with a sample holder witch disabled any light piping effects. The effective cell surface area was kept at 1 cm^2.

Open Circuit Voltage Decay (OCVD) measurements were performed using a Keithley 2400 SourceMeter, exposing the cell to full sunlight for 5 s to achieve steady state, then the illumination was interrupted by closing the shutter, the time interval between points was 50-100 ms.

2.2. Results and Discussion

2.2.1. Photoanode Morphology Dependence of Post-Treatment Sintering Temperature

The investigation on the coating of the photoanode initially established that the optimal concentration of the colloidal solution was 0.12 M. Increasing the concentration leads to cracking and peeling of the films. The effect of further decoration of the mesoporous films by successive coatings led to similar results. This was a consequence of tightly packed areas of the TiO_2 film surface that were acting as a compact layer which when dried, shrank, causing strain between the formed surface film and the rest of the mesoporous matrix, which subsequently led to cracking and detaching from the substrate. Employing a post-treatment of the TiO_2 mesoporous photoanode films requires a sintering process in order to remove any residual water or impurities from the mesoporous matrix and film surface, to ensure an efficient dye loading and to improve the connection between the nanoparticles. However, to try and understand the effect of the sintering temperature on the size of the colloidal TiO_2 nanocrystals, as well as, on the morphology and porosity of the mesoporous films, systematic investigations were performed using profilometric measurements, Raman spectroscopy and SEM imaging.

To investigate the nanocrystalline size and morphology of the films with regard to the temperature treatment, Raman measurement was performed on samples prepared as described in Section 2.1.1.

The data of the Raman spectra are summarized in Table 1. Estimations of the crystalline size were made according to Kelly *et al*.[29] experimental results. The analysis was done on the basis of the two most intense anatase E_g modes around 145 cm^{-1} and 640 cm^{-1}. Extracting the values for the full width half maximum (FWHM) of the peaks (Γ_1 and Γ_2, respectively), using the available data, it was observed that by increasing the annealing temperature, the size of the nanocrystals increases as a consequence of nanocrystalline coalescence during the burning process (see Figure 2). Here we note that the Raman measurement is essentially a measurement of the crystalline core and not the nanoparticle itself, which in turn could be few nanometers larger.

Table 1. Raman shift (ω) and FWHM (Γ) of the of the E_g modes around 145 cm^{-1} and 640 cm^{-1} Nanocrystalline size (Φ) dependence on the sintering temperature, estimated from the FWHM.

	Colloidal nanoparticles						**P25**	
***T* (°C)**	**150**		**350**		**450**		**450**	
	cm^{-1}	**Φ (nm)**	**cm^{-1}**	**Φ (nm)**	**cm^{-1}**	**Φ (nm)**	**cm^{-1}**	**Φ**
ω_1	157.9 ± 0.9		149.8 ± 1.2		146.7 ± 1.6		144.1	
Γ_1	39.7 ± 0.3	3.2 ± 0.2	17.9 ± 2.9	7.0 ± 1.0	15.6 ± 2.3	8.0 ± 1.1	9.6	>23
ω_2	640.6 ± 0.2		640.9 ± 2.1		641.9 ± 0.6		639.0	
Γ_2	80.8 ± 1.8	3.4 ± 0.1	52.5 ± 0.6	5.1 ± 0.1	38.3 ± 7.5	7.7 ± 1.9	25.5	>17

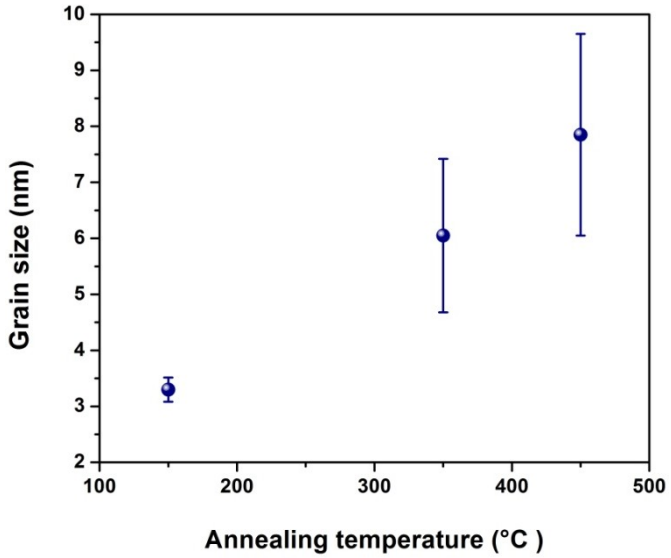

Figure 2. Dependence of colloidal nanoparticles size on annealing temperature.

The colloidal post-treatment of the mesoporous TiO_2 photoanodes induces a slight thickness change. For the films between 13-15 μm, an increase of 0.2-0.5 μm, depending on the sample was observed. An interval is reported, rather than a fixed thickness increase, as a result of multiple measurements on large number of substrates, also taking into account the difficulty of precise measurement on films of 1 cm^2 surface with such roughness. This difference in thickness was compensated by using a few tenths of micron ticker films for the untreated photoanode. Additionally the 2D surface profile did not indicate any difference in the roughness of the samples as presented in Figure 3.

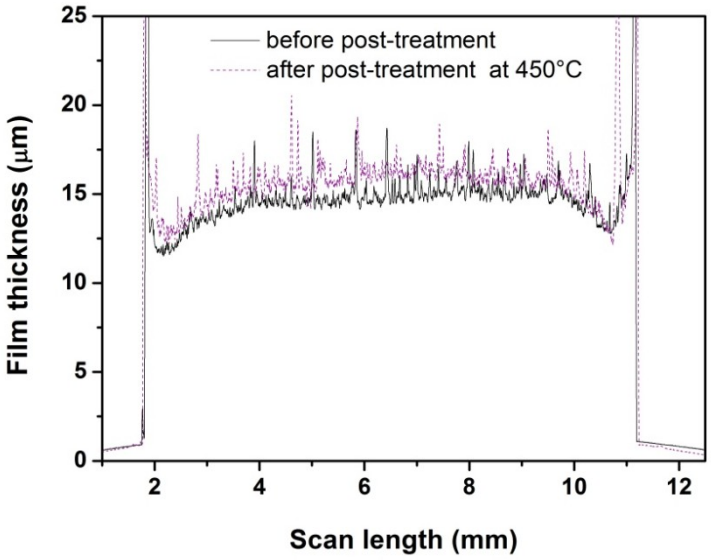

Figure 3. Surface profile of the TiO_2 film before and after the colloidal post-treatment sintered at 450°C.

Figure 4 shows secondary electrons SEM images of the untreated and post-treated photoanode at 450°C. At this resolution no difference between the surface morphologies was observed.

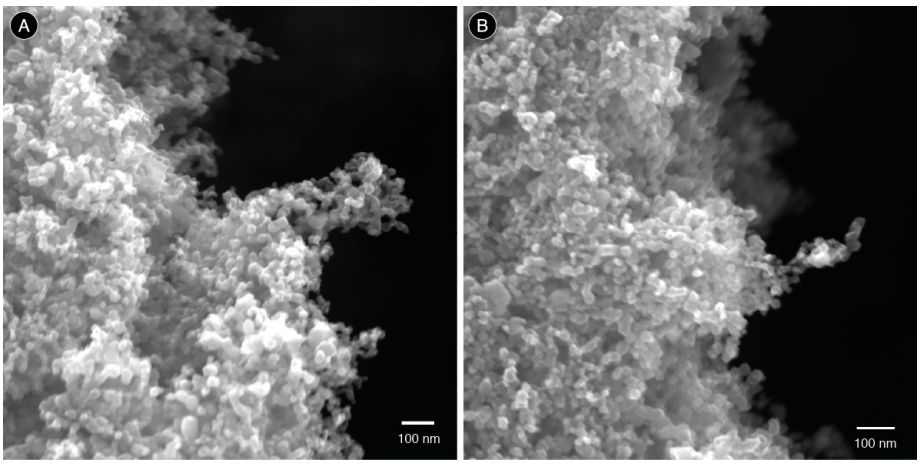

Figure 4. Secondary electrons SEM images of mesoporous TiO_2 photoanodes; a) untreated photoanode; b) post-treated photoanode sintered at 450°C.

Post-treatment of the photoanode with nanoparticles of around 5 nm can impact the surface volume ratio of the mesoporous films. Any change in efficiency of the DSC could be attributed to the higher or lower dye loading of the photoanodes. To study the effect of the post-treatment of the photoanode at the investigated temperatures, absorption measurements were performed. The UV-Vis absorption spectra of the dye solutions desorbed from untreated and post-treated mesoporous films are shown in Figure 5.

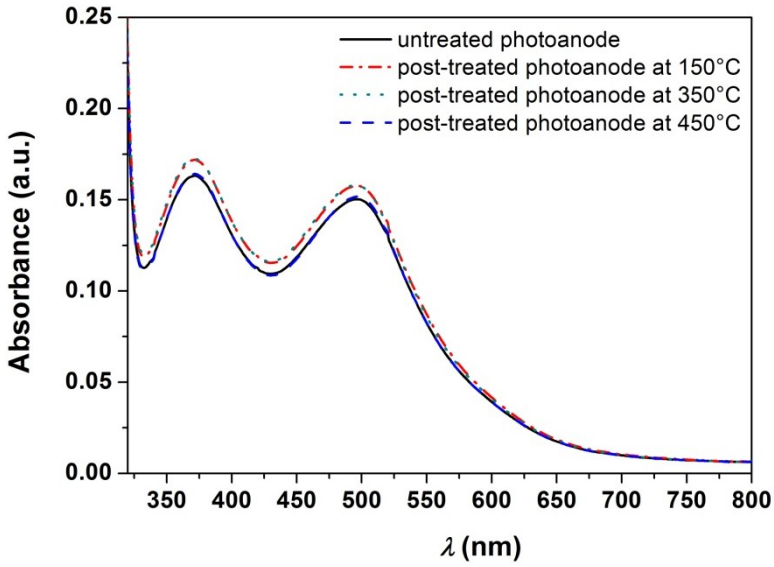

Figure 5. Absorbance of aqueous solution of N3 dye desorbed from TiO_2 mesoporous films.

It can be observed that there is a small increase (around 5%) in the dye absorption of the films treated at 150 and 350°C, in contrast, the film with surface treatment at 450°C does not show practically any difference in dye absorption with respect to the untreated film. This increase could be expected taking into account the smaller nanoparticle size in the coated films sintered at lower temperatures. The surface treatment in this case is increasing the effective surface area of the mesoporous film, hence increasing the dye absorption. The absorption measurements were performed on several batches of untreated and post-treated films to substantiate the observed absorption trend. It was found that even though the absorption increase for the low temperature sintered films was small (5.0 ± 1.5%), the tendency of this increase and the lack of difference between the untreated and films treated at 450°C remained.

According to the performed measurements and investigations on the post-treated TiO_2 films, it can be concluded that the surface treatment is only marginally increasing the thickness of the films without changing the surface morphology and slightly increasing the surface/volume ratio (S/V) only for low temperature annealed samples, while for those sintered at higher temperature (450°C) there is no distinction in the S/V with the untreated films.

2.2.2. Solar Cell Efficiency Improvement by Photoanode Post-Treatment

Electrical investigations were made on complete dye-sensitized solar cell devices employing post-treated photoanodes annealed at different temperatures to understand the effect that the colloidal post-treatment would have on the efficiency of the cell. A cartoon of the solar cell configuration and the difference between the treated and post-treated photoanode is presented in Figure 6. The current-voltage characteristics of the prepared cells are shown in Figure 7.

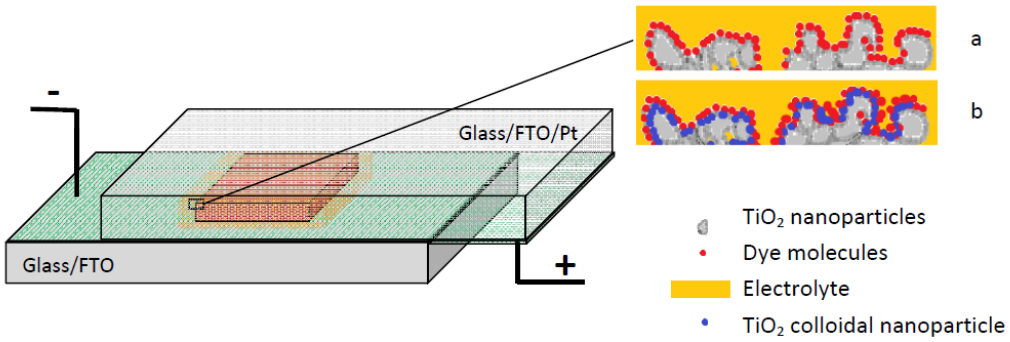

Figure 6. Cartoon of the DSC configuration; cross section of: a) non treated photoanode; b) post-treated photoanode.

The parameters of the cells in Figure 7a are presented in Table 2. The highest conversion efficiency was observed for the DSC device with the colloidal treatment of the photoanode sintered at 450°C, showing an improvement in efficiency larger than 10% with respect to the bare one. This improvement is mainly associated with the increase in the photocurrent of the cell. The increase in the I_{SC} depends on the LHE and or the collection and injection efficiency.[30] However, the investigation done on the dye absorption of the photoanode indicates that there are no extra dye molecules absorbed to account for an increase of 10%. Furthermore, taking into account only the UV-Vis absorption measurements one would expect to find a slight increase in the photocurrent (about 5%) for the cells with photoanode treatment at 150°C and 350°C, but in fact the efficiency of these cells is slightly lower than for the cells with the untreated photoanode, as seen from Figure 8.

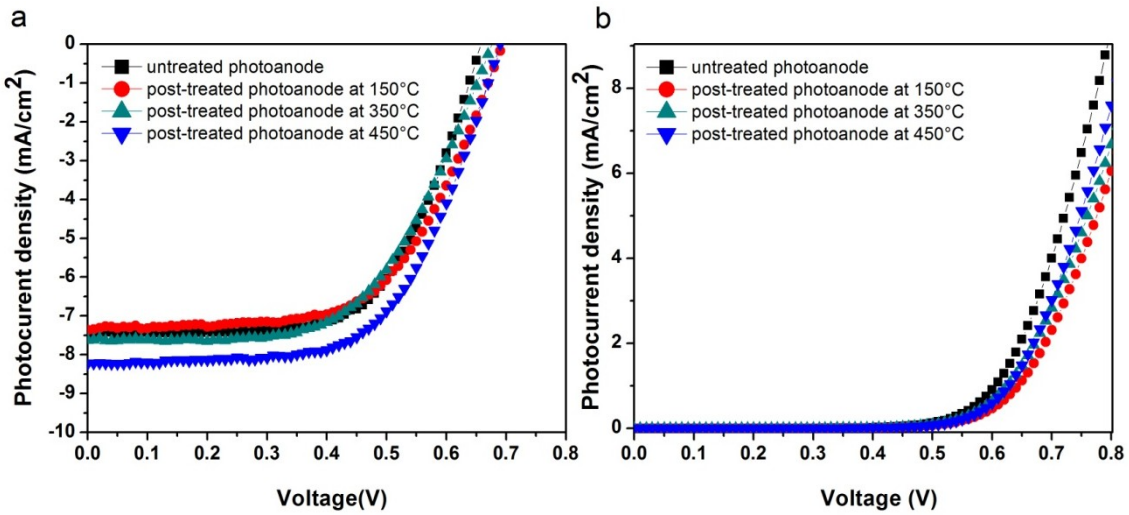

Figure 7. Current density-voltage characteristics of DSC with untreated photoanode and post-treated photoanodes with colloidal treatment at different temperatures: a) at 1 sun illumination; b) in dark.

Table 2. Photovoltaic parameters of the DSC with *J-V* curves shown in Figure 7a.

Photoanode type	J_{SC} (mA/cm^2)	V_{OC} (V)	*FF* (%)	η (%)
No post-treatment	-7.45	0.66	62.99	3.10
150°C	-7.36	0.69	60.21	3.06
350°C	-7.62	0.68	58.01	3.01
450°C	-8.23	0.69	60.92	3.46

Apparently there is no significant correlation among the increase in the dye absorption (the surface/volume ratio) and the conversion efficiency increase in these cells, allowing to disregard the LHE as a reason for the efficiency increase.

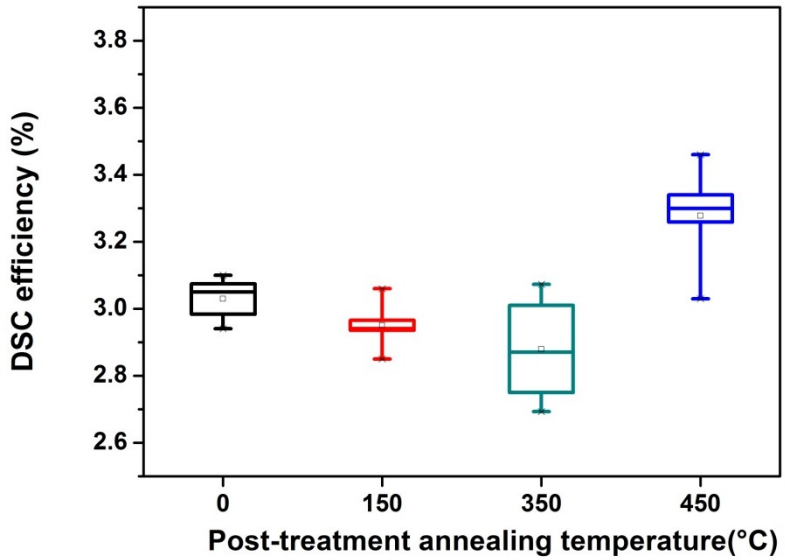

Figure 8. Box plots of the dependence of the efficiency of the DSC on the photoanode post-treatment temperature.

Furthermore, low sintering temperature can also affect the conductivity of the TiO_2 photoanode by slowing down the charge transport probably as a consequence of the low interconnectivity of the surface nanoparticles to the mesoporous matrix. In the case of low temperature annealed photoanodes, these two effects, LHE increase and worse electron transport would compensate each other to which end the final conversion efficiency of the cells with treated and untreated electrodes is similar.

If we consider the difference in the dark current shown in Figure 7b, we can notice a very slight shift of the dark current onset, hence the increase in the V_{OC} of 0.01-0.02 V. According to Ito *et al.*,[25] the suppression of the dark current for the post-treated photoanodes would indicate a decrease of the electron trap sites on the TiO_2 surface. This argument would suggest that the photoanode post-treated at 150°C has the smallest surface trap density. However, if the steepness of the slopes is taken in to account, where the steepest slopes indicate lowest series resistance in the cell,[31] it can be assumed that, in fact for the 150°C and 350°C treated samples there is an issue of the electron transport through the photoanode due to interconnectivity of the nanoparticles, which in turn is suppressing the cell efficiency regardless of the higher dye absorption and possibly lower surface trap sites of these photoanodes.

This is only a qualitative estimation since the series resistance depends not only on the electron transport in the photoanode but on the transport in the FTO substrate, electron transfer across the interface of electrolyte/Pt-FTO, and the electrolyte diffusion time.[32] Nevertheless, for the means of this investigation, due to the identical construction elements of the cells and changes only in the photoanode surface, this result is deemed relevant. It is reasonable to suggest that the increase in the I_{SC}/efficiency is a result of either change in the collection and/or injection efficiency.

In order to have an increase in the rate and efficiency of electron injection from the photo-excited dye into the TiO_2 one should observe a downward shift of the conduction band which would result in lower V_{OC}, since the band edge would become closer to the redox potential. This has not been observed in the investigation taking into account the solar cells characteristics. According to Sommeling *et al.* this downward shift effect could be balanced out if the surface treatment also strongly reduces the recombination rate, hence no change in the V_{OC} would be recorded.[23] In fact the small increase in the V_{OC} can also be attributed to increase in the quasi-Fermi level of the TiO_2 which happens as a consequence of reduced density of surface trap states of the titania.[21] Nevertheless, at this point the injection efficiency is ruled out as the dominant contributor to the improvement in the current density.

The open circuit voltage decay (OCVD) of the solar cells with and without a surface treatment was recorded to investigate in-depth the mechanism behind the efficiency improvement in using the colloidal treatment and annealing at 450°C. This technique is used to extract information on the recombination time and mechanism of the electrons with the oxidized electrolyte in the DSC (see Appendix). Figure 9a shows the decay curves of the cells prepared with and without the colloidal treatment of the photoanode. It can be seen that the V_{OC} of the cell with post-treated photoanode has a slower initial decay, which continues with time to decay in a similar way as the cell with the untreated photoanode. The steeper decay of the cell with untreated photoanode is an indication of faster recombination of the electrons with the oxidized species in the electrolyte. According to the theory[33] the electron lifetime τ can be derived from the derivative of the V_{OC} decay and it's presented in Figure 9b.

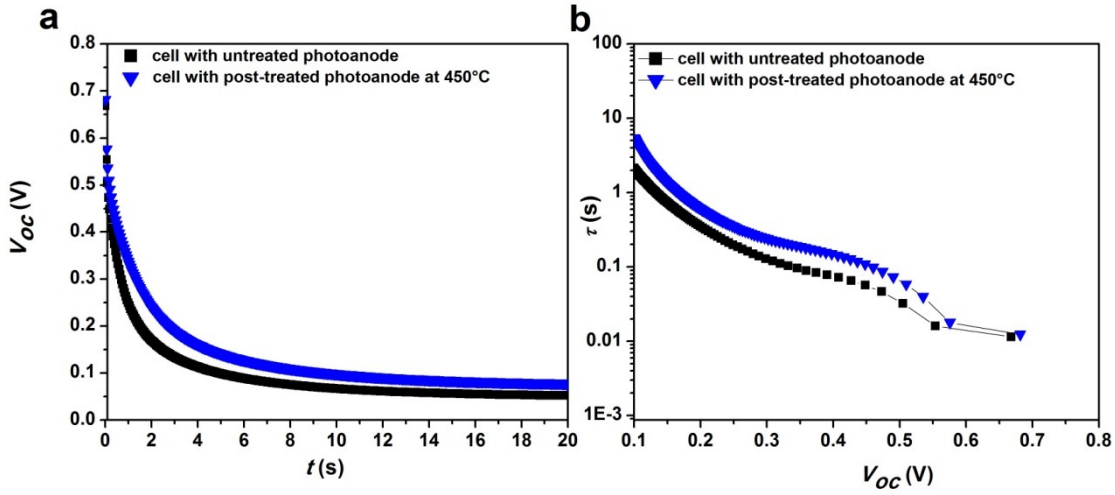

Figure 9. a) Open circuit voltage decay curves; b) Electron lifetime as a function of the V_{OC}; of DSC with untreated photoanode and post-treated photoanode with colloidal treatment at 450°C.

The logτ-V_{OC} curve has 3 characteristic regions which give information on the electronic states involved in the recombination process. A constant electron lifetime at high V_{OC} indicates recombination via free electrons in the conduction band, a linear increase in the mid V_{OC} region is a sign of trapping/detrapping events where charge transfer is mainly governed through bulk traps, and a region of inverted parabola in the low V_{OC} region indicates a change in the trap states responsible for the recombination from bulk to surface states.[34]

From the two curves in Figure 9b it is evident that there is a very small region of seemingly constant lifetime at high V_{OC} around 0.7 V. In this region there is practically no difference between the two cells. Analyzing the shape of the curves it can be noticed that there is a more significant difference in the electron lifetime of the two cells in the region where the charge transport is governed by processes of trapping and detrapping. The relatively linear part up to V_{OC}~0.45 V suggests that at this position of the Fermi level the transfer occurs mainly through bulk traps in the TiO_2. The onset of the parabolic shape of the curve for the cell with the post-treated photoanode is slightly shifted towards lower potentials witch signifies the beginning of recombination processes dominated by surface states. Charge transfer occurs through bulk trap states up to lower values of the potential compared to the cell with the untreated photoanode. It would seem that the mechanism of increasing the efficiency of the cell is in fact determined by the decrease of surface trap states. By modifying the surface trap density one can manage to reduce the charge transport through the surface states and increase the electron lifetime of the TiO_2 photoanode and consequently reduce the recombination probability. This increase in the electron lifetime can be the reason behind the efficiency increase.

Since there have been reports in the literature that the recombination kinetics between the TiO_2 photoanode and the electrolyte might be dependent on the ionic liquid in the electrolyte,[35,36] OCVD measurements were performed on solar cells with commercially available Solaronix electrolyte. Without the intention of investigating how concentration, diffusion coefficient of the triiodide, or how different cations affect the recombination, but rather just to confirm that the surface treatment is reducing the surface states of the TiO_2 mesoporous film, and in doing so reducing the interfacial recombination regardless of the electrolyte. The cell size and assembly and all other materials and parameters are as described previously in Section 2.1.

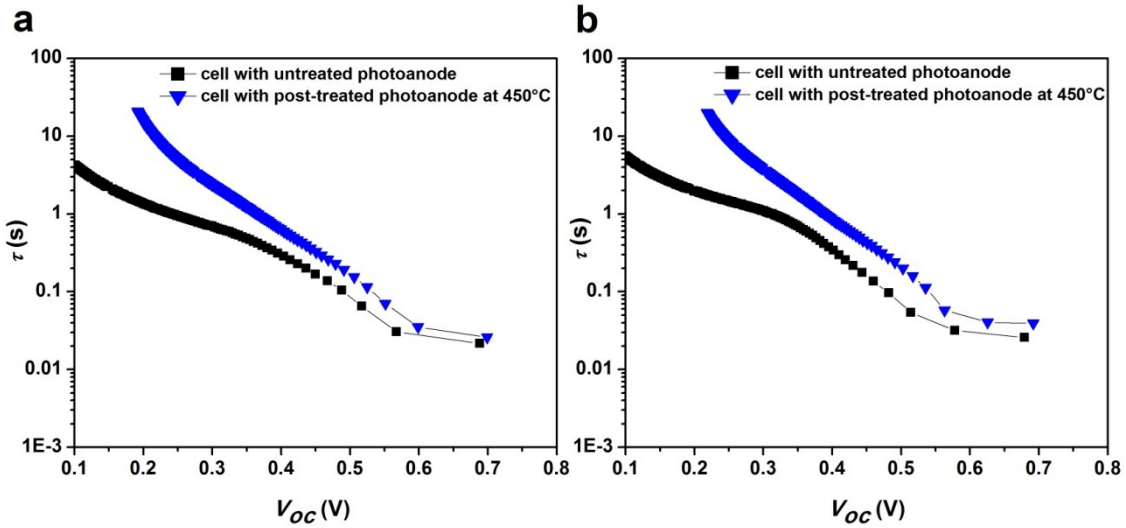

Figure 10. Electron lifetime as a function of the V_{OC} of DSC with untreated photoanode and post-treated photoanode with colloidal treatment at 450°C, with Solaronix electrolyte: a) without a compact layer; b) with a compact layer.

In Figure 10a the electron lifetime dependence on the open circuit voltage of these cells is presented. The shape of the curves emphasizes the difference in the recombination mechanism even more significantly. At high V_{OC} the electron transport through the conduction band is demonstrated with the seemingly constant electron lifetime. The exponential increase of the lifetime represented with the straight line in the logarithmic representation follows the same trend of trap-facilitated transport as described from the curves in Figure 9b. However at $V_{OC} < 0.4$ V for the untreated electrode there is an onset of parabolic curvature which indicates that recombination through surface traps becomes dominant, whereas for the post-treated electrode this onset begins at around 0.25 V. Because the transport mainly occurs through bulk trap states, the recombination time is prolonged by one order of magnitude considering that the electrons are caught and released much faster from surface than from bulk trap states. This type of lifetime dependence points out that surface traps have been significantly diminished.

In contrast to the $\tau(V_{OC})$ curve shape of the cells with ionic liquid electrolyte presented in Figure 9b, the curves in Figure 10a are quite different. Explicitly this difference is evident in the lower electron lifetime and the more pronounced inverted parabola shape in the low V_{OC} region. The lower electron lifetime can be attributed to the higher thickness of the mesoporous photoanode. Because of the grater surface area and the larger number of grain boundaries, a more intense electron recombination due to a higher surface states density can be expected. The shape of the inverted parabola region is determined mainly by the reorganization energy of the acceptor species in the electrolyte.[34] Furthermore, the combination of different dye and electrolyte components on semiconducting nanocrystals can change the density of surface states.[37]

According to Cameron and Peter,[38] it is essential to also take into account the recombination with the electrolyte through the substrate when analyzing the OCVD curves. But since no surface treatment is made on the substrate in the preparation of the different photoanodes and the investigation is focused on the surface treatment of the photoanode without changing the electrolyte within the same batch of cells, for the purposes of analyzing the charge transfer through different trap states, the back reaction via the substrate was not taken into account, since the effects of this reaction should be the same in all the cells. However, with the intention of confirming the validity of the results, identical

cells to those measured in Figure 10a were prepared, with the only difference of adding a compact TiO_2 layer. The results are shown in Figure 10b. It is evident that using a compact layer doesn't significantly change the shape of the $\tau(V_{OC})$ curve, meaning that the cells employing a TiO_2 compact layer and the ones without the compact layer have almost identical $\tau(V_{OC})$ curve shape. This result again confirms that the main difference in the electron lifetime is due to the reduction of the surface state transport.

2.3. Conclusion

The implementation of TiO_2 nanoparticle colloidal solution for post-treatment of the dye sensitized solar cell photoanode has proven favorable in efficiency improvement. An increment in the efficiency of 10% was established for the solar cells with post-treated photoanode, with the colloidal solution of anatase nanoparticles at 450°C, with respect to the solar cells with the untreated one. The post-treatment sintering temperature shows dependence on the morphological properties of the photoanode films as well as the impact on the photovoltaic properties of the DSC. Investigating the mechanisms responsible for this efficiency increase further showed that the recorded efficiency increase was mostly a result of an increase in the short circuit current; however there was no evidence of an increase of the effective surface area of the post-treated photoanode or an increased dye loading. From the conducted investigation by OCVD measurements it can be validated that this type of colloidal treatment of the mesoporous photoanode successfully reduces the number of surface traps that can act as recombination centers, hence prolonging the electron lifetime. The post-treatment nanoparticle layer operates in a manner of passivating the surface of the photoanode altering the recombination mechanism by shifting the bulk trap state dominant transport to lower potentials. The colloidal treatment does not only increase the overall cell efficiency, but it represents a facile method for post-treatment that leads to further cost beneficial manufacturing of the dye sensitized solar cell.

3. Composite Single Wall Carbon Nanotube/TiO_2 Photoanode

It has been shown that one of the limiting factors in the efficiency of dye sensitized solar cells (DSC) is the relatively low mobility of electrons in the TiO_2 mesoporous photoanode.[39] Obtaining higher efficiency in DSC can be attributed mainly to enhancement of charge separation and improvement of charge transport through the cell. Perfecting these transport mechanisms ensures reduction of the electron-hole recombination, thus improving the cell parameters such as the open circuit voltage V_{OC}, short circuit current I_{SC}, fill factor FF and ultimately, the overall efficiency η.

The challenge is to facilitate the electron transport through the thick mesoporous TiO_2 photoelectrode by ensuring a faster electron collection and improving the electron mean free path. One of the possibilities to achieve this is by engineering a composite the TiO_2 photoanode. Introducing highly conductive carbon materials in the mesoporous scaffold, such as graphene in order to form a composite material with enhanced electron transport properties have been reported to increase the efficiency of the DSC devices by 30-40%.[40,41]

On the other hand, reported efficiency improvement for composite carbon nanotube/TiO_2 mesoporous photoanodes are slightly lower.[15,42,43] However, the electronic type and the

degree of bundling of the CNT have been reported as significant contributors to the final photovoltaic properties of devices incorporating composite photoanodes.[14]

Carbon nanotubes are composed of graphene sheets, each rolled into a tube, where all the carbon atoms are sp^2 σ bounded which in turn provides specific advantageous optical, electrical, mechanical and thermal properties for charge transport applications.[44] Depending whether the CNT are composed of a single graphene sheet or several rolled graphene sheets concentrically placed one inside the other, single wall carbon nanotubes (SWCNT) and multi-wall carbon nanotubes (MWCNT) are distinguished. Depending on the different wrapping angles, SWCNT can be zigzag, armchair and chiral, whereas, depending on the chirality and the diameter they can be metallic or semiconducting. During the production of SWCNT, chirality cannot be controlled meaning that statistically a batch of nanotubes will contain 1⁄3 of metallic with practically a "zero-gap" (<0.1 eV) and 2⁄3 semiconducting nanotubes with a narrow band gap (0.4-1.2 eV),[45–47] which can subsequently be separated by other methods.[48]

Having in consideration their specific electrical properties,[49] introducing SWCNT in the mesoporous anatase TiO_2 film should reduce the electrical resistivity of the film.

With this in mind further research into the improvement and optimization of the TiO_2 photoanode, with respect to dye sensitized solar cell concept and subsequently the perovskite solar cell, was conducted by engineering a composite SWCNT/TiO_2 photoanode. In order to obstruct bundling and to provide quality dispersion, a unique method for dispersion of CNT in O-benzyl tyrosine was employed.[50]

Investigations of SWCNT loading in the composite photoanode were performed to understand the optimal ratio between the constituents which would yield highest solar cell efficiency. Efficiency increment raging from (5-50%) with introducing small weight ratios of SWCNT vs. TiO_2 was established depending on solar cell technology and device preparation materials and conditions.

3.1. Experimental

All chemicals except for the ones stated otherwise, were acquired from Aldrich, Fluka and used without further purification.

3.1.1. Photoanode Preparation and Characterization

Composite SWCNT/TiO_2 photoanode preparation. Fluorine doped tin oxide (FTO) substrates (Solaronix TCO 22-7, 7 Ω/sq) were cut in size 1,8x2 cm, washed in successive ultrasonic baths of deionized water, acetone and isopropanol and dried with N_2 gas flow. The TiO_2 paste was made suspending P25 nanoparticles and PEG 2000 in water, adding Triton X100 to adjust the viscosity and improve adhesion to the substrate. The SWCNT were dispersed in a $7 \cdot 10^{-4}$ M water solution of aromatic amino acid O-benzyl tyrosine[50] with a final concentration of 0.92 mg/ml. Sonication was used as a method to promote efficient dispersion of the SWCNT. The SWCNT/TiO_2 paste for preparation of composite photoanode films was prepared by mixing in the O-benzyl tyrosine/SWCNT suspension in the pristine TiO_2 paste. The pastes were accordingly adjusted (adding water) to obtain equivalent viscosity and weight ratios of SWCNT to TiO_2 of 0.04; 0.07; 0.15; 0.30 and 0.80%. The plain TiO_2 and composite SWCNT/TiO_2 mesoporous films were obtained by doctor blade deposition of the pastes, and subsequent annealing on a hot plate for 15 min at

150°C and 40 min at 450°C for the DSC, whereas, diluted pastes were deposited by spin coating on substrates for SDSC and PSC. The thickness of the films was measured by step profilometer.

Raman spectroscopy. Spectro-microscopic characterization of the photoelectrodes was made by inVia Renishaw micro-Raman (λ_{ex} = 532 nm) in streamline configuration.

SEM images were obtained using a Zeiss FEG-SEM LEO 1530 electron microscope at 5.00 kV equipped with an energy dispersive X-ray spectrometer (EDX).

Electrical conductivity measurements. Plain TiO_2 and composite SWCNT/TiO_2 mesoporous films were prepared on clean glass substrates and 100 nm Ag contacts were deposited on top by thermal evaporation using a transistor shadow mask with 100 μm channel length. Two contact current-voltage measurements were performed with a Keithley 236 source-measure unit under 1 sun illumination by Abet Technologies Sun 2000 Solar Simulator.

3.1.2. Solar Cell Preparation and Characterization

Dye sensitized solar cell (DSC). Photoanode preparation is described in Section 3.1.1. The dye cell preparation and assembly follows the same procedure as reported in detail in Section 2.1.2. Briefly, after the adsorption procedure of the N3 dye (Solaronix), the cell was assembled by using a FTO counter electrode coated with platinum, in a sandwich configuration by sealed with a 60 μm Surlyn spacer. The ionic liquid electrolyte consisting of 0.6 M BMII, 0.1 M LiI, 0.05 M I_2 and 0.5 M TBP in acetonitrile was inserted in to the cell before complete sealing. For the devices employing a compact TiO_2 layer, prior to the mesoporous film deposition, a precursor solution of 0.25 M TAA in ethanol was spin coated on top of the clean FTO and annealed for 1 hour at 490°C. For the solar cells which were subjected to photoanode post-treatment by TiO_2 colloidal solution, prior to dye absorption, the photoanodes were post-treated at 450°C as described in Section 2.1.1.

Solid state dye sensitized solar cell (SDSC). FTO substrates (Solaronix TCO 22-7, 7 Ω/sq) were cut in size 1,8x2 cm, appropriately etched with Zn powder and HCl, and washed as described in the previous sections for photoanode preparation. Compact TiO_2 layer was deposited from precursor solution of 0.25 M TAA in ethanol by spin-coating on top of the clean FTO and annealing for 1 hour at 490°C. The plain TiO_2 and SWCNT/TiO_2 mesoporous films were prepared as described (Section 3.1.1.). For the SDSC where post-treatment with a colloidal solution of TiO_2 nanoparticles was applied, the procedure was followed as in Section 2.1.1. After photoanode preparation the samples were dipped in 9 mM N3 dye (Solaronix) solution to ensure the dye absorption, and subsequently a HCM was deposited on top by spin-coating. The HCM was a 150 mg/ml of 2,2',7,7'-Tetrakis[N,N-di(4-methoxyphenyl)amino]-9,9'-spirobifluorene (spiro-OMeTAD (LUMCHEM)) solution in chlorobenzene, doped by 4-*tert*-Butylpyridine (TBP) and bis(trifluoromethane)sulfonimide lithium salt (LiTFSI) 170 mg/ml solution in acetonitrile (1:9.25 μl/mg TBP:spiro-OMeTAD; 1:4.25 μl/mg LiTFSI:spiro-OMeTAD). The cells were prepared in air and left overnight in dark prior to top contact deposition. The deposition of the top contact was done by thermal evaporation of 120 nm Ag employing a shadow mask to provide a four 0.16 cm^2 solar cells per substrate.

Perovskite solar cell (PSC). Compact TiO_2 layer was prepared on clean etched FTO substrates (see previous paragraph on SDSC preparation) from a precursor solution of 0.25 M TAA in ethanol by spin coating. The films were annealed for 1 hour at 490°C. Mesoporous plain TiO_2 and composite SWCNT/TiO_2 films were prepared as described in

more detail in Section 3.1.1. Methylammonium iodide CH_3NH_3I was crystallized from methylamine and hydroiodic acid according to standard procedure.[51] The CH_3NH_3I and $PbCl_2$ were dissolved at a 3:1 molar ratio in N,N-Dimethylformamide (DMF) to form a 35 and 40 wt% Cl-doped $MAPbI_3$ (MAPI) perovskite precursor solution. The MAPI was deposited on top of the mesoporous films by spin-coating, and annealed on a hot plate at 95°C for 70 min in a N_2 filled glove box with approximately 30% relative humidity. After perovskite formation, spiro-OMeTAD was deposited on top, again by spin-coating, and the samples were left to dry overnight in dark, in ambient air. Afterwards, 120 nm silver top contacts were deposited by thermal evaporation using a shadow mask to obtain 4 (0.16 cm^2) solar cells per substrate.

Current-voltage characteristics of the cells were measured with Keithley 236 source-measure unit under simulated AM1.5 illumination of 100 mW/cm^2 Abet Technologies Sun 2000 Solar Simulator. The simulator was calibrated using a silicon reference cell with KG5 filter, and the cells were masked with a sample holder witch disabled any light piping effects.

Open circuit voltage decay (OCVD) measurements were performed using a Keithley 2400 SourceMeter, exposing the cell to full sunlight for 5 s to achieve steady state, then the illumination was interrupted by closing the shutter, the time interval between points was 50-100 ms.

3.2. Results and Discussion

3.2.1. Morphology and Electrical Properties of Composite Photoanodes

Engineering a composite photoanode by incorporation SWCNT in the mesoporous network essentially needs to improve the conductivity of the photoanode and additionally sustain the microscale morphology and mesoporosity of the plain TiO_2 film. Using the biocompatible O-benzyl tyrosine as a suspending agent for SWCNT disables the aggregation of the nanotubes and more importantly it is completely removed from the composite film during the sintering process, not introducing any residual impurities in the electrode after annealing.

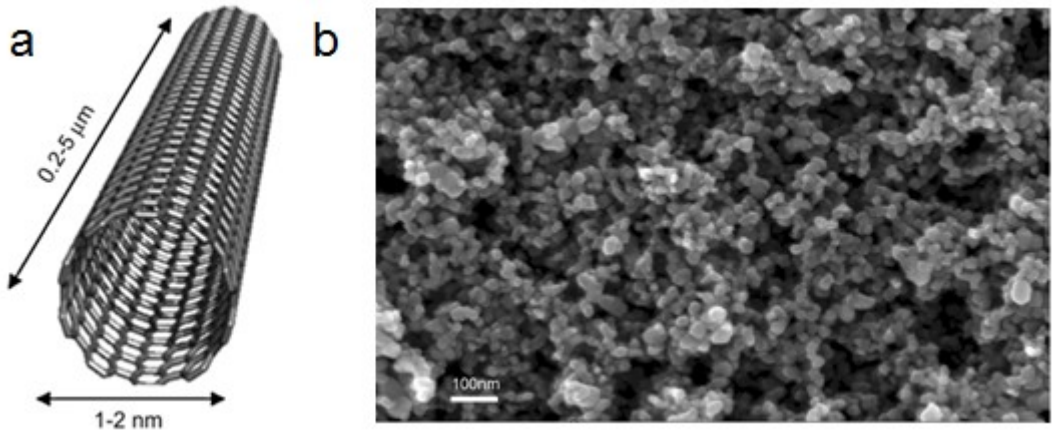

Figure 11. a) Graphic representation of a SWCNT; b) SEM image of cross section area of 0.04% SWCNT/TiO_2 film.

The SEM image in Figure 11b shows the morphology of the 0.04% SWCNT/TiO_2 film. Considering the size and the concentration of the nanotubes, there are no changes or distinctive features observed between the films with without SWCNT. The porosity and the morphology of the TiO_2 film does not seem to suffer from changes or difference in the interconnection of the nanoparticles, most likely due to the significantly different size in diameter of the nanotubes and the size of the TiO_2 nanoparticles (1-2 nm compared to 25-30 nm).

In order to confirm the presence and investigate the structural quality of the nanotubes in the photoanodes after the annealing process, Raman measurements were performed with respect to the SWCNT loading in the composite films. Raman maps of the SWCNT/TiO_2 composite mesoporous films are presented in Figure 12.

The Raman spectra of the nanotubes in the maps show consistency of the SWCNT loading in the films. It is clear that a good distribution of nanotubes is present throughout the TiO_2 composite films. The Raman spectra in Figure 12 (graph and inset) confirm that the SWCNT signal is present through the measured films.

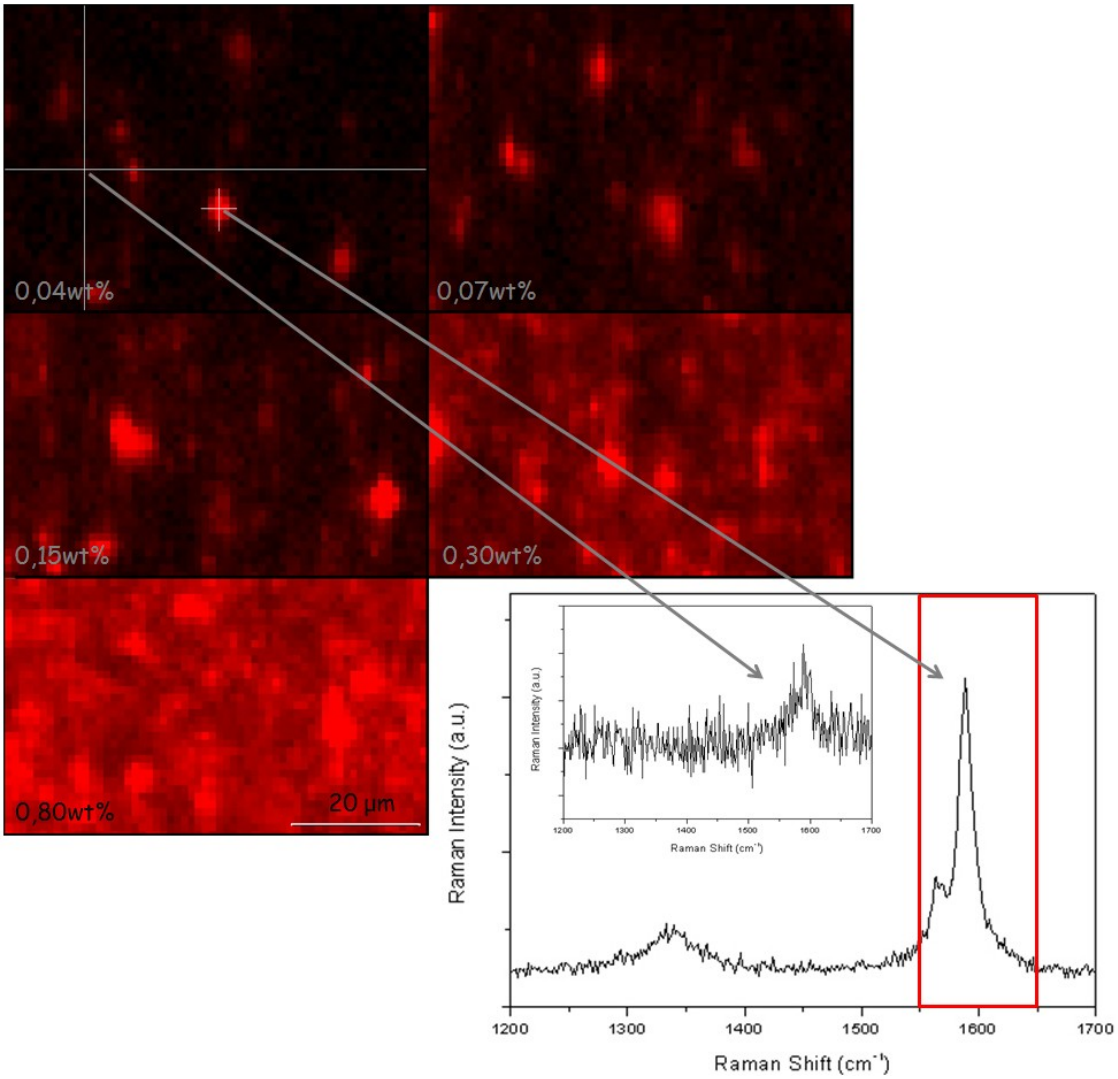

Figure 12. Raman maps SWCNT/TiO_2 films. Black to red color represents the increase of intensity of signal to noise ratio in the frequency region 1550-1650 cm^{-1}. The red spot corresponds to the Raman spectra of G^- and G^+ bands of SWCNT shown in the graph, the inset shows the Raman spectra of the G^+ band (black spot).

The low intensity of the characteristic Raman signal of the SWCNT in the inset indicates that the nanotubes are present not only on the surface of the films, but are well dispersed within the entire TiO_2 film. The signal of the characteristic D and G bands[52] indicates that there is no thermal or chemical degradation of the nanotubes as a result of preparation process. However, it can also be seen that at certain points the Raman signal of the nanotubes is quite intense which is a result of a larger amount of SWCNT in the same position, this is a fingerprint of aggregation of nanotubes which can be expected to a certain level since SWCNT are prone to bundle.

Once the morphology of the composite photoanode films was established, the essential electrical properties of the composite material were probed. The electrical conductivity of the SWCNT/TiO_2 films was measured in two contact architecture under 1 sun illumination. The results are resented in Figure 13.

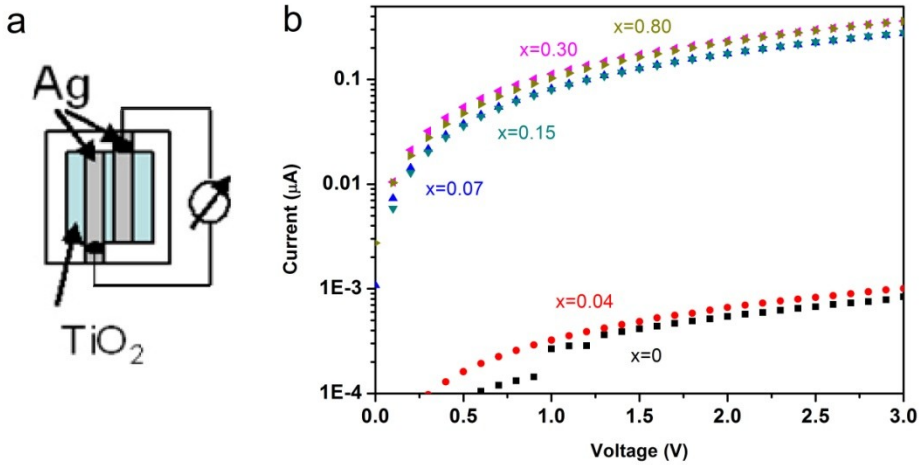

Figure 13. a) Shematic of electrode placement for the two contact *I-V* measurement; b) *I-V* curve for plain and SWCNT/TiO_2 films, *x* represents the percentage of the SWCNT/TiO_2 loading.

Two important conclusions about the difference in the conductivity of the composite photoanode films can be extracted. Namely, for the lowest SWCNT loading of 0.04% the conductivity didn't change significantly as oppose to the plain TiO_2 film, however for the higher loadings starting from 0.07-0.80% there is a large increase in conductivity of two orders of magnitude. The nonsignificant difference of the conductivity between films with higher loadings of nanotubes can be attributed to certain saturation in the conductivity for the composite system. The conductivity measurement under light implies that the electrons in the TiO_2 are no longer trapped and the conductivity is a result of a free electron transport within the film.

3.2.2. Investigation of DSC with Composite SWCNT/TiO_2 Photoanode

Confirming the composite structure and the enhanced electronic properties of the films justified the introduction of composite photoanodes in solar cell configuration. However, introducing higher concentration of nanotubes, such as the 0.80% SWCNT/TiO_2 loading, changes the color of the mesoporous film which becomes dark gray. Due to the functionality of the photoanode when illuminated and the property not to absorb or obstruct the light before it reaches the dye, this composite electrode was excluded from solar cell application. The DSC configuration is presented in Figure 6 of this chapter. The investigation of the solar cell efficiency with respect to the SWCNT/TiO_2 composite

photoanode is presented in Figure 14. Despite the increase in the conductivity of the standalone composite films, the efficiency of the DSC did not increase with the increased electron transport performance of the photoanode. In fact, the efficiency decreased significantly going to higher SWCNT loadings in the photoanode. Primarily one of the reasons for this efficiency decrease is most likely the increased recombination. Upon close investigation of the photoanode films as evidenced from the Raman maps (Figure 12), it can be noted that there is a widespread of nanotubes through the films, as well as, some bundles of nanotubes whose number increases with the increase of the SWCNT loading. Additionally, there could be a number of nanotubes which are most likely not covered by any TiO_2 nanoparticles and thus their nanotube walls are exposed to the electrolyte and act as direct recombination centers. Exposed nanotubes can also be in direct contact with the FTO and thus, it is of primal importance to isolate the nanotubes walls and ends from the FTO and reduce the interfacial recombination between the electrons from the photoanode and the electrolyte at this interface. In order to reduce this recombination, an electron selective layer i.e. a compact TiO_2 layer which acts as a buffer between the FTO and electrolyte was introduced (see Figure 15).

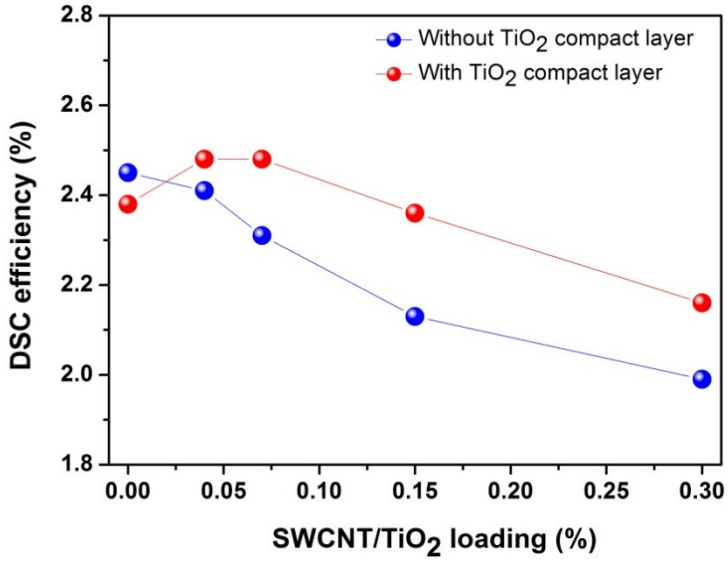

Figure 14. DSC efficiency dependence on SWCNT loading of the composite photoanode for solar cells with and without a TiO_2 compact layer.

The efficiency of the DSC with compact layer is also presented in Figure 14. The introduction of the compact layer resulted in several distinctive features. Primarily the solar cell constructed with a plain TiO_2 photoanode suffered a decrease in efficiency. This decrease in efficiency can be expected due to the fact that the compact layer is essentially a resistive element when employed in DSC configuration. Employing a compact layer in the DSC configuration with ruthenium dye and thick TiO_2 photoanode film is not a necessary element.[53] The compact layer essentially represents a tradeoff, introducing an additional series resistance to the electron charge transport via the TiO_2/FTO interface; as oppose to reducing the charge recombination via electrolyte/FTO interface. Furthermore, depending on the crystalline quality, porosity and electronic properties of the TiO_2 film and the adhesion of the TiO_2 mesoporous film to the FTO substrate, the latter reaction can have a smaller effect on the charge transport with respect to former reaction. However, increasing the loading of the SWCNT in the composite photoanode changes the balance of this dynamic tradeoff in favor of the compact layer which acts as a recombination buffer.

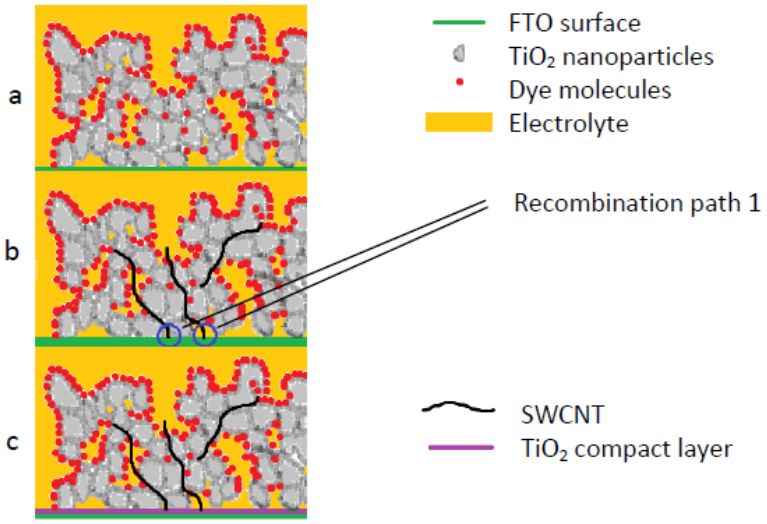

Figure 15. Cartoon of the DSC cross section; a) reference structure with a plain TiO_2 photoanode; b) cell with a composite SWCNT/TiO_2 photoanode and possible recombination path through FTO; c) cell employing a compact TiO_2 layer.

The efficiency of the solar cell employing a photoanode with 0.07% and especially 0.15% and 0.3% is significantly increased, meaning that the compact layer indeed has the effect of reducing the recombination minimizing the direct contact of the nanotubes at the FTO and the electrolyte at the FTO/mesoporous TiO_2 interface. Interestingly even though the efficiency for composite photoanodes increased for more that 10% with respect of the cells without and with a compact layer, the improvement of DSC efficiency was evidenced only for the lowest SWCNT loadings in the photoanode of 0.04 and 0.07%, whereas for the photoanodes with higher loadings, it was sill rather low with respect to the cell with plain TiO_2 photoanode. This can be a result of substantial SWCNT loading in the composite photoanode as evidenced by the Raman investigation (Figure 12), both with respect to uniform dispersion of nanotubes through the film and to the formation of bundles. The amount of uncovered nanotubes is probably much larger throughout the film with respect to the FTO/photoanode interface, as it is physically impossible to obtain complete coverage of SWCNT with diameters of 1-2 nm by TiO_2 grains of 20-30 nm size. Furthermore SWCNT bundles have previously been observed to support enhanced recombination.[14] Thus, the compact layer does not sufficiently account in improvement of efficiency since the reduced recombination at the FTO/TiO_2 interface is smaller with respect to the remaining recombination centers and processes.

In order to further retard the electron recombination through exposed nanotubes within the photoanode film and be able to exploit the benefits of the increased composite film conductivity, a second experiment was performed subjecting the composite photoanodes to the post-treatment with colloidal solution of nanoparticles presented in Section 2 of this chapter. For this purpose using the already improved solar cell configuration with a TiO_2 compact layer; twin solar cell devices without and with TiO_2 colloidal post-treatment and composite SWCNT/TiO_2 photoanodes were investigated in more detail.

The current-voltage characteristics of DSC with a composite photoanode and without colloidal post-treatment are presented in Figure 16. Their representative solar cell parameters are presented in Table 3.

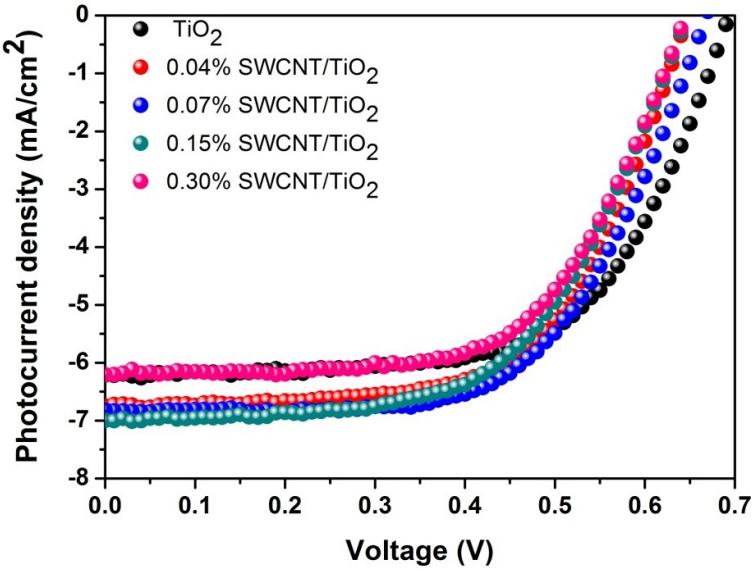

Figure 16. Current-voltage characteristics of DSC with different composite photoanodes with TiO_2 compact layer.

Table 3. Solar cell parameters of DSC with different composite photoanodes with TiO_2 compact layer represented in Figure 16.

Type of photoanode (P25)	J_{SC} (mA/cm^2)	V_{OC} (V)	*FF* (%)	η (%)
TiO_2	-6.21	0.69	63.12	2.70
0.04 % SWCNT/TiO_2	-6.75	0.65	61.59	2.70
0.07 % SWCNT/TiO_2	-6.82	0.67	61.03	2.79
0.15 % SWCNT/TiO_2	-7.00	0.65	57.83	2.63
0.30 % SWCNT/TiO_2	-6.21	0.64	62.16	2.47

From the parameters in Table 3 it is evident that increasing the SWCNT loading in the photoanode increases the current density for the DSC with the composite photoanode, especially for the 0.15% loading. The short circuit current density (J_{SC}) increase is associated with the mitigated electron mobility once the compact layer is introduced, as already discussed. However, further increase in the SWCNT concentration results in decrease of the current, supporting the theory of increased recombination through a larger number of uncovered SWCNT i.e. recombination centers. On the other hand, there is an evident decrease V_{OC} by increasing the photoanode SWCNT loading which in turn affects the overall cell efficiency. This decrease of V_{OC} has been investigated by Kongkanand and Kamat[54] to be a result of the Fermi level equilibration. In a cell configuration, the introduction of the SWCNT in the composite is causing charge equilibration between the TiO_2 and the SWCNT which in turn is lowering the Fermi level of the TiO_2 to a less negative value. Thus, although there is an increment in the photocurrent of more than 10% for the photoanode with 0.15% SWCNT loading, the dip in the V_{OC} with respect to the cell with a plain TiO_2 photoanode results in approximately same efficiency for these cells (Figure 14). A delicate improvement of DSC efficiency was only recorded for the 0.04 and 0.07% SWCNT photoanode loading.

To investigate the electron recombination OCVD measurements were performed. The decay curves as well as the calculated electron recombination time with respect to the V_{OC} are reported in Figure 17.

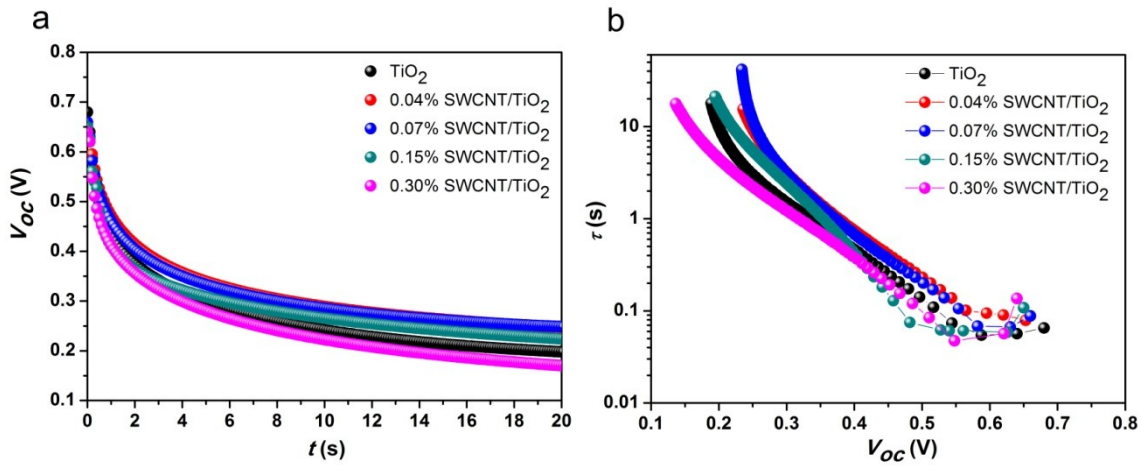

Figure 17. a) Open circuit voltage decay curves; b) Electron lifetime as a function of the V_{OC} of DSC with plain TiO_2 photoanode and SWCNT/TiO_2 composite photoanodes.

The decay curves in Figure 17a show a relaxation trend which matches the efficiency of the solar cells investigated (Table 3). Initially the V_{OC} decay is slowest for the cells with 0.04 and 0.07% SWCNT/TiO_2 photoanode, whereas the cells with the plain photoanode and the 0.15% SWCNT loading have almost identical decay times. The cell with the 0.30% SWCNT photoanode loading shows the fastest decay. Interestingly, there is difference in decay times for all cells mainly in the first few seconds which slowly evens out further with time. A closer inspection of the electron recombination time (refer to Appendix for the theoretical background) can be done through Figure 17b. It is evident that in the region of recombination through free electrons, the cells with composite photoanodes (except for the 0.15 and 0.30% SWCNT/TiO_2 photoanode) show slower recombination time. This could be a result of the electron storage capability of the SWCNT, where the electrons are being released first through the TiO_2 and then recombine. However, increasing the SWCNT loading and, as evidenced by the electron recombination time of the cell with the highest 0.30% loading SWCNT/TiO_2 photoanode, there is a strong implication that the excess of exposed nanotubes act as recombination centers thus speeding up the recombination. Further information of interest is that the recombination time is similar for all the cells when discussing the electron transport through bulk traps, which implies that the bulk trap states for the electron in the composite are governed by the TiO_2. Lastly, it can be noticed that the recombination through surface trap states is also shifted with respect to the composite electrodes, the recombination through surface trap states apparently starts at higher V_{OC} for the plain TiO_2 cell, oppose to the cells with the composite photoanode, and recombination through surface states is slightly faster for the former with the exception of the cell with the 0.30% SWCNT/TiO_2 photoanode.

To further increase the efficiency of the DSC employing SWCNT/TiO_2 photoanode, the coverage of the SWCNT has to be improved throughout the mesoporous photoanode to successfully reduce the recombination with the electrolyte within the cell. It is well known that the dye adsorption on the TiO_2 surface is not absolute hence there are certain areas which are not covered by dye molecules and can act as recombination centers. In a situation in which additionally there are SWCNT in direct contact with the electrolyte the recombination is increased. With this in mind applying a surface post-treatment to the photoanode would not only improve the surface trap states recombination, but it should

also provide an efficient coverage of SWCNT. The further decoration of the photoanode and the effect on the recombination mechanism are presented in Figure 18.

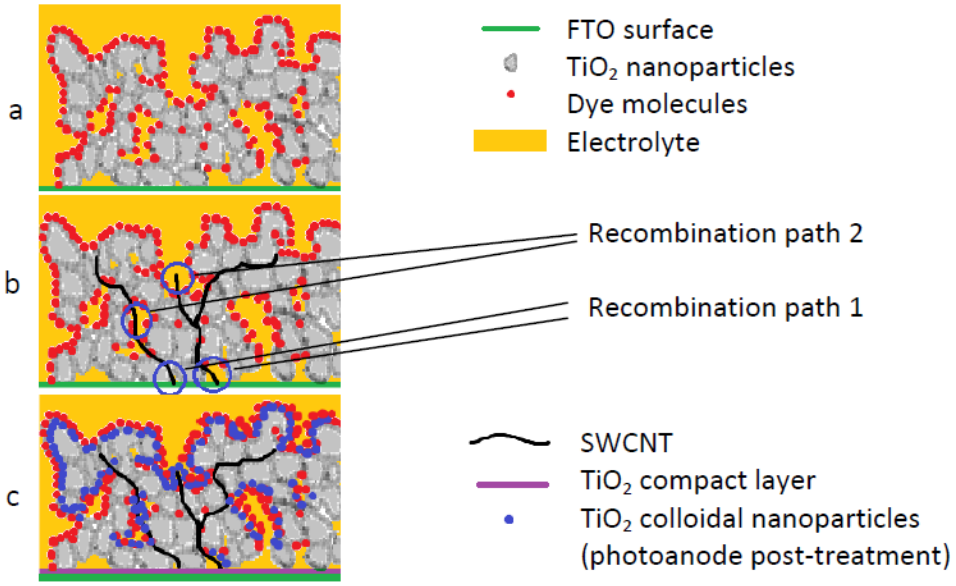

Figure 18. Cartoon of the DSC cross section; a) reference structure with a plain TiO_2 photoanode; b) cell with a composite SWCNT/TiO_2 photoanode and possible recombination paths; c) cell employing a compact TiO_2 layer and a TiO_2 colloidal post-treatment.

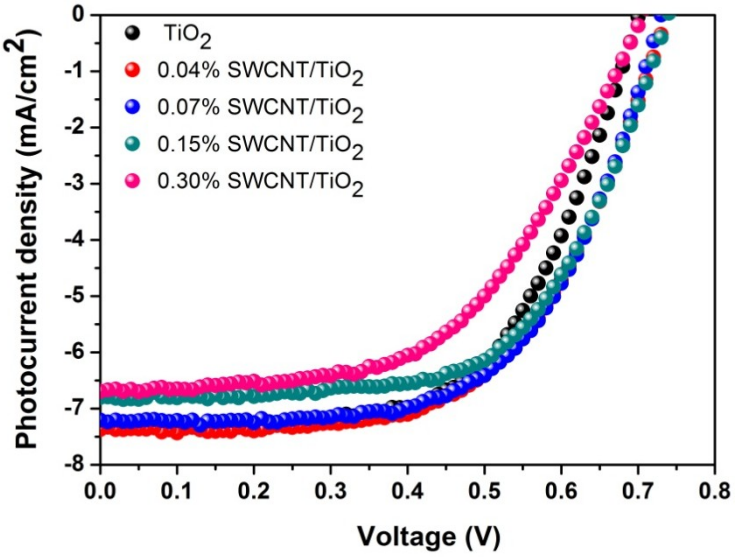

Figure 19. Current-voltage characteristics of DSC with different composite photoanodes with TiO_2 compact layer and TiO_2 colloidal post-treatment.

The current–voltage characteristics of the DSC with post-treated, composite SWCNT/TiO_2 photoanode are presented in Figure 19. The representative solar cell parameters are presented in Table 4.

Table 4. Solar cell parameter of DSC with different composite photoanodes with TiO_2 compact layer and TiO_2 colloidal post-treatment represented in Figure 19.

Type of photoanode (P25)	J_{SC} (mA/cm^2)	V_{OC} (V)	*FF* (%)	η (%)
TiO_2	-7.31	0.70	60.78	3.11
0.04 % SWCNT/TiO_2	-7.37	0.74	58.77	3.21
0.07 % SWCNT/TiO_2	-7.20	0.73	61.14	3.21
0.15 % SWCNT/TiO_2	-6.81	0.74	61.33	3.09
0.30 % SWCNT/TiO_2	-6.70	0.71	53.75	2.56

In comparison with the solar cell parameters presented in Table 3 it is evident that the post-treatment further increases the short circuit current. However, the increase with respect to the reference cell (plain TiO_2 photoanode) is less significant and evident only for the cell with 0.04% SWCNT/TiO_2 photoanode. Interestingly, the DSC efficiency increase is quite clear between the cells without and with post-treated composite photoanodes, confirming the results achieved and described in Section 2 of the chapter (Figure 20).

Notably the cells with the composite photoanode with the highest SWCNT loading again show the least increase in the efficiency and there is an even bigger discrepancy between the cells with plain and 0.30% composite photoanode.

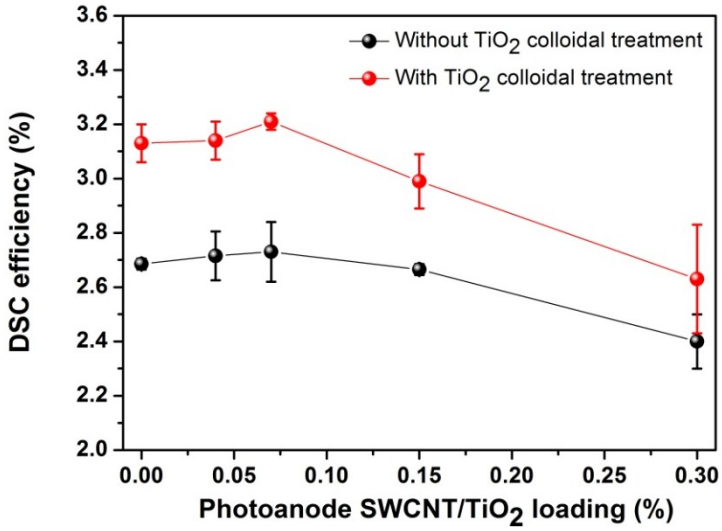

Figure 20. DSC with TiO_2 compact layer efficiency dependence on SWCNT loading of the composite photoanode with and without post-treatment.

The results in Figure 20 are averaged with respect to at least 4 equivalent solar cells (photoanode thickness of 12.2 ± 0.7 µm). It should be noted that the higher efficiency for the DSC without post-treatment presented in Figure 14, with respect to efficiency of the equivalent cells in Figure 20, is due to the larger thickness of the photoanode of around 2 µm in the current experiment, nevertheless the efficiency trend with respect to the photoanode SWCNT loading remains the same. It can be concluded that the peak efficiency is evidenced for the solar cells with 0.07% SWCNT/TiO_2 photoanode.

Achieving this efficiency increase confirms efficient coverage of the nanotubes and mitigated electron transport for the lower SWCNT loadings. Even though the J_{SC} did not

increase significantly after the post-treatment with respect SWCNT loading, there was another effect that influenced the overall efficiency. The impact of the Fermi level equilibration was reduced and there is a practically negligible drop of V_{OC} with respect to the increase in SWCNT loading of the photoanode, and a 30 mV increase for the cells with composite anode of 0.04, 0.07 and 0.15% SWCNT loadings. This can additionally be a result of the post-treatment effect on the surface trap states and not only on the nanotube coverage i.e. recombination centers.

To be able to collect further information on both the nanotubes and the post-treatment effect on the electron recombination via the electrolyte, OCVD measurements were performed and the electron lifetime was extracted. Figure 21a presents the V_{OC} decay curves for the cells with post-treated composite photoanodes. It is evident that for the cells with the composite photoanode the initial decay is faster than for the reference cell, whereas, the situation is opposite for the dynamics after the 10s mark. It is peculiar that the cell with the highest efficiency (0.07% SWCNT loading photoanode) has practically identical decay as the reference cell (plain TiO_2 photoanode). The electron lifetime shortens with increasing the SWCNT loading of the photoanodes regarding the free electron and bilk trap facilitated transport. The situation, on the contrary, is different for the surface trap states mitigated electron recombination. It is quite peculiar that cells with the post-treated composite photoanode have faster decay in comparison to the respective cells without a post-treatment (Figure 17); this result indicates that the charge transport dynamics of the electrons in the mesoporous photoanode could be governed by a series of effects which could be especially sensitive on the fundamental electronic properties of the photoanode material. This result confirms that the presence of the nanotubes in the photoanode changes the dynamical process of the charge recombination with respect to the plain TiO_2 photoanode.

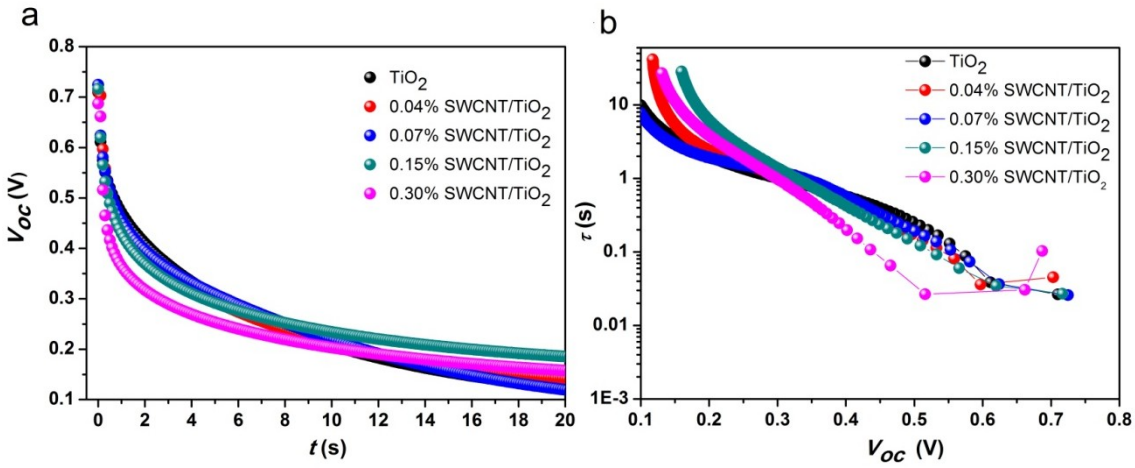

Figure 21. a) Open circuit voltage decay curves; b) Electron lifetime as a function of the V_{OC} of DSC with plain TiO_2 photoanode and SWCNT/TiO_2 composite photoanodes with post-treatment.

Furthermore, according to Chen *et al.*,[43] carbon nanotubes can facilitate electron transport in the low voltage range, whereas at the high voltage range the potential barrier for electron injection between the nanotube ad the TiO_2 in the composite photoanode becomes quite high and the charge leakage through the nanotubes becomes the predominant charge transport mechanism, which supports the presented experimental data on the electron recombination time.

One of the possible reasons however for the relatively low efficiency improvement of the composite photoanode DSC could also be the presence of metallic nanotubes. Having in mind that the SWCNT are composed of both metallic and semiconducting SWCNT, most

likely the metallic nanotubes facilitate the recombination as presented in Figure 22, and hinder the efficiency increase expected as a result of the photoanode conductivity increase.[15]

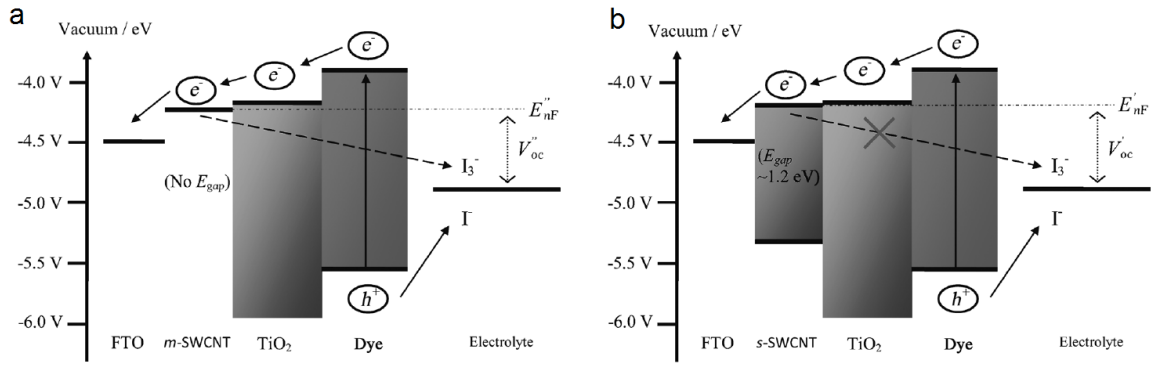

Figure 22. Energy band diagram of DSC with a) metallic; b) semiconducting SWCNT incorporated in the TiO_2 photoanode.[15]

In conclusion, the photovoltaic performance enhancement of the DSC was accomplished by introducing a post-treatment of the mesoporous SWCNT/TiO_2 films using a colloidal solution of TiO_2 nanoparticles. Coating the films has a dual outcome: eliminating the effect of the surface traps in the mesoporous TiO_2, and covering the unscreened SWCNT acting as recombination spots. However, the photovoltaic properties of DSC are extremely sensitive to the concentration of SWCNT in the mesoporous titania photoelectrode. Carefully increasing the SWCNT concentration effectively increases the I_{SC} and η which was found in a small interval of SWCNT loading around 0.07% where the V_{OC} , I_{SC} and η show higher values than the cells with plain TiO_2 electrode. Further increasing of the SWCNT concentration didn't translate to an increment in DSC efficiency. With relatively high nanotube contents the positive conductivity increase is outweighed by the electron-hole recombination which might be caused by metallic SWCNT. Due to their zero gap, the metallic SWCNT can act as recombination centres thus suppressing the photocurrent generation and lowering both V_{OC} and $I_{SC.}$ Having in mind the obtained results further investigations needs to be conducted using SWCNT with different metallic/semiconducting composition.

3.2.3. Investigation of SDSC with Composite SWCNT/TiO_2 Photoanode

The concept and mechanism of operation behind the solid state dye sensitized solar cell (SDSC) has been described in Chapter 1, Section 6. The investigation and implementation of the photoanode and engineering employed for the standard dye cell with liquid electrolyte, and the increment in efficiency and optimization can be confidently translated to the SDSC concept.

The main issue of the SDSC performance and photovoltaic properties is the infiltration of the hole conducting material in the photoanode. The requirement to reduce the thickness from 10-15 μm (for the DSC) to 1-2 μm, diminishes the effective surface of the mesoporous film and the amount of adsorbed dye, and in turn affects several charge transport and recombination properties. In the electrolyte cell, the iodide/triiodide redox couple has a strong over-potential at the FTO interface, thus there is a barrier which prevents the recombination of the photogenerated charges at the interface. In SDSC, the hole conducting material (spiro-OMeTAD) and FTO form ohmic contact, which means

that the charge carriers will recombine at this interface, resulting in an intrinsically inefficient solar cell. Hence, an additional blocking, compact TiO_2 layer between the FTO surface and the mesoporous photoanode is essential to avoid short-circuiting (prevents HCM from reaching FTO), and loss of current through recombination between FTO and p-type semiconductor. Due to the insufficient infiltration and pore filling, the contact between the HCM and the nanocrystalline/dye photoanode is a major drawback in the SDSC system. The problem arises from fast inevitable recombination processes occurring at TiO_2/dye and TiO_2/HCM interfaces.[1] Hence, the efficient operation of SDSC relies on the minimization of these recombination paths. The investigation target is therefore the enhancement of the charge transport and collection, especially the long-lasting charge separation as a key to the improvement of the photovoltaic properties of the SDSC or any other photovoltaic concept. This means that improving the electron transport through the TiO_2 can be essential for the extraction of the electrons into the external circuit and reducing the recombination.

The algorithm for photoanode improvement which was employed for the DSC can be easily translated to the solid state device. A cartoon of the solar cell configuration is presented in Figure 23. The current-voltage characteristics of the prepared devices with a composite photoanode are presented in Figure 24. The corresponding solar cell parameters are reported in Table 5.

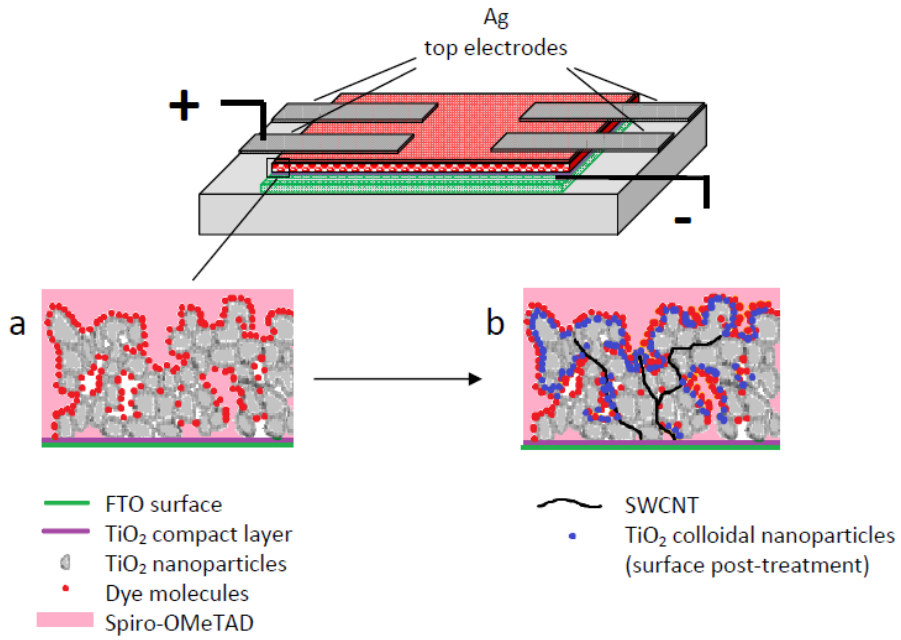

Figure 24. Cartoon of the SDSC solar cell configuration; Cross section of a) reference structure with a plain TiO_2 photoanode; b) cell with a composite SWCNT/TiO_2 photoanode and a TiO_2 colloidal post-treatment.

The significant difference in efficiency is between the DSC and the SDSC is mainly due to the significant reduction of the photoanode thickness. The achieved efficiency for SDSC configuration with N3 sensitizer and spiro-OMeTAD as a hole conducting material is in the range of reported results for this solar cell configuration.[55] As evidenced from Figure 24 and Table 5 there is an efficiency improvement for the solar cells prepared with the 0.04 and 0.07% SWCNT/TiO_2 photoanodes. The efficiency for the SDSC with the 0.15% SWCNT/TiO_2 photoanodes is similar to the solar cell with a plain TiO_2 photoanode. These results are corresponding well with the ones obtained for the DSC and discussed in the precious Section 3.2.2.

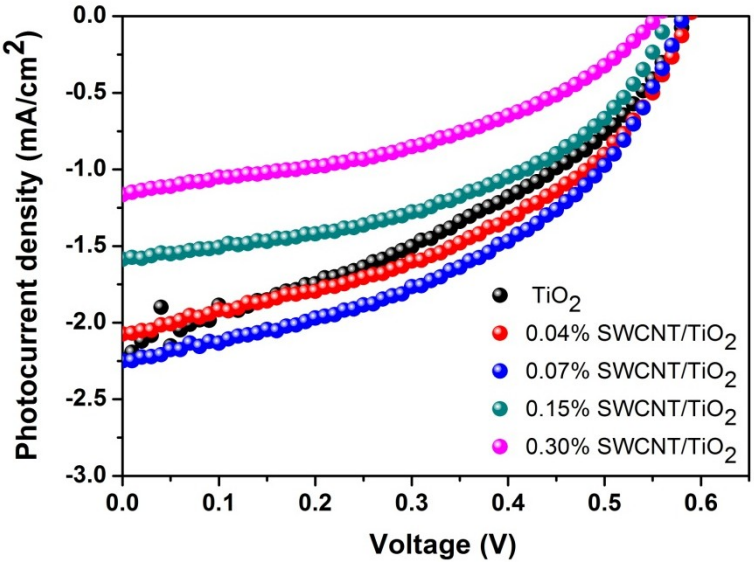

Figure 24. Current-voltage characteristics of SDSC with different composite photoanodes.

The highest efficiency improvement for the lower SWCNT loadings in the photoanode is around 20%, which in comparison with the DSC, is a quite notable efficiency increment. This result indicates that the improved conductivity in the photoanode has a stronger impact on systems with additional resistive elements, such as the photoanode/HCM interface (due to reduced recombination). As evident from the solar cell parameters from Table 5, the efficiency improvement is mainly due to the increase in the photocurrent. The introduction of the compact layer in the SDSC architecture as well as the lower thickness of the photoanode suggests that the increase in efficiency is due to the improvement in charge separation and collection, as a result of the incorporation of SWCNT. The difference in the efficiency increment of the solid, as oppose to the liquid electrolyte device is due to the smaller number of uncovered nanotubes which act as recombination centers. Nevertheless, one of the mitigating factors can also be the relatively insufficient interface between the HCM and the TiO_2 which can attribute to lower recombination via these SWCNT cites, and effectively improve the efficiency of the cell, turning this unwanted feature which results in low efficiency in favorable property when employing composite photoanodes.

Table 5. Solar cell parameters of SDSC with different composite photoanodes represented in Figure 24.

Type of photoanode (P25)	J_{SC} (mA/cm^2)	V_{OC} (V)	*FF* (%)	η (%)
TiO_2	-2.24	0.59	35.91	0.47
0.04 % SWCNT/TiO_2	-2.07	0.59	43.41	0.53
0.07 % SWCNT/TiO_2	-2.25	0.58	45.06	0.59
0.15 % SWCNT/TiO_2	-1.59	0.57	46.52	0.42
0.30 % SWCNT/TiO_2	-1.16	0.56	40.96	0.27

As evidenced from the solar cell parameters, the lowering of the Fermi level of the photoanode with increasing the SWCNT content is present in the solid device as well.

Since the TiO_2 colloidal post-treatment subsequently improved the charge transport in the DSC with the composite photoanode, the same methodology was employed for the photoanode for the SDSC investigation. The efficiency of the solar cells changed with respect to the cells without the post-treatment. The *I-V* curves of the SDSC with composite photoanode and colloidal post-treatment are presented in Figure 25. It is evident that the efficiency of all devices increased with respect to the one without the post-treatment. However, post-treating the photoanode resulted in efficiency increase of 20% for the 0.15% SWCNT/TiO_2 photoanode while for the 0.04 and 0.07% there was a slight drop and insignificant change with respect to the plain photoanode. Inspecting more closely the solar cell parameters of these devices, reported in Table 6, it can be seen that the short circuit current increased, especially for the 0.15% cell. This indicates that the mitigated electron transport due to the SWCNT loading needs to be finely balanced with respect to the certain additional resistive elements that could be present due to the TiO_2 post treatment.

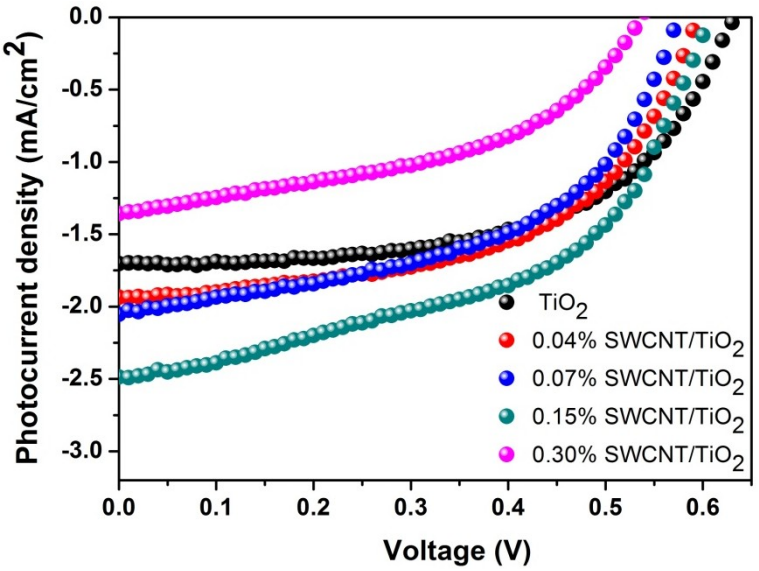

Figure 25. Current-voltage characteristics of SDSC with different composite photoanodes with TiO_2 colloidal post-treatment.

Table 6. Solar cell parameters of SDSC with different composite photoanodes represented in Figure 25.

Type of photoanode (P25)	J_{SC} (mA/cm^2)	V_{OC} (V)	*FF* (%)	η (%)
TiO_2	-1.70	0.63	57.58	0.62
0.04 % SWCNT/TiO_2	-1.93	0.59	55.21	0.63
0.07 % SWCNT/TiO_2	-2.05	0.57	51.21	0.60
0.15 % SWCNT/TiO_2	-2.49	0.61	50.34	0.76
0.30 % SWCNT/TiO_2	-1.36	0.54	45.33	0.33

In Section 2 of this chapter a detailed study of the morphology of the photoanode before and after post-treatment was investigated, however one has to keep in mind that the difference in thickness between these two photoanodes is 10 times, thus the post-treatment could have different implications of the morphology and the porosity of the photoanode for SDSC, especially considering the HCM infiltration which could be affected much more

than a liquid electrolyte by any slight change in the porosity of the photoanode. The V_{OC} of the solar cells with post-treated photoanode did not experience an increase; this can be an indication of a additional resistive element in the cell, thus despite of reducing the recombination and increasing the photocurrent, the post-treatment might cause a trade-off between the V_{OC} and I_{SC}, which could result in the shift in efficiency increase of the solar cells from 0.07 to 0.15%, as reported in Figure 26. The efficiency of the cells with 0.04 and 0.07% SWCNT/TiO_2 photoanode before and after the post-treatment didn't change indicating that the post-treatment either had no effect on the charge transport or that to dynamical processes of reduced recombination at the SWCNT/HCM and increased recombination at TiO_2/HCM effectively cancel each other.

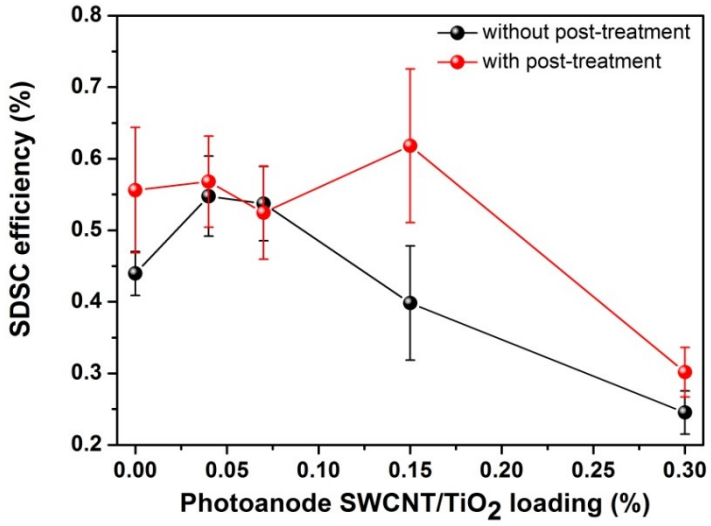

Figure 26. SDSC dependence on SWCNT loading of the composite photoanode with and without post-treatment.

The detailed investigation of the influence of the conductivity of the photoanode on both liquid and solid dye sensitized solar cells has shown that indeed for low SWCNT loadings in the photoanode, an increase of efficiency of up to 10% can be reproductively achieved. However, certain effects of changes of the electronic properties of the TiO_2 when incorporating SWCNT have to be taken into account when investigating solar cells and not standalone composite films. Since a solar cell is a layered device where charge generation, separation and transport depends on the energy levels and dynamical processes at least 4 interfaces the appropriate modeling of the charge transport when incorporating composite materials needs to be subjected to additional fundamental research.

Considering that all sensitized solar cell concepts should generally benefit from increased charge transport through the TiO_2 mesoporous photoanode further experiments were made incorporating the composite photoanode in the perovskite solar cell architecture.

3.2.4. Investigation of PSC with Composite SWCNT/TiO_2 Photoanode

Increasing the low mobility of electrons and facilitating the electron transport through the mesoporous TiO_2 photoelectrode could be a positive feature for the perovskite solar cell in mesoporous configuration, since it has been reported that the electron diffusion through the Cl-doped $CH_3NH_3PbI_3$ (MAPI) is much faster than through the mesoporous titania.[56] With this aim, in order to reduce the series resistance of the system, investigation on how low

amounts of SWCNT loadings in the mesoporous TiO_2 photoanode matrix would change the perovskite solar cell parameters was performed.

The perovskite solar cell (PSC) in a mesoporous configuration i.e. where the perovskite material is acting as a sensitizer of the mesoporous TiO_2 photoanode has similar concept of charge generation and transport mechanisms as the SDSC.[57] The basic operational principle and the specific features of the PSC have been addressed in Chapter I, Section 7. An animated image of the PSC configuration and cross section is presented in Figure 27. Since the electron mobility of the perovskite is around 35 cm^2/Vs[58] (at room temperature) in contrast to the Spiro-OMeTAD hole mobility which is about 4 orders of magnitude slower,[59] delicate differences of the perovskite precursor solution concentration were also taken into account.[60] The idea was to study how the change in the perovskite infiltration by using a less concentrated solution which can easily infiltrate the mesoporous photoanode; or the overlayer thickness which can form by using a more concentrated solution can affect the electron transport with respect to the composite SWCNT/TiO_2 photoanode. Considering the previous results of the implementation of the SWCNT/TiO_2 photoanode for DSC and SDSC intuitively the investigation with the perovskite solar cells was focused on the lower loadings of carbon nanotubes in the TiO_2 (0.04; 0.07 and 0.15%).

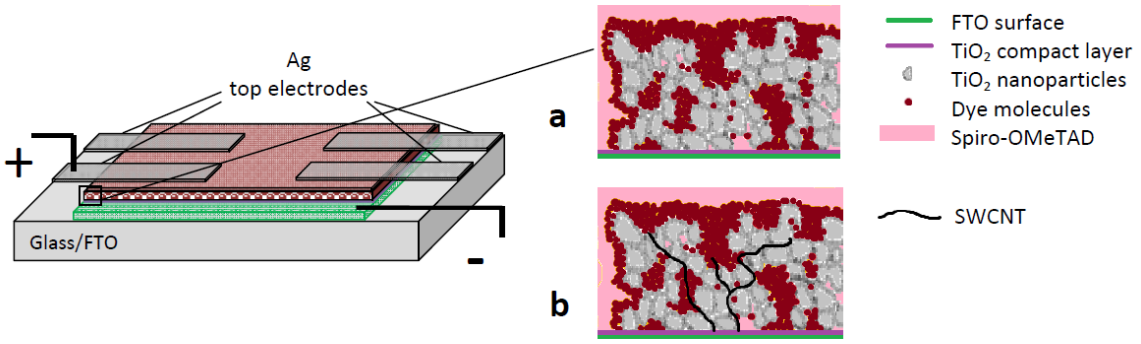

Figure 27. Cartoon of the PSC architecture; a cross section of a) reference structure with a plain TiO_2 photoanode; b) cell with a composite SWCNT/TiO_2 photoanode.

The current-voltage characteristics of the solar cells from the same batch, with photoanode thickness of 0.5±0.8 µm, are presented in Figure 28.

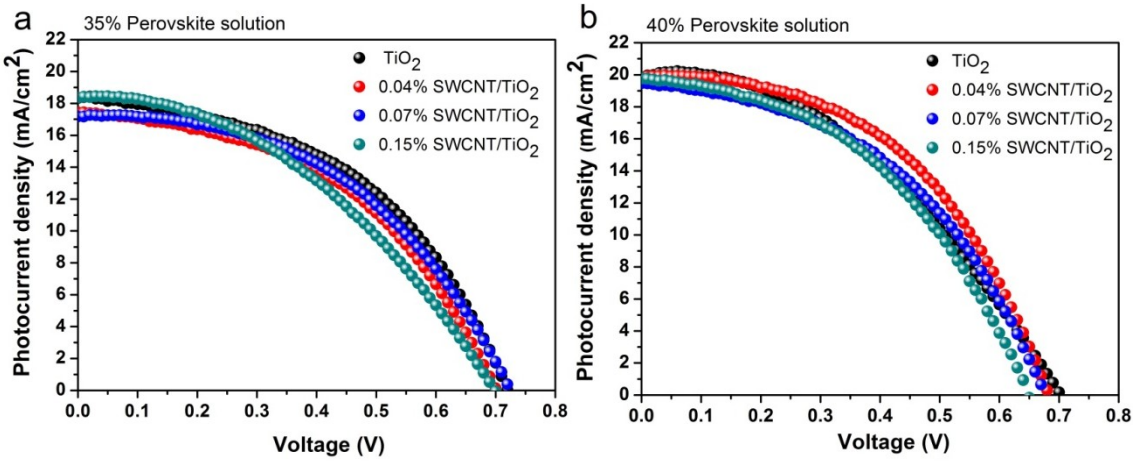

Figure 28. Current-voltage measurements of PSC prepared with a composite photoanode from a) 35% perovskite solution; b) 40% perovskite solution.

The difference in the precursor solution concentration can have implication on the pore filling and the perovskite overlayer thickness. Since a lower perovskite solution concentration will ensure a better infiltration of the perovskite and better interconnectivity of the mesoporous photoanode, the active material charge transport should be more efficient. On the other hand employing a higher solution concentration will provide a perovskite overlayer which will efficiently separate the TiO_2 and the HCM. The solar cell parameters of the cells presented in Figure 28, are reported in Table 7 and Table 8.

Table 7. Solar cell parameter of PSC with different composite photoanodes prepared from 35% perovskite solution represented in Figure 28a.

Type of photoanode (P25)	J_{SC} (mA/cm^2)	V_{OC} (V)	*FF* (%)	η (%)
TiO_2	18.31	-0.72	47.45	6.2
0.04 % SWCNT/TiO_2	17.44	-0.71	46.12	5.7
0.07 % SWCNT/TiO_2	19.44	-0.71	42.71	5.9
0.15 % SWCNT/TiO_2	18.38	-0.70	41.04	5.3

Table 8. Solar cell parameter of PSC with different composite photoanodes prepared from 40% perovskite solution represented in Figure 28b.

Type of photoanode (P25)	J_{SC} (mA/cm^2)	V_{OC} (V)	*FF* (%)	η (%)
TiO_2	19.81	-0.70	41.46	5.7
0.04 % SWCNT/TiO_2	19.75	-0.68	49.24	6.6
0.07 % SWCNT/TiO_2	19.50	-0.68	45.21	6.0
0.15 % SWCNT/TiO_2	19.75	-0.65	44.60	5.7

The efficiency of the presented solar cells with and without the composite photoanode, regardless of the concentration of the perovskite solution, varies within 15%. Several characteristic differences can be observed regarding the J_{SC} and V_{OC} of the representative cells. Namely, all the cells suffer a drop in the V_{OC} with increasing the concentration of SWCNT in the photoanode which has already been discussed. The trend of the Femi level lowering is present for the composite photoanode regardless of the sensitizing material. However, the V_{OC} of the solar cells prepared with the more concentrated solution of 40% experience a drop between 20-50 mV with respect to the cells prepared with the 35% perovskite solution. This decrease indicates lower pore filling of the mesoporous photoanode with the perovskite material, and possibly low interconnection of the TiO_2/MAPI interface. However, the high J_{SC} indicates that despite this issue the electron transport does not seem to be affected. Parallel mechanisms of diminished electron transport due to a bad TiO_2/MAPI interface and reduced recombination between TiO_2/HCM due to the perovskite overlayer could be at play.

Investigation of electron recombination was performed by OCVD measurement and analysis. The decay curves of the solar cells presented in Figure 28 are reported in Figure 29.

The open circuit voltage decay in the perovskite solar cells is quite fast during the first few hundreds of milliseconds. It can be noticed that the fast voltage decay is characteristic for the cells with all types of photoanode. When discussing the transient behavior of the PSC in order to extract information on the electronic processes in the solar cell, the polarization of the perovskite material needs to be taken into account. Thus, when discussing the time transients of the PSC it is necessary to consider both the decay of the non equilibrium careers and the polarization.[61] During the OCVD measurement, after removing the electronic driving force (illumination), the recombination of the carriers is very fast in the order of magnitude of ms, while the polarization decays to the equilibrium position much slower. From Figure 29 it is evident that for all types of solar cells the decay in the first hundred ms is very fast. Unfortunately, due to the resolution of the measurement it is not possible to extract any information on the shape of the decay curve in the region which is responsible for the fast phenomena such as recombination of electrons and holes. In this sense it is not reliable to predict the effect of SWCNT loading in the photoanode on the electron dynamics at the TiO_2/MAPI, TiO_2/HCM interfaces. The longer time decay (0.3s < t < 100s), responsible for dielectric relaxation of the perovskite active layer, was not subjected to study and interpretation at this point. It should be noted that small discrepancies of the V_{OC} values reported in Table 8 and Figure 29 for the corresponding cells could be a result of the previously reported in literature slow response of the perovskite solar cells in reaching study state conditions, hysteresis and light soaking behaviour[62,63] which are not taken into account for the purpose of this investigation (experimental setup and conditions), since essentially they do not influence the results within the investigated time resolution.

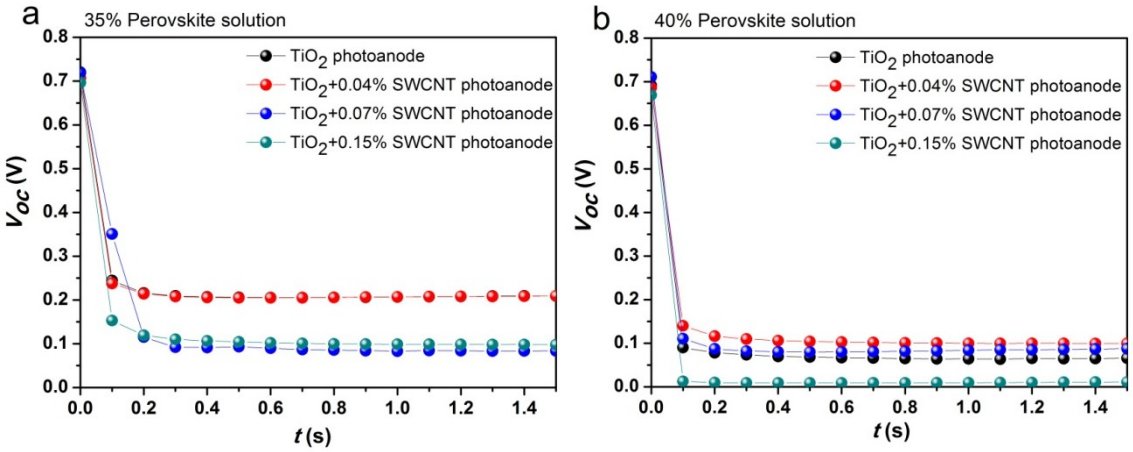

Figure 29. Open circuit voltage decay curves of PSC prepared with composite photoanode from a) 35% perovskite solution; b) 40% perovskite solution.

To conclude the influence of the SWCNT loading of the photoanode on the efficiency of the perovskite solar cells, several batches of cells were prepared and measured, and the results of their efficiency are presented in Figure 30.

The low concentrations of SWCNT in the photoanodes are not leading to an improvement in the cell efficiency when in condition of good perovskite infiltration and without an overlayer i.e., 35% precursor solution. This is probably due to the fast transport properties of the perovskite for both type of carriers (transport is more efficient through the perovskite than via the SWCNT decorated titania). For solar cells with an overlayer and possibly worse infiltration i.e., 40%, a slight trend in efficiency improvement was observed for cells with lowest loadings of SWCNT in the photoanode.

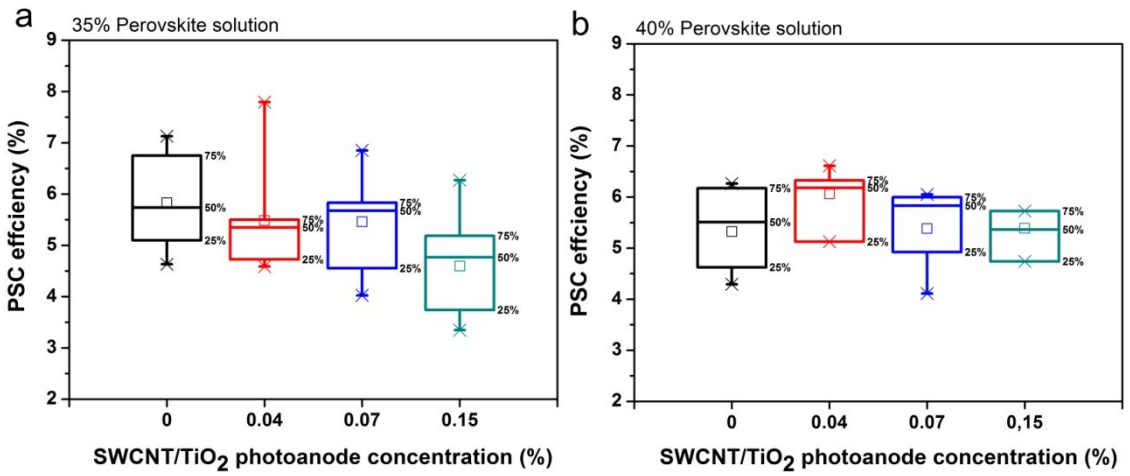

Figure 30. PSC efficiency dependence on SWCNT loading of the composite photoanode for solar cells prepared from a) 35% perovskite solution; b) 40% perovskite solution.

The addition of SWCNT in the mesoporous photoanode scaffold for the Cl-doped $CH_3NH_3PbI_3$ perovskite solar cell does not make significant change in the solar cell parameters and overall efficiency. This is a result of fast charge transport inside the perovskite which is not influenced by the presence of nanotubes within the titania scaffold. In conditions of poorer infiltration of the perovskite, the effect of the transport within the titania layer is no more negligible inducing a slight increase of the efficiency for the cells with 0.04% SWCNT loaded photoanodes. At higher SWCNT concentrations electron-hole recombination is also occurring.

3.3. Conclusion

The influence of the SWCNT on the conductivity of SWCNT/TiO_2 electrodes and the consequences on the photovoltaic efficiency and characteristics of three types of solar cells were investigated. The conductivity of the mesoporous composite photoanode was improved for SWCNT/TiO_2 concentration larger than 0.04% by two orders of magnitude.

Application of the composite photoanode in solar cell configuration resulted in an efficiency improvement within 0.04-0.15% SWCNT/TiO_2 composite photoanodes with respect to the solar cell technology and preparation conditions.

The improvement and optimization of the dye sensitized solar cell was achieved by employing both a compact TiO_2 layer and a photoanode post-treatment. Even though the effect of the conductivity enhancement of the photoanode was not translated to the solar cell, a fine efficiency improvement of around 5% was recorded for the cells employing the 0.07% SWCNT/TiO_2 photoanode. Although reports on similar approaches for efficiency improvement in DSC by employing MWCNT/TiO_2 composite photoanode show highest efficiency increments of 15-25% with respect to plain TiO_2 photoanodes,[42,43] the presented results correspond well with respect to studies on the impact of SWCNT type on the efficiency.[14,15] The use of mixture of both metallic and semiconducting SWCNT in the present investigation reflects the opposite efficiency impact that both types of nanotubes have on the photovoltaic performance which results in a delicate efficiency augmentation for the DSC.

For the solid state dye sensitized solar cell the efficiency improvement due to the superior conductivity of the 0.07% for SWCNT/TiO_2 photoanode was accomplished, whereas,

introducing a post-treatment resulted in efficiency improvement, for cells employing 0.15% SWCNT/TiO_2 photoanode, of approximately 50% with respect to the cells with a bare TiO_2 electrode.

The efficiency improvement in the perovskite solar cell followed the trend of least influence of improved photoanode conductivity on solar cell parameters; however, for the 40wt% perovskite solution and 0.04% SWCNT/TiO_2 photoanode an efficiency improvement of around 5% was achieved.

The obtained results indicate that the faster electron collection and transport in the photoelectrode, is weakened by the elevated recombination through possible SWCNT recombination centres. Introducing additional SWCNT decoration by photoanode post-treatment confirms this hypothesis by shifting of the maximum efficiency vs. SWCNT concentration in solid state DSC. Additional issue that needs to be addressed is the lowering of the Fermi level of the photoanode by increasing the SWCNT concentration in the composite photoanode which was confirmed by the experimental results of the solar cell parameters. The electron transport and recombination in the perovskite solar cell has a relatively more complicated reaction dynamics due to the fast charge transfer though the perovskite material of both electrons and holes, as well as the intrinsic structural properties of the perovskite material which give rise to a variety of phenomena such as polarization and ion migration[64,65], thus understanding the fine effect of SWCNT incorporation needs to be further investigated.

An increase of efficiency was evidenced for all three solar cell technologies with respect to plain TiO_2 photoanode reference cells, even though a breakthrough improvement was not recorded within the expected experimental parameters for solar cell preparation. These results are encouraging and further investigation should be concentrated in eliminating metallic SWCNT and working within a small window of SWCNT concentration (0-0.1% SWCNT/TiO_2) for best optimization.

4. Bibliography

1. Karthikeyan, C. S. & Thelakkat, M. Key aspects of individual layers in solid-state dye-sensitized solar cells and novel concepts to improve their performance. *Inorganica Chim. Acta* **361,** 635–655 (2008).
2. Shen, Q. & Toyoda, T. Studies of optical absorption and electron transport in nanocrystalline TiO_2 electrodes. *Thin Solid Films* **438-439,** 167–170 (2003).
3. Lau, S. T. C., Dayou, J., Sipaut, C. S. & Mansa, R. F. Development in Photoanode Materials for High Efficiency Dye Sensitized Solar Cells. *Int. J. Renew. Energy Res.* **4,** (2014).
4. J. Frank, A., Kopidakis, N. & Lagemaat, J. van de. Electrons in nanostructured TiO_2 solar cells: transport, recombination and photovoltaic properties. *Coord. Chem. Rev.* **248,** 1165–1179 (2004).
5. Subramanian, A., Ho, C.-Y. & Wang, H. Investigation of various photoanode structures on dye-sensitized solar cell performance using mixed-phase TiO_2. *J. Alloys Compd.* **572,** 11–16 (2013).
6. De Marco, L. *et al.* High-quality photoelectrodes based on shape-tailored TiO_2 nanocrystals for dye-sensitized solar cells. *J. Mater. Chem.* **21,** 13371 (2011).
7. Anta, J. A., Nelson, J. & Quirke, N. Charge transport model for disordered materials: Application to sensitized TiO_2. *Phys. Rev. B* **65,** 125324 (2002).
8. Tiwana, P., Docampo, P., Johnston, M. B., Snaith, H. J. & Herz, L. M. Electron Mobility and Injection Dynamics in Mesoporous ZnO, SnO_2 , and TiO_2 Films Used in Dye-Sensitized Solar Cells. *ACS Nano* **5,** 5158–5166 (2011).
9. Hsiao, P., Tung, Y. & Teng, H. Electron Transport Patterns in TiO_2 Nanocrystalline Films of Dye-Sensitized Solar Cells. *J. Phys. Chem. C* **114,** 6762–6769 (2010).
10. Van de Lagemaat, J. & Frank, A. J. Nonthermalized Electron Transport in Dye-Sensitized Nanocrystalline TiO_2 Films: Transient Photocurrent and Random-Walk Modeling Studies. *J. Phys. Chem. B* **105,** 11194–11205 (2001).
11. Dupuis, A.-C. Sensitized and perovskite solar cells how to capitalize on the developments of the photoanode and the hole transport material.
12. Antila, L. J., Santomauro, F. G., Hammarström, L., Fernandes, D. L. a. & Sá, J. Hunting for the elusive shallow traps in TiO_2 anatase. *Chem. Commun.* **51,** 10914–10916 (2015).
13. Park, N.-G. Dye-Sensitized Metal Oxide Nanostructures and Their Photoelectrochemical Properties. *J. Korean Electrochem. Soc.* **13,** 10–18 (2010).
14. Dang, X. *et al.* Virus-templated self-assembled single-walled carbon nanotubes for highly efficient electron collection in photovoltaic devices. *Nat. Nanotechnol.* **6,** 377–384 (2011).
15. Guai, G. H., Li, Y., Ng, C. M., Li, C. M. & Chan-Park, M. B. TiO_2 Composing with Pristine, Metallic or Semiconducting Single-Walled Carbon Nanotubes: Which Gives the Best Performance for a Dye-Sensitized Solar Cell. *ChemPhysChem* **13,** 2566–2572 (2012).
16. Dubey, M., Shrestha, M., Zhong, Y., Galipeau, D. & He, H. TiO_2 nanotube membranes on transparent conducting glass for high efficiency dye-sensitized solar cells. *Nanotechnology* **22,** 285201 (2011).
17. Crossland, E. J. W. *et al.* Mesoporous TiO_2 single crystals delivering enhanced mobility and optoelectronic device performance. *Nature* **495,** 215–219 (2013).
18. Li, T. C. *et al.* Surface Passivation of Nanoporous TiO_2 via Atomic Layer Deposition of ZrO_2 for Solid-State Dye-Sensitized Solar Cell Applications. *J. Phys. Chem. C* **113,** 18385–18390 (2009).
19. Fabregat-Santiago, F. *et al.* The origin of slow electron recombination processes in

dye-sensitized solar cells with alumina barrier coatings. *J. Appl. Phys.* **96,** 6903 (2004).
20. Palomares, E., Clifford, J. N., Haque, S. a, Lutz, T. & Durrant, J. R. Control of Charge Recombination Dynamics in Dye Sensitized Solar Cells by the Use of Conformally Deposited Metal Oxide Blocking Layers. *J. Am. Chem. Soc.* **125,** 475–482 (2003).
21. Lee, S.-W., Ahn, K.-S., Zhu, K., Neale, N. R. & Frank, A. J. Effects of TiCl 4 Treatment of Nanoporous TiO_2 Films on Morphology, Light Harvesting, and Charge-Carrier Dynamics in Dye-Sensitized Solar Cells. *J. Phys. Chem. C* **116,** 21285–21290 (2012).
22. Vesce, L. *et al.* Optimization of nanostructured titania photoanodes for dye-sensitized solar cells: Study and experimentation of TiCl4 treatment. *J. Non. Cryst. Solids* **356,** 1958–1961 (2010).
23. Sommeling, P. M. *et al.* Influence of a TiCl 4 Post-Treatment on Nanocrystalline TiO_2 Films in Dye-Sensitized Solar Cells. *J. Phys. Chem. B* **110,** 19191–19197 (2006).
24. O'Regan, B. C., Durrant, J. R., Sommeling, P. M. & Bakker, N. J. Influence of the TiCl 4 Treatment on Nanocrystalline TiO_2 Films in Dye-Sensitized Solar Cells. 2. Charge Density, Band Edge Shifts, and Quantification of Recombination Losses at Short Circuit. *J. Phys. Chem. C* **111,** 14001–14010 (2007).
25. Ito, S. *et al.* Control of dark current in photoelectrochemical (TiO_2/I^- –I_3^-) and dye-sensitized solar cells. *Chem. Commun.* 4351 (2005). doi:10.1039/b505718c
26. Rajh, T., Ostafin, A. & Micic, O. Surface modification of small particle TiO_2 colloids with cysteine for enhanced photochemical reduction: an EPR study. *J. Phys. Chem.* **100,** 4538–4545 (1996).
27. Thompson, R. C. Oxidation of peroxotitanium (IV) by chlorine and cerium (IV) in acidic perchlorate solution. *Inorg. Chem.* **23,** 1794–1798 (1984).
28. Jeffery, G. ., Bassett, J., Mendham, J. & Denney, C. *Vogel's Textbook of Quantitative Chemical Analysis*. (Wiley, New York, NY, USA, 1989).
29. Kelly, S., Pollak, F. H. & Tomkiewicz, M. Raman Spectroscopy as a Morphological Probe for TiO_2 Aerogels. *J. Phys. Chem. B* **101,** 2730–2734 (1997).
30. Trupke, T., Würfel, P. & Uhlendorf, I. Dependence of the Photocurrent Conversion Efficiency of Dye-Sensitized Solar Cells on the Incident Light Intensity. *J. Phys. Chem. B* **104,** 11484–11488 (2000).
31. Zhang, D., Downing, J. a, Knorr, F. J. & McHale, J. L. Room-Temperature Preparation of Nanocrystalline TiO_2 Films and the Influence of Surface Properties on Dye-Sensitized Solar Energy Conversion. *J. Phys. Chem. B* **110,** 21890–21898 (2006).
32. Liu, W. *et al.* The effect of the series resistance in dye-sensitized solar cells explored by electron transport and back reaction using electrical and optical modulation techniques. *Electrochim. Acta* **55,** 2338–2343 (2010).
33. Zaban, A., Greenshtein, M. & Bisquert, J. Determination of the Electron Lifetime in Nanocrystalline Dye Solar Cells by Open-Circuit Voltage Decay Measurements. *ChemPhysChem* **4,** 859–864 (2003).
34. Bisquert, J., Zaban, A., Greenshtein, M. & Mora-Serot, I. Determination of Rate Constants for Charge Transfer and the Distribution of Semiconductor and Electrolyte Electronic Energy Levels in Dye-Sensitized Solar Cells by Open-Circuit... *J. Am. Chem. Soc.* **126,** 13550–13559 (2004).
35. Kambe, S., Nakade, S., Kitamura, T., Wada, Y. & Yanagida, S. Influence of the Electrolytes on Electron Transport in Mesoporous TiO_2 −Electrolyte Systems. *J. Phys. Chem. B* **106,** 2967–2972 (2002).
36. Nakade, S. *et al.* Role of Electrolytes on Charge Recombination in Dye-Sensitized

TiO_2 Solar Cell (1): The Case of Solar Cells Using the I - /I 3 - Redox Couple. *J. Phys. Chem. B* **109,** 3480–3487 (2005).
37. Li, R., Liu, J., Cai, N., Zhang, M. & Wang, P. Synchronously Reduced Surface States, Charge Recombination, and Light Absorption Length for High-Performance Organic Dye-Sensitized Solar Cells. *J. Phys. Chem. B* **114,** 4461–4464 (2010).
38. Cameron, P. J. & Peter, L. M. How does back-reaction at the conducting glass substrate influence the dynamic photovoltage response of nanocrystalline dye-sensitized solar cells? *J. Phys. Chem. B* **109,** 7392–8 (2005).
39. Docampo, P., Guldin, S., Steiner, U. & Snaith, H. J. Charge Transport Limitations in Self-Assembled TiO_2 Photoanodes for Dye-Sensitized Solar Cells. *J. Phys. Chem. Lett.* **4,** 698–703 (2013).
40. Yang, N., Zhai, J., Wang, D., Chen, Y. & Jiang, L. Two-Dimensional Graphene Bridges Enhanced Photoinduced Charge Transport in Dye-Sensitized Solar Cells. *ACS Nano* **4,** 887–894 (2010).
41. Kim, A.-Y. *et al.* Photovoltaic Efficiencies on Dye-Sensitized Solar Cells Assembled with Graphene-Linked TiO_2 Anode Films. *Bull. Korean Chem. Soc.* **33,** 3355–3360 (2012).
42. Dembele, K. T. *et al.* Hybrid Carbon Nanotubes–TiO_2 Photoanodes for High Efficiency Dye-Sensitized Solar Cells. *J. Phys. Chem. C* **117,** 14510–14517 (2013).
43. Chen, J., Li, B., Zheng, J., Zhao, J. & Zhu, Z. Role of Carbon Nanotubes in Dye-Sensitized TiO_2 -Based Solar Cells. *J. Phys. Chem. C* **116,** 14848–14856 (2012).
44. *Carbon Nanotubes*. **80,** (Springer Berlin Heidelberg, 2001).
45. Teichmann, P. *Adiabatic Logic*. **34,** (Springer Netherlands, 2012).
46. Song, W. *et al.* Synthesis of Bandgap-Controlled Semiconducting Single-Walled Carbon Nanotubes. *ACS Nano* **4,** 1012–1018 (2010).
47. Matsuda, Y., Tahir-Kheli, J. & Goddard, W. a. Definitive Band Gaps for Single-Wall Carbon Nanotubes. *J. Phys. Chem. Lett.* **1,** 2946–2950 (2010).
48. Krupke, R. Separation of Metallic from Semiconducting Single-Walled Carbon Nanotubes. *Science.* **301,** 344–347 (2003).
49. Bandaru, P. R. Electrical Properties and Applications of Carbon Nanotube Structures. *J. Nanosci. Nanotechnol.* **7,** 1239–1267 (2007).
50. Dionigi, C. *et al.* Control of neuronal cell adhesion on single-walled carbon nanotube 3D patterns. *J. Mater. Chem.* **20,** 2213–2218 (2010).
51. Mosconi, E., Quarti, C., Ivanovska, T., Ruani, G. & De Angelis, F. Structural and electronic properties of organo-halide lead perovskites: a combined IR-spectroscopy and ab initio molecular dynamics investigation. *Phys. Chem. Chem. Phys.* **16,** 16137 (2014).
52. Dionigi, C. *et al.* Carbon nanotube networks patterned from aqueous solutions of latex bead carriers. *J. Mater. Chem.* **17,** 3681 (2007).
53. Burke, A. *et al.* The Function of a TiO_2 Compact Layer in Dye-Sensitized Solar Cells Incorporating 'Planar' Organic Dyes. *Nano Lett.* **8,** 977–981 (2008).
54. Kongkanand, A. & Kamat, P. V. Electron Storage in Single Wall Carbon Nanotubes. Fermi Level Equilibration in Semiconductor–SWCNT Suspensions. *ACS Nano* **1,** 13–21 (2007).
55. Grätzel, M. *et al.* No Title. *Nature* **395,** 583–585 (1998).
56. Lee, M. M., Teuscher, J., Miyasaka, T., Murakami, T. N. & Snaith, H. J. Efficient Hybrid Solar Cells Based on Meso-Superstructured Organometal Halide Perovskites. *Science.* **338,** 643–647 (2012).
57. Kim, H. *et al.* Lead Iodide Perovskite Sensitized All-Solid-State Submicron Thin Film Mesoscopic Solar Cell with Efficiency Exceeding 9%. *Sci. Rep.* **2,** 1–7 (2012).
58. Milot, R. L., Eperon, G. E., Snaith, H. J., Johnston, M. B. & Herz, L. M. Temperature-Dependent Charge-Carrier Dynamics in $CH_3NH_3PbI_3$ Perovskite Thin

Films. *Adv. Funct. Mater.* **25,** 6218–6227 (2015).
59. Weisspfennig, C. T. *et al.* Optimizing the Energy Offset between Dye and Hole-Transporting Material in Solid-State Dye-Sensitized Solar Cells. *J. Phys. Chem. C* **117,** 19850–19858 (2013).
60. Leijtens, T., Lauber, B., Eperon, G. E., Stranks, S. D. & Snaith, H. J. The Importance of Perovskite Pore Filling in Organometal Mixed Halide Sensitized TiO_2 -Based Solar Cells. *J. Phys. Chem. Lett.* **5,** 1096–1102 (2014).
61. Bertoluzzi, L. *et al.* Cooperative kinetics of depolarization in $CH_3NH_3PbI_3$ perovskite solar cells. *Energy Environ. Sci.* **8,** 910–915 (2015).
62. Gottesman, R. *et al.* Extremely Slow Photoconductivity Response of $CH_3NH_3PbI_3$ Perovskites Suggesting Structural Changes under Working Conditions. *J. Phys. Chem. Lett.* **5,** 2662–2669 (2014).
63. Liu, C. *et al.* Hysteretic Behavior upon Light Soaking in Perovskite Solar Cells Prepared via Modified Vapor-Assisted Solution Process. *ACS Appl. Mater. Interfaces* **7,** 9066–9071 (2015).
64. Juarez-Perez, E. J. *et al.* Photoinduced Giant Dielectric Constant in Lead Halide Perovskite Solar Cells. *J. Phys. Chem. Lett.* **5,** 2390–2394 (2014).
65. Eames, C. *et al.* Ionic transport in hybrid lead iodide perovskite solar cells. *Nat. Commun.* **6,** 7497 (2015).

CHAPTER III:
PEROVSKITE SOLAR CELLS

1. Perovskite Active Layer Morphology Dependence on Solar Cell Architecture

The family of perovskite solar cells contains several highly efficient solar cell architectures or concepts which are generally driven by fundamentally different charge transport mechanisms.[1,2] A great deal of research has been focused on understanding the connection between the configuration of the solar cell with the morphology and structure of the perovskite material, with scaffold materials varying not only in their structural but in their dielectric/conductive properties as well.[3,4] In order to optimize each of the perovskite solar cell architectures there have been a variety of publications regarding the perovskite active layer deposition and formation conditions and mechanism, and the charge transfer dynamic with respect to the device structure.[5–7] It has been shown that the crystallization of the MAPI is strongly dependent on the mesoporous scaffold as well as the surface conditions (roughness, temperature, humidity) of the flat substrate. Since there are still unknowns regarding the charge transport in the MAPI, which will be discussed in the next chapter (from a certain viewpoint), significant data is also available on the identification of traps and defects in connection to the crystallinity, grain size and boundaries of the material.[8–11]

In an attempt to further research the MAPI formation and surface coverage with respect to the morphology of the underlying layer (mesoporous scaffold or flat compact layer) laser scanning confocal microscopy (LSCM) and laser beam induced photocurrent (LBIC) have been performed. Both mapping techniques have been employed as powerful tools for correlation of the optical images obtained with the LSCM and the electrical response from the LBIC. The study of the morphological properties confronted by the photophysics of the perovskite material, under illumination in cell configuration (charge generation and extraction), by beam induced scanning techniques is a novel approach in the field of perovskite solar cells. Very few publications report on similar approaches for Pl and current mapping,[12–15] not fully exploiting the potential of these techniques. The direct confrontation of the spatially resolved properties from both techniques (PL and I_{SC} intensity) provides connection between sub-micrometric morphological features of the active layer and the local photovoltaic response of the device. Moreover, this type of measurements can provide important information on the existence and influence not only of defects, but of specific degradation channels monitored under controlled ambient condition.

To obtain a full image of the active layer morphology confronted with the photocurrent generation, several types of cells were investigated:

- Planar solar cell configuration with two different types of TiO_2 compact layers (from now on referred as CL1 and CL2). Furthermore for the CL2, two types of solar cells were prepared with respect of the sintering temperature of the TiO_2 (low temperature 150°C and high temperature 450°C).
- TiO_2 mesoporous solar cell with CL1
- Al_2O_3 meso-superstructured solar cell with CL1.

1.1. Experimental - Device Preparation and Characterization

All chemicals except for the ones stated otherwise, were acquired from Aldrich, Fluka and used without further purification.

Device preparation. A detailed description of perovskite solar cell preparation employing a compact layer (CL1) and a TiO_2 mesoporous scaffold is presented in Chapter II, Section 3.1.2. All other PSC configurations were prepared following the same instruction for substrate cleaning and preparation. For the PSC employing CL2, the TiO_2 compact layer was deposited by spin coating 0.2 M of TiO_2 colloidal solution (see Chapter II, Section 2.2.1.) which was subsequently annealed at 150 or 450°C for 1 hour. For the solar cells employing alumina mesoporous scaffold, on top of the TiO_2 compact layer (CL1), aqueous solution of 235nm polystyrene beads and aluminium-sec-butoxide was drop-casted, which was subsequently burned at 450°C for 2 hours in air.[16] The Al_2O_3 scaffold was obtained after the annealing process during which the polystyrene beads were removed and the scaffold material was formed.

After the preparation of the photoanode, the cells were transferred in a controlled atmosphere, N_2 filled glove box with approximately 25% relative humidity and the perovskite and HCM were deposited by spin coating. In particular for all PSC architectures 40wt% (3:1 CH_3NH_3I to $PbCl_2$) DMF solution of Cl-doped MAPI (referred only as MAPI) was used. The MAPI was deposited on top of the compact or mesoporous films by spin-coating, and annealed on a hot plate at 95°C for 70 min. After perovskite formation spiro-OMeTAD (MERCK) was used as HCM with a concentration of 100 mg/ml solution in chlorobenzene, doped by TBP and LiTFSI (170 mg/ml solution in acetonitrile), 1:9 μl/mg TBP:spiro-OMeTAD; 1:2 μl/mg LiTFSI:spiro-OMeTAD). The samples were left to dry overnight in dark, in ambient air. 120 nm silver top contacts were deposited by thermal evaporation using a shadow mask to obtain 4 (0.16 cm^2) solar cells per substrate.

LSCM was performed with Nikon TE2000 optical microscope connected with a Nikon EZ-1 confocal scanning head. The laser excitation wavelength was 488 nm. The laser was focused inside the device at a depth corresponding to the active layer and the corresponding confocal photoluminescence signal was collected in reflection mode, through the same optical path of the excitation light. Different dichroic mirrors were used to collect the luminescence from different spectral regions. By scanning the samples over a defined area, a two-dimensional map of the photoluminescence intensity was created. All devices were measured in air without encapsulation after preparation. After LSCM, the LBIC were performed.

LBIC measurements were performed with the same experimental set-up, using a pulsed laser diode with 405 nm wavelength as light excitation source. At this wavelength the devices exhibit a light absorption sufficient to obtain a detectable photocurrent signal. The laser is focused on the sample through a 60x NA 0.70 air objective of the confocal microscope. The locally generated short-circuit photocurrent was acquired with a lock-in amplifier by modulating the excitation source between 5 and 15 kHz, while the device was kept in short circuit conditions. The PC maps were collected by scanning the laser beam onto the sample. The laser power was 15 μW, and the laser spot 0.7μm.

SEM images were obtained using a Zeiss FEG-SEM LEO 1530 electron microscope at 5.00 kV equipped with an energy dispersive X-ray spectrometer (EDX).

1.2. LSCM and LBIC Investigation

With the laser scanning confocal microscopy it is possible to study selectively the morphology of the active layer in working devices. Upon illumination with the excitation light, the excited states are generated in the photoactive material. The photoluminescence is consecutively generated by radiative recombination of the excited states by emission of photons with energies around the band gap of the solar cell absorber material. If there is an electron transfer and charge generation processes in the perovskite material, the photoluminescence will be mostly quenched, however it should still possible to collect the residual photoluminescence arising from unquenched photoexcited states, resulting in rather low PL intensity.[17,18] Since the LSCM is based on the absorption of the active material, it will essentially reflect only on the perovskite properties and not on processes involving the selective contacts. Thus, the obtained maps can be used for localization and qualitative as well as quantitative classification of local defects existing in the solar cell structure.[14] While a detailed description of the technique and the experimental conditions are presents in the Appendix and the experimental part of this section several important points need to be noted. Exciting the cell with longer wavelength sources would generally produce higher photocurrent; nevertheless, by using monochromatic light excitation with a shorter wavelength images with a higher resolution can be obtained. Furthermore the absorption and the external quantum efficiency of the MAPI are quite high at 405 nm.[3]

On the other hand the laser beam induced photocurrent (LBIC) allows investigation of the morphology the active layer through its charge generation, separation and transport efficiency. The local short circuit photocurrent arising from the photoexcited material is collected by the electrodes and a map of the photogenerated carrier collection as a function of the location of carrier generation is created.

Measurements of a planar perovskite solar cell with CL1 are presented in Figure 1. The two different LSCM images are obtained by using different filters for the photoluminescence collection. Namely, the first image is obtained by using a green channel (490-565nm), while the second is obtained by a red-IR channel (565-900nm). It has to be pointed out that the contrast of the PL maps is taken in arbitrary units to ensure better visualization of the features, thus the intensity of the signals cannot be directly correlated between the images, providing only a qualitative inspection. The PL intensity obtained with the green channel was practically negligible in intensity compared to the signal obtained with the red-IR channel and the brightness of the features is strongly enhanced with respect to the real emission. Since the 2D maps acquired with LSCM basically represent projection of the active layer morphology, the same distinctive features can be observed on both maps, though having opposite position of bright and dark spots. When comparing both PL maps in Figure 1 it is obvious that the photoluminescing species in the green appear to cover the entire surface area and the most intense signal is evident in the dark spots of the red-IR channel map. Intuitively it can be concluded that the dark spots in the map (Figure 1b) represent areas not covered by the perovskite, concluding that the signal in the map in Figure 1a is due to the weak broad PL band of the spiro-OMeTAD.

Upon further investigation it can be concluded that the perovskite coverage of the CL1 is rather good, however several pinholes of few microns are present. In Figure 1c a partial LBIC image is reported, note that the quality of the image is low since very few bright spots can be observed, due to the fact that the devices were investigated in ambient conditions (60-65% relative humidity), degradation of the cell due to humidity is most probable although light-induced degradation cannot be excluded. However, since the LBIC and LSCM are not completely observing the same objects, laser scanning microscopy being confocal is collecting the luminescence only from a limited area independently from

where the light propagation is, and on the other end the LIBC is collecting carriers photogenerated from all the sites where the light can be absorbed, more or less from the entire illuminated cone, thus the homogeneous signal could be due to the absorption from deeper layers.

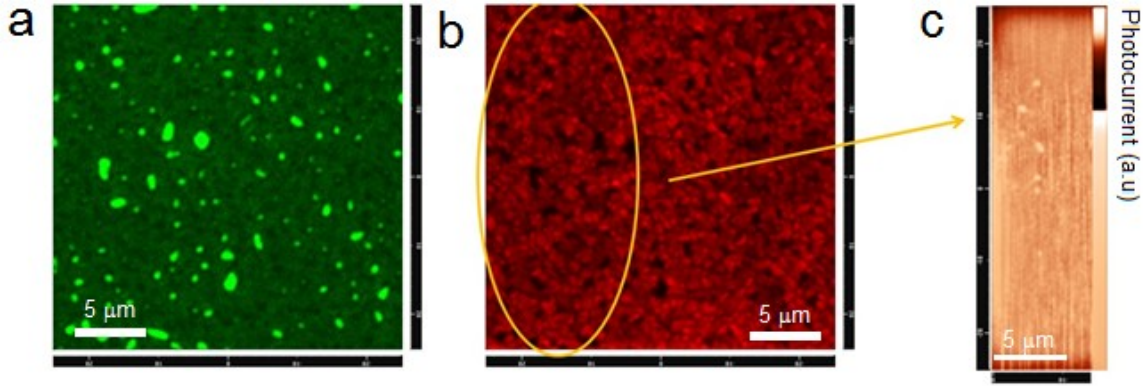

Figure 1. Investigation of planar PSC with CL1; a) PL map obtained with green channel (490-565nm); b) PL map obtained with red-IR channel (565-900nm); c) LBIC measurement of the designated cell area reported in b).

To obtain information on whether the differences in the compact layer can have impact on the crystallization of the MAPI and the surface coverage of the substrate, investigations were performed employing differently prepared compact layers CL2. Without changing the semiconducting material in order not to introduce new variables in the charge generation and transport investigation, the light beam techniques were used to study the morphology of solar cells prepared by annealing CL2 at both 150 and 450°C (Figure 2 and Figure 3).

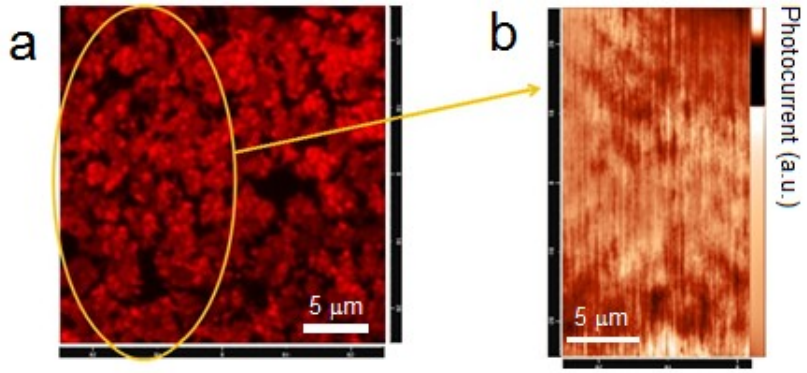

Figure 2. Investigation of planar PSC with CL2_150°C; a) PL map obtained with red-IR channel (565-900nm); b) LBIC measurement of the designated cell area reported in a).

Surprisingly, it can be observed that the crystallization of the perovskite material depends on the annealing temperature of the compact layer. Namely, the features in the two PL map images corresponding to a cell with CL2_150 and CL2_450 present quite a different morphology. Although the surface coverage was not significantly different, several distinctive features can be observed. In the low temperature processed cell (CL2_150) the perovskite had a cracked and disordered structure having almost a porous character (Figure 2a), whereas in the high temperature processed PSC (CL2_450) a more interconnected uniform structure was obtained. Additionally, in the CL2_450 (Figure 3a) the PL signal was more uniform in intensity indicating even charge generation and radiative recombination throughout the layer. By LBIC measurement (Figure 2b) information on the

efficient charge transport in the solar cell was observed. Although the contrast of the current map was not sufficiently clear, the dark and light areas are correlated to the same features of the PL map. The quality of the image could be connected to the roughness of the perovskite layer which might cause changes of the focus position throughout the scan. As evidenced from Figure 3b, the LBIC measurement provided an image with good quality (contrast and features corresponding to the PL map in Figure 3a), where bright features result from efficient charge transport and dark spots correspond to pinholes in the perovskite layer where probably non-radiative absorption is occurring, because of absence of MAPI. The relatively uniform intensity of the LBIC image supports the PL map in the interpretation of homogeneous charge generation throughout the MAPI.

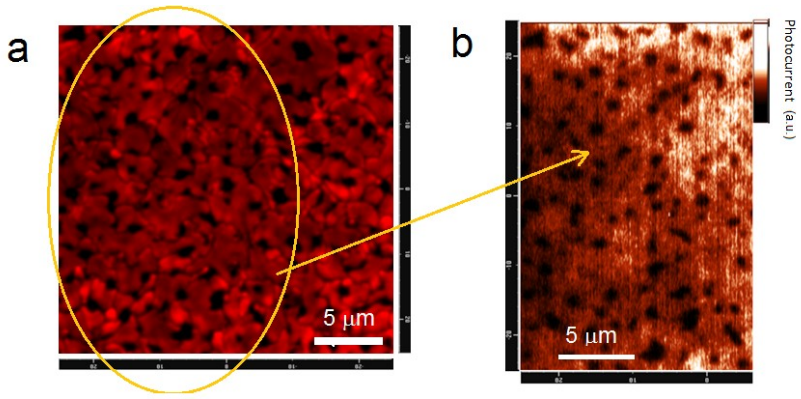

Figure 3. Investigation of planar PSC with CL2_450°C; a) PL map obtained with red-IR channel (565-900nm); b) LBIC measurement of the cell area reported in a).

The mesoporous PSC employing a TiO_2 photoanode was discussed with respect to photoanode optimization in the previous chapter. Further investigation into this type of PSC was conducted to investigate the difference of the perovskite layer morphology with respect to the planar PSC, since differences in crystallinity as well as crystalline size can have implication on the light absorption properties and in turn device efficiency.[4] In Figure 4a and b, PL maps of the same cell but in different positions are presented. It can be observed that the distinctive features of the perovskite layer are relatively smaller in comparison with the solar cells where the perovskite layer is in a planar configuration and not incorporated in a scaffold. It is obvious that the interconnection between the perovskite (bright spots) and the TiO_2 (dark spots) is quite good indicating a thin overlayer. An SEM image of the TiO_2 mesoporous scaffold is presented in Figure 4d to indicate the morphology of the underlayer. In Figure 4b a rather large dark spot is observed, this is a result of non-uniformity or a grain within the TiO_2 mesoporous layer where no perovskite is evident. The LIBC image similar to the one in Figure 1c does not reproduce the surface morphology of the perovskite very well. Considering that the intrinsic humidity of a mesoporous layer prepared in ambient conditions, even after annealing, could be quite relevant for the degradation of the perovskite layer. Additionally, the intense light of the LBIC (even though the light exposure time is 0.1ms/point) is probably increasing the degradation rate of the non-encapsulated device.

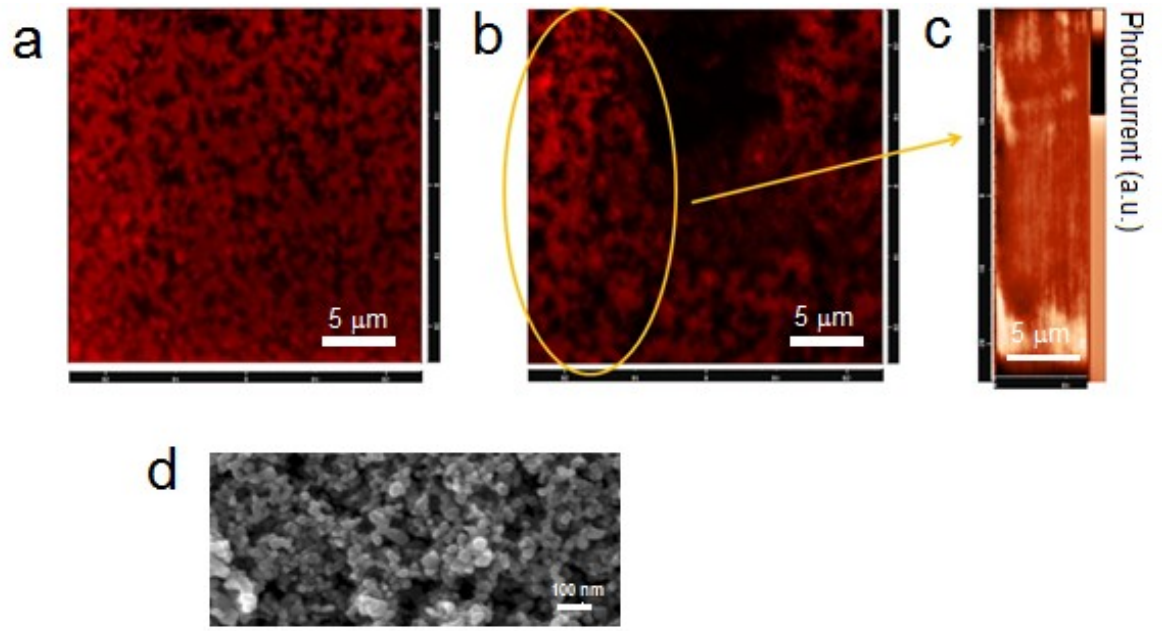

Figure 4. Investigation of mesoporous PSC with CL1; a) and b) PL map obtained with red-IR channel (565-900nm); c) LBIC measurement of the designated cell area reported in b); d) SEM image of the mesoporous TiO_2 scaffold.

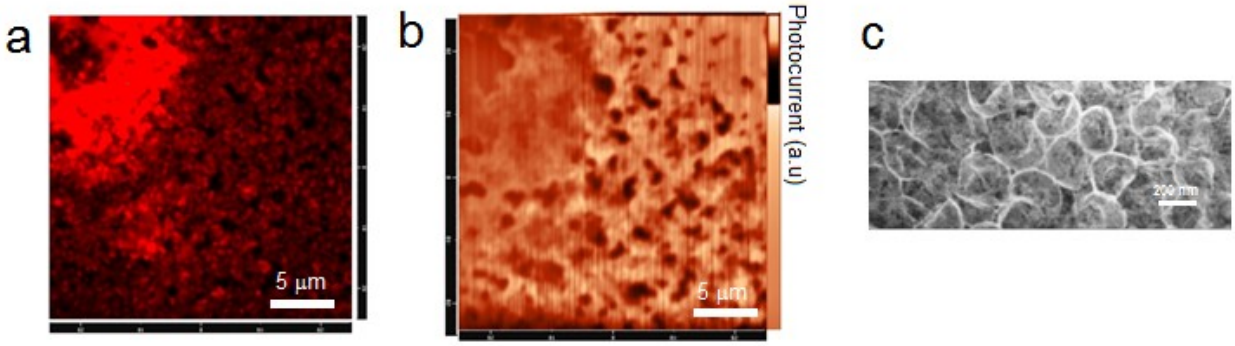

Figure 5. Investigation of meso-superstructured PSC with CL1; a) PL map obtained with red-IR channel (565-900nm); b) LBIC measurement of the cell area reported in a); c) SEM image of the Al_2O_3 scaffold.

Figure 5 reports on the PL and photocurrent map images of the meso-superstructured PSC. This investigation is of great importance especially in comparison to the previous solar cell configurations since the charge transport within the cell is quite different. As described in Chapter I Section 7, the photogenerated electron in the perovskite will not be injected into the Al_2O_3 scaffold but will rather be transported throughout the perovskite till the charge selective compact TiO_2 layer.

The PL map in image in Figure 5a presents the perovskite layer within the dielectric alumina scaffold (Figure 5c). The coverage and the small distinguishable features are similar as discussed previously. Due to the dynamics of perovskite crystallization certain dark spots are also observed presumably as a result of lack of material; however, a large spot of very high intensity PL emission is also evident. When compared to the LBIC image all features are reproduced with respect to bright and dark spots except the large feature of increased PL (top left in Figure 5a). Considering that the increased PL signal results from unquenched states where the photogenerated carriers are not injected into the electron or

hole transport layers, the majority of these carriers will recombine, most of them radiatively which by comparison, due to the inefficient charge transport, in this position will not be reproduced by the LBIC image as the brightest spot, as evidenced form Figure 5b. One of the reasons could be the lack of HCM, or an area of too compact insulation alumina. This indicates that certain local device functioning mechanisms such as increased charge-carrier recombination and local resistivity are affecting the current generation. In a solar cell configuration detecting defects of this type can provide important information of device functioning and optimization.

1.3. Conclusion

LSCM and LBIC are non-invasive techniques which allow visualization of the morphology of the active layer in complete working devices which helps us to correlate it with the photovoltaic parameters of the solar cell through the photocurrent map image and its distinctive features. The investigation of different device architectures was performed not only to observe the variation of the perovskite layer morphology and surface coverage, but to monitor the possible degradation of the devices under reported measurement conditions.

The devices employing a mesoporous scaffold are more prone to defects due to the un-uniformity that arises from the deposition of the mesoporous film, single step solution deposition of MAPI and insufficient pore filling of the perovskite. The lack of photoactive material at certain points or high recombination due to possible pinholes inevitably diminishes the efficiency of the device reducing the *FF* and V_{OC}. Furthermore it was observed that the uniformity and the crystallinity of the perovskite growth are greatly influenced by the morphology of the compact layer. The air exposure of non encapsulated cells during measurement show possible route towards degradation through residual humidity in the mesoporous material and possibly the compact layer, although the impact of the light intensity in combination with atmospheric conditions cannot be excluded.

2. Low and High Temperature Processed Planar Perovskite Solar Cell

In developing and optimizing any new solar cell technology apart from the improvement in efficiency, the stability and the cost-effectiveness of the device have to be taken into account. The LSCM and LBIC discussed in the previous section revealed that the planar PSC prepared by employing compact layer annealed at low and high temperature, even though the morphology and the surface coverage of the perovskite layer exhibits differences, could have better reproducibility, stability and slower degradation rate with respect to preparation and exposure to atmospheric conditions, than the mesoporous PSC. Additionally, investigating and evaluating the photovoltaic parameters of a low temperature (150°C) and high temperature (450°C) processed PSC with respect to certain aging conditions can in turn provide information on whether the PSC with reduced construction energy consumption can sufficiently measure up to its high temperature opponent with respect to efficiency and stability.

There are only few reports in literature on low temperature processed perovskite solar cell, employing a solution processed TiO_2 compact layer,[19,20] however a direct confrontation of the possible differences, advantages or disadvantages due to the low temperature TiO_2

annealing have not been directly reported or postulated. The differences between the low and high temperature processing of the compact layer can be disused from the point of view of charge transport properties and electronic structure of the compact layer, since the higher temperature annealing is promoting better sintering, and in turn, better connection between the nanoparticles which was discussed in the previous chapter. However, as evidenced from the precious section, when discussing MAPI the processing temperature of the compact TiO_2 layer affects at least another parameter, the morphology of the perovskite. Considering this, further investigation was conducted in order to achieve high efficiency solution processed planar PSC employing standard materials (FTO/TiO_2/MAPI/spiro-OMeTAD/Ag) and low-cost techniques such as spin-coating. Furthermore, differences in the PSC photovoltaic parameters are addressed not only regarding the annealing temperature of the TiO_2 compact layer, but studies are focused on the perovskite material with respect to crystallization, doping and degradation, as well.

2.1. Experimental

All chemicals except for the ones stated otherwise, were acquired from Aldrich, Fluka and used without further purification.

2.1.1. Device Preparation

Substrate preparation (cleaning and etching) was performed as described in Chapter II Section 3.1.2. The low and high temperature processed compact TiO_2 layers were prepared by spin coating 0.2 M of TiO_2 nanoparticle colloidal solution (Chapter II Section 2.2.1.) which was subsequently annealed at 150 or 450°C for 1 hour. After the preparation of the photoanode, the samples were transferred in a controlled atmosphere, N_2 filled glove box with approximately 20±3% relative humidity and 40wt% (3:1 CH_3NH_3I to $PbCl_2$) DMF solution of Cl-doped MAPI (referred only as MAPI) was deposited by spin coating employing solvent engineering during the last 10s of the spin cycle by drop casting Toluene,[21] after which the samples were annealed on a hot plate at 95°C for 70 min. Spiro-OMeTAD (MERCK) was used as HCM with a concentration of 100 mg/ml solution in chlorobenzene, doped by TBP and LiTFSI (170 mg/ml solution in acetonitrile), 1:9 µl/mg TBP:spiro-OMeTAD; 1:2 µl/mg LiTFSI:spiro-OMeTAD). Where stated, a highly doped 72.3 mg/ml of spiro-OMeTAD in chlorobenzene solution was used (1:2.6 µl/mg TBP:spiro-OMeTAD; 1:4.25 µl/mg LiTFSI (520 mg/ml solution in acetonitrile):spiro-OMeTAD. The samples were left to dry overnight in dark, in dry box with O_2. 120 nm silver top contacts were deposited by thermal evaporation using a shadow mask to obtain 4 (0.16 cm^2) solar cells per substrate.

2.1.2. Device Characterization

Current voltage measurements of the cells were performed with Keithley 236 source-measure unit with a point delay of 300 ms both in forward and backward scanning direction under simulated AM1.5 illumination of 100 mW/cm^2 from Abet Technologies Sun 2000 Solar Simulator. During measurement the cells were masked with a sample holder of a cell size aperture. The cells were tested inside a glove box in oxygen and moisture free environment.

LSCM was performed with Nikon TE2000 optical microscope connected with a Nikon EZ-1 confocal scanning head. The laser excitation wavelength was 488 nm. The laser was focused inside the device at a depth corresponding to the active layer and the corresponding confocal photoluminescence signal was collected in reflection mode, through the same optical path of the excitation light.

2.2. Effect of O_2 Exposure on Solar Cell Parameters

The optimization of the preparation procedure for the planar perovskite solar cell has been vastly reported throughout the literature in the last 3 years. From the thickness of the TiO_2 compact layer, to the thickness and annealing conditions of the MAPI, to the thickness and doping of the HCM,[22–25] especially for the vastly used spiro-OMeTAD (since highest PSC efficiencies have been reported with this p-semiconductor, regardless of the PSC configuration). Nevertheless, one of the main points in the optimization procedure is the fine adjustment of the preparation procedure and atmospheric conditions when it comes to the MAPI. Namely, the high sensitivity on this perovskite on humidity, oxygen and temperature has hindered researchers to come to a consensus on the positive (efficiency improvement) vs. negative (degradation) effects of certain atmospheric elements.[26–30]

The low and high temperature processed planar perovskite solar cells were prepared as described in the experimental section following a generally accepted procedure.[22] The spin-coating speed and time, the annealing temperature and the different exposure steps (atmospheric) were established in the laboratory after a period of optimization.

After the photovoltaic investigation (*I-V* measurement under 1 sun) most of the as prepared devices (immediately after the top contact deposition) experienced low efficiency. Both the low and the high temperature processed devices (denoted as CL_150 and CL_450) were exhibiting low V_{OC} and *FF*, while the J_{SC} was generally good. The inspection of the shape of the *I-V* plots and the photovoltaic parameters indicated significant contribution of unfavorable resistance which could be the predominant reason for the low efficiency. *I-V* plots of representative CL_150 and CL_450 solar cells are reported in Figure 6.

Confronting the data published in literature one of the issues of the working mechanism could be the insufficient doping of the spiro-OMeTAD.[31] During the preparation procedure, the solar cells were left overnight in a dry box with O_2 to ensure the doping of the HCM. This step was replaced with doping in air since it is essentially oxygen which is influencing the doping of the spiro-OMeTAD[32] and furthermore the humidity from the ambient air could degrade the perovskite layer by infiltrating within the cell. Nevertheless, to understand if further oxygen exposure could have any effect on the photovoltaic parameters, the PSC were left for another 16-20 hour (overnight in dark) in dry oxygen prior to remeasuring their *I-V* response. A schematic diagram of the ambient conditions of the solar cells preparation and characterization is presented in Figure 7.

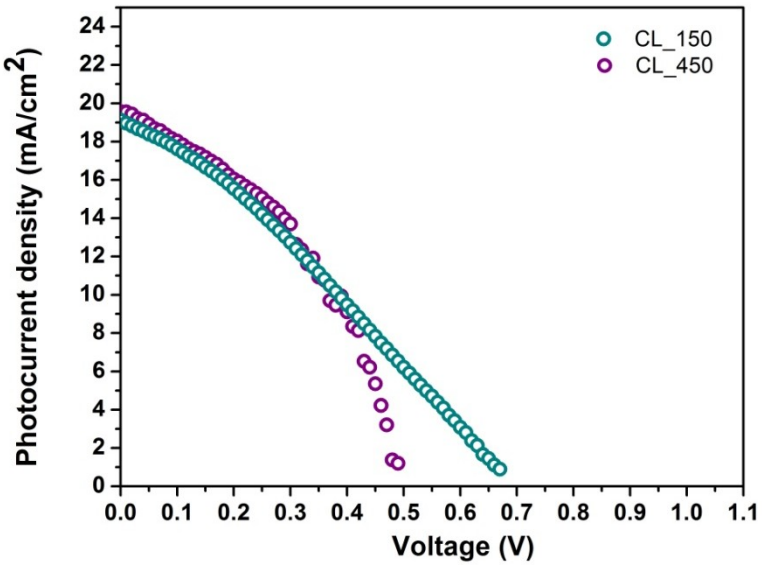

Figure 6. Current-voltage plots of as prepared (after top contact deposition) CL_150 and CL_450 PSC.

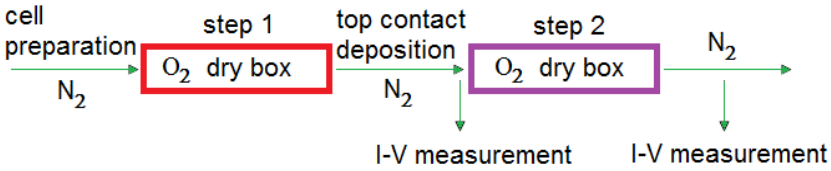

Figure 7. Schematic presentation of successive steps in PSC atmospheric exposure and measurement conditions.

After the second step oxygen exposure the *I-V* response of the cells was remeasured; significant increase of efficiency was observed. All photovoltaic parameters increased, however the increase of V_{OC} and *FF* was quite high (Figure 8). In order to confirm the observed effect, to understand the reproducibility of the efficiency improvement mechanism and to establish a quantitative analysis regarding the difference of the PSC parameters several batches of cells were prepared and investigated. The results are reported in Figure 9.

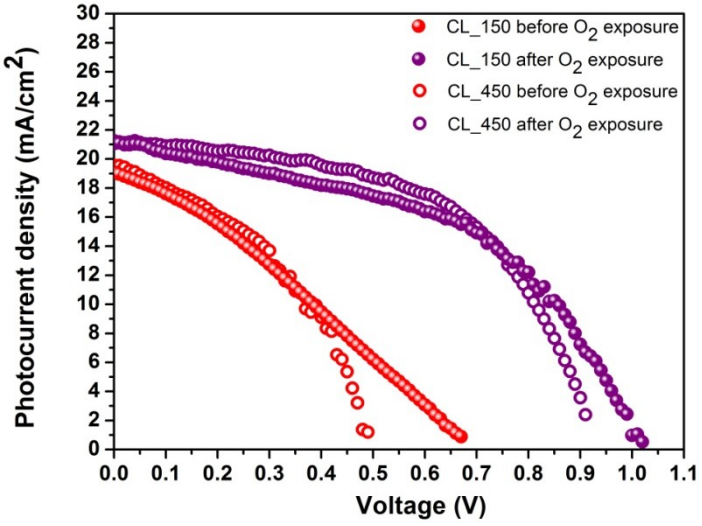

Figure 8. Current-voltage plots of as prepared CL_150 and CL_450 PSC and second step O_2 exposed devices. Both measurements are performed on the same representative cell

As evident from the statistics in Figure 9, the as prepared CL_150 PSC had generally lower reproducibility of the J_{SC} and V_{OC}. Although the mean value of the J_{SC} for the CL_450 was around 40% higher, the V_{OC} mean value between the low and high temperature processed cells was almost the same, although some CL_150 devices exhibited high V_{OC} up to 1.1V. The fill factor of all devices was quite low, especially for CL_150 around 30%, whereas for the CL_450 a widespread of values is observed, though statistically the CL_450 devices had a better fill factor. Since the efficiency of both types of devices was generally low probably due to obstructed charge transport mechanisms, a valid interpretation of the photovoltaic parameters and differences between the low and the high processed device is difficult. On the other hand after the second step O_2 exposure for both types of devices a smaller discrepancy in the photovoltaic parameters was observed within the respective group, especially evident for the J_{SC}. Regarding the optimized devices (after step 2 O_2 exposure), both the J_{SC} and the V_{OC} show similar mean values, while the difference in efficiency is mimicking the difference in the fill factor between the low and the high temperature processed device.

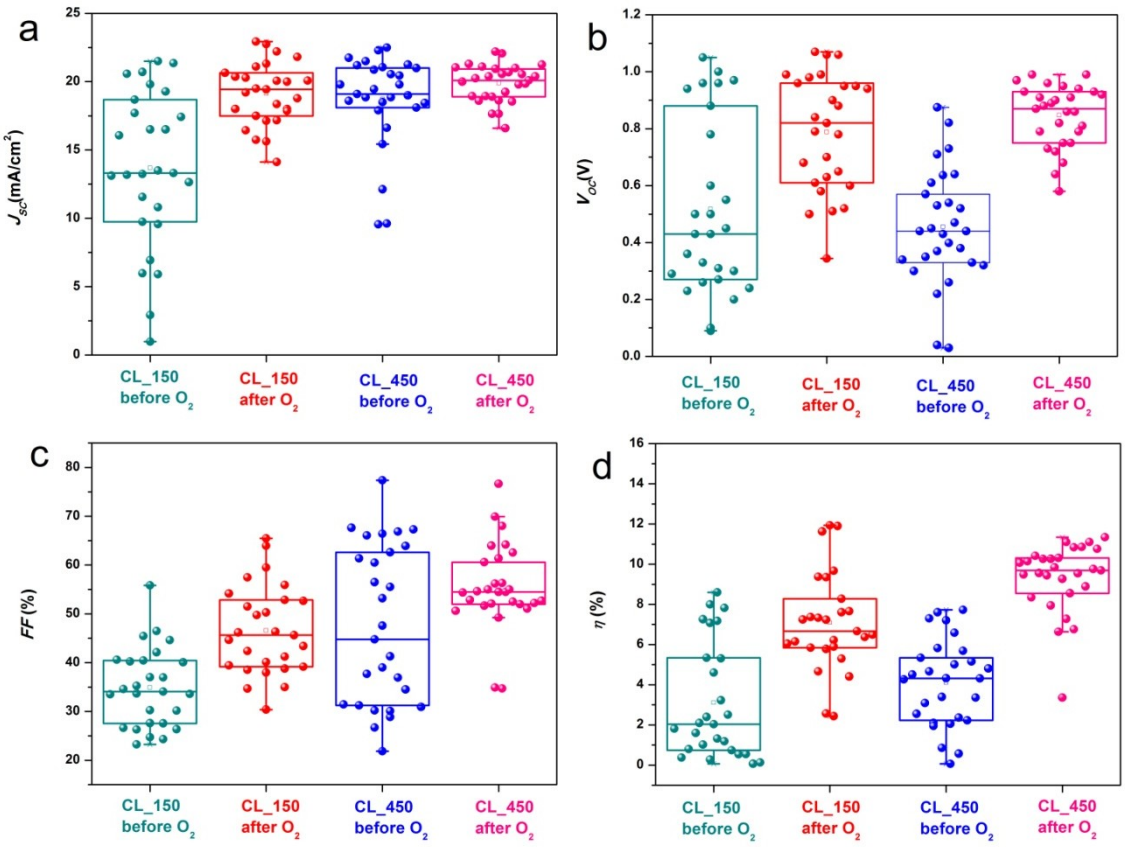

Figure 9. Box plots of solar cell parameters for CL_150 and CL_450 PSC before second step O_2 exposure (as prepared) and after O_2 exposure; a) J_{SC}; b) V_{OC}; c) FF; d) η.

The differences in the photovoltaic parameters of the PSC with respect to the processing temperature, depend not only on the difference of the electronic properties of the TiO_2 but also on the properties of the MAPI. From the LSCM images reported in the previous section it was evident that the morphology of the MAPI was different with respect to the annealing temperature of the TiO_2 layer. One of the reasons could be intrinsic residual humidity in the low temperature processed compact layer which could in turn change the thermodynamic landscape during the crystallization of the perovskite. Regarding the optimized device efficiency (after the second step O_2 exposure) the CL_150 PSC are able

to compete with the high energy processed CL_450. Granted the reproducibility of the CL_450 is higher, however optimization of the deposition method for the compact layer could be achieved to further support this claim. Annealing an aqueous colloidal suspension of TiO_2 nanoparticles at 150°C is sufficient to remove the suspending medium; however certain residual impurities such as hydrated compounds can remain present. This can affect the wettability of the perovskite solution on one side and the crystallization on the other.

It should be noted that in all the current-voltage characterization of the PSC, both before and after the second step O_2 exposure, a hysteresis of the *I-V* response was observed. Considering this observation, all the data presented in this chapter correspond to the forward scanning direction regarding the *I-V* measurement of the PSC. Since the nature of the hysteresis behavior is still under debate in the scientific community, the presentation of the backward scan is omitted in order not to overestimate the PSC efficiency. In Figure 10, the *I-V* response recorded in forward and backward scan direction of a representative cell from Figure 9 (CL_450) is reported.

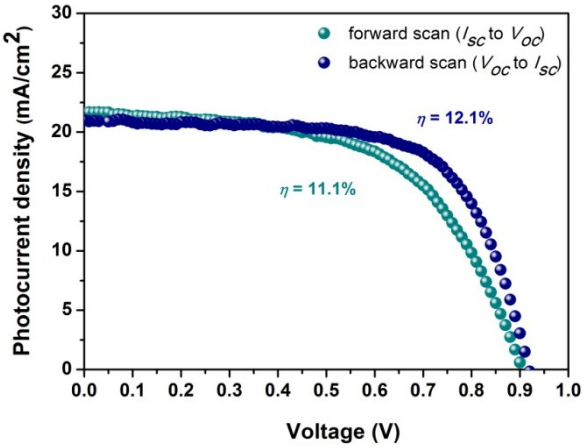

Figure 10. Hysteresis behavior of the *I-V* response of the PSC with respect to the scan direction.

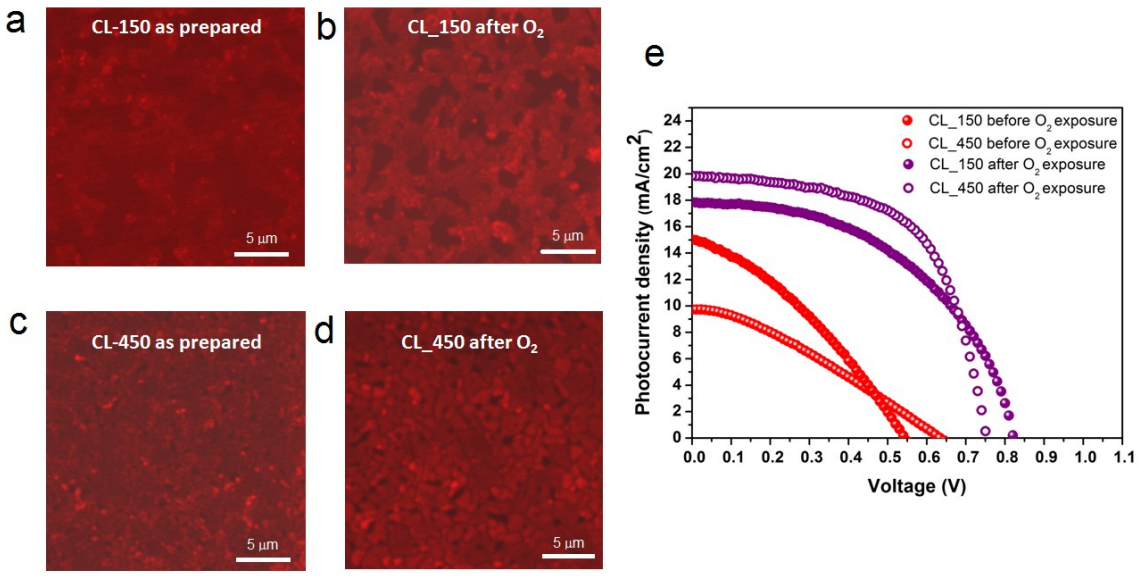

Figure 11. CL_150 and CL_450 perovskite solar cells; a) LSCM image of MAPI of as prepared CL_150 device before O_2 exposure; b) LSCM image of MAPI of CL_150 device after O_2 exposure; c) LSCM image of MAPI of as prepared CL_450 device before O_2 exposure; d) LSCM image of MAPI of CL_450 device after O_2 exposure; e) *I-V* plots before (as prepared) and after O_2 exposure.

In Figure 11a-d LSCM images of MAPI layer from the CL_150 and CL_450 PSC are reported. The representative *I-V* curves of these devices are reported in Figure 11e. Indeed as evidenced, the surface coverage of the CL_150 is smaller than CL_450, thus any difference in the solar cell efficiency could be attributed to this.

The interface between the TiO_2 and the HCM could introduce increased recombination mechanisms which in turn can lower the *FF*. Even though further investigation is needed to clearly distinguish whether the conductivity of the low temperature processed TiO_2 has any contribution to the lower value of the CL_150 PSC efficiency, the negligible difference between the J_{SC} and V_{OC} with respect to the CL_450 PSC indicate that the contribution to the charge transport of the possibly lower conductivity of the CL_150 is rather small, if any.

The investigation reported in Figure 11 was performed using twin devices by acquiring the PL map on an as prepared encapsulated device, and subsequently the twin PSC was O_2 aged and encapsulated before measurement in order to eliminate any MAPI degradation during the transfer and measurement.

Upon inspection of the PL maps it is evident that the morphology of the CL_150 and CL_450 is relatively different and the surface coverage of the CL_150 is smaller CL_450 as already discussed. However, what can be noticed about the PL intensity of both as prepared devices is that it's quite low. Note that the contrast of the images was adjusted for better visualization and the direct comparison of the color intensity/PL intensity between the images/samples is not adequate. However, it can be observed that the difference in the intensity between the dark spots (no MAPI) and bright spots (MAPI) of the as prepared devices (Figure 11 a and c) is quite small especially for the CL_150 where practically no features of the MAPI can be distinguished. It is doubtful that this large PL quenching is due to highly efficient charge diffusion towards the electron/hole selective buffer layers, but rather due to trapping defects which are causing non-radiative charge recombination.

There have been numerous reposts in literature on the instability of the MAPI with respect to humidity and oxygen exposure. At a certain point during the development and optimization of this new and young type of solar cell technology a general consensus was established on the negative aspects of the atmospheric conditions on material and device durability by material degradation and PbI_2 formation by exposure to H_2O. However, in the past year an increasing number of publications deal with the observation of positive effects of oxygen on both MAPI standalone films and devices. Furthermore, while it's accepted that high humidity atmosphere is degrading the MAPI, reposts surfaced on the positive impact of moisture (low relative humidity) on the PSC efficiency during annealing of the MAPI, as well as, in post-treatment conditions.[26,28,33]

The initial investigation was focused on the differences of the photovoltaic parameters of the low and high temperature processed solar cells, however in parallel the effect of the prolonged oxygen exposure was studied both regarding the underlining cause and the difference with respect to the type of solar cell (CL_150 and CL_450). The initial step was to confirm that the O_2 exposure was in fact responsible for the change in photovoltaic parameters, and not some other delayed structural or chemical mechanism not related to the oxygen exposure at all. After the preparation and the measurement of the solar cells, instead of second step O_2 exposure (Figure 7), half of a batch of PSC were left in the glove box overnight. After remeasuring the *I-V* response, no improvement was observed, as oppose to the other half which was submitted to O_2 exposure. Additionally, a batch of solar cells was prepared to investigate whether the increased efficiency of the solar cells was connected to the increase of the conductivity of the spiro-OMeTAD. CL_150 solar cells were prepared using a more chemically doped HCM (see Section 2.1.1) which were

additionally, according to device preparation procedure, submitted to the first step O_2 exposure prior to top contact deposition. Surprisingly, no difference in solar cell parameters was observed due to the increased doping, as a second step these devices were again exposed to O_2 after which mainly the increase in V_{OC} and FF was observed which resulted in increased efficiency. Considering that the increased doping level of the HCM did not show significant contribution the efficiency improvement both before and after the second step oxygen exposure, the effect of reduced series resistance and increased shunt should be a result either of TiO_2, or MAPI modification. It is known that reducing oxygen vacancies in the TiO_2 can have positive influence on electron transport, and oxygen exposure can, in a sense, passivate these vacancies, however, since the compact layers have been prepared in air, and furthermore the oxygen is affecting both CL_150 and CL_450 in same manner, most likely the transport mechanism modification due to O_2 is connected to the MAPI. Considering the above, this step of oxygen exposure efficiency improvement could be regarded as a curing step in the solar cell preparation.

This phenomenon of oxygen related species which under light exposure (during *I-V* measurement in this case) are deactivating trapping defects within the MAPI has already been observed and proposed by several groups.[34–36] Furthermore, the passivation effect of the oxygen on the MAPI grain boundaries has recently been reported with regard to reducing shallow traps.[37] Namely, it is proposed that the O passivation is modifying the grain boundaries of the MAPI at the interface with the spiro-OMeTAD, to a more p-type material, which in turn is facilitating the hole transport at this interface. Since grain boundaries are observed to be associated with PL quenching,[38] the O passivation can indeed yield positive effect by reducing non-radiative recombination as well. These results explain the large increase of the V_{OC} and the increase of the FF that have been observed during the solar cell investigation presented in this chapter.

Regarding the effect of the O_2 exposure on the efficiency of both CL_150 and CL_450 planar PSC further investigation is currently underway. The results generally indicate that in the presence of defects within the MAPI and poor photovoltaic response a simple and effective curing effect can be accomplished. Although these hypothesis need to be confirmed, the clear connection between O_2 positive impact on planar PSC efficiency is evident.

2.3. Planar Perovskite Solar Cell Degradation

A strait forward investigation on the degradation of low and high temperature processed planar PSC was performed by using LSCM. The measurements were performed in order to understand whether the residual intrinsic humidity of the CL_150 PSC could present a disadvantage, of an additional degradation channel in the solar cell. A schematic diagram of the preparation and measurement of the cells is presented in Figure 12.

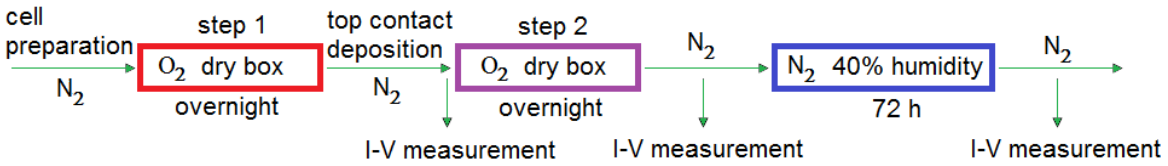

Figure 12. Schematic presentation of successive steps in PSC atmospheric exposure and measurement conditions.

LSCM images were recorded to understand if any distinct difference in the MAPI morphology or PL intensity can be observed after 72 hours in an N_2 environment with 40% relative humidity and ambient light. In Figure 13, PL maps and *I-V* plots of non-aged and aged encapsulated twin devices are reported. The investigation was performed by measuring encapsulated devices after oxygen curing and then twin devices (identical to the PSC reported in Figure 11) were exposed to the aging process and encapsulated prior to measurement. This sequence of events was employed to avoid additional atmospheric contribution to degradation during transport and measurement.

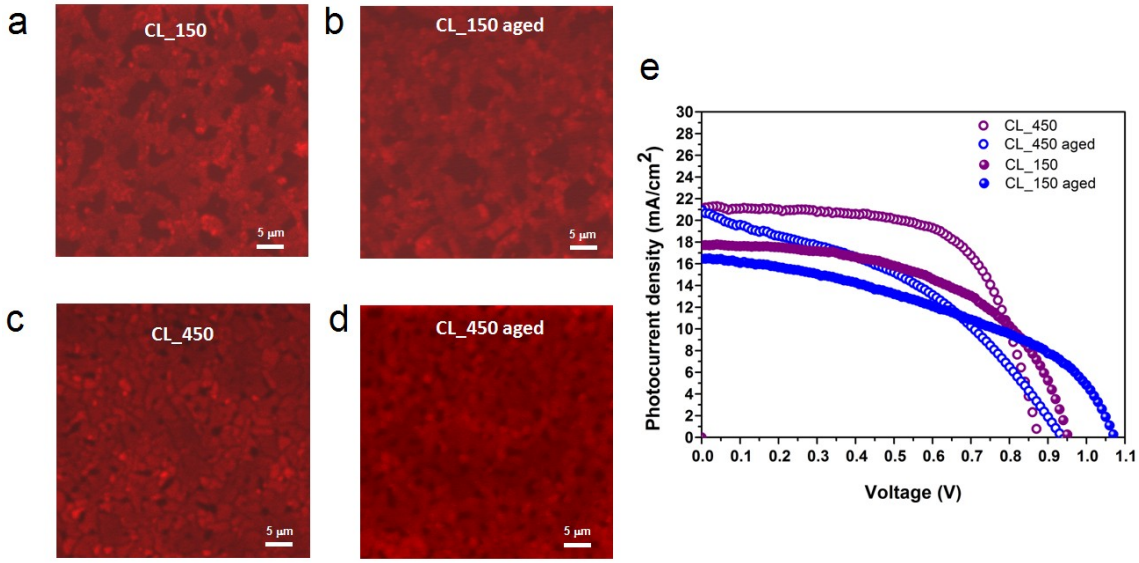

Figure 13. CL_150 and CL_450 perovskite solar cells; a) LSCM images of MAPI of O_2 cured devices; b) LSCM images of MAPI after aging procedure; c) *I-V* plots before and after aging.

The LSCM images show no significant change if morphology or PL intensity with respect to the distinctive features or grain boundaries. Even though these are initial degradation studies which need to be expended to longer aging time, different atmospheric conditions and larger device number, it is surprisingly encouraging to encounter that the low temperature processed device did not suffer from faster degradation. The efficiency of the investigated solar cell devices suffered a decline mainly as a result of a decrease in the *FF*. The degradation percentage was similar for both low and high temperature prepared devices indicating that the residual humidity in the compact layer does not significantly affect the perovskite material.

2.4. Conclusion

Preparation and characterization of low and high temperature processed planar perovskite solar cell was performed to understand whether the low annealing temperature (150°C) of the TiO_2 compact layer will grant comparable photovoltaic parameters, efficiency and stability with respect to the standard 450°C processed device. Oxygen exposure of the prepared devices increased the efficiency of all devices, for certain devices more than double, with the best performing cells having efficiency of more than 10%. This important O_2 post-treatment effect has been observed by other groups in different steps and aspects of the perovskite or PSC preparation and investigation, and could in turn play important role in MAPI defect curing of underperforming devices. Although further investigation in optimization of the deposition and crystallization of the MAPI could prove to decrease the trap density in the material, the O_2 curing can represent a "go to" mechanism in compensating differences in perovskite solar cell preparation conditions. Furthermore, it was established that even though the low temperature processed solar cells exhibited somewhat lower power conversion efficiency, due to most likely lower surface coverage of the MAPI of the TiO_2 compact layer, it can essentially compete with its high temperature counterpart.

Initial investigation of the degradation mechanism of both types planar PSC (CL_150 and CL_450) showed no increased number of degradation pathways due to the low processing temperature of the compact layer, thus optimizing the deposition kinetics or method of the MAPI for the CL_150 PSC could increase the surface coverage and increase the efficiency leveling the performance of the low and high processed device. The equality of photovoltaic parameters of planar perovskite solar cells processed at low and high temperatures, can single out the CL_150 PSC as not only the more cost-efficient device but more importantly extend the application of the PSC on different flexible substrates.

3. Bibliography

1. Yang, Z. & Zhang, W.-H. Organolead halide perovskite: A rising player in high-efficiency solar cells. *Chinese J. Catal.* **35,** 983–988 (2014).
2. Park, N.-G. Perovskite solar cells: an emerging photovoltaic technology. *Mater. Today* **18,** 65–72 (2015).
3. Lee, M. M., Teuscher, J., Miyasaka, T., Murakami, T. N. & Snaith, H. J. Efficient Hybrid Solar Cells Based on Meso-Superstructured Organometal Halide Perovskites. *Science.* **338,** 643–647 (2012).
4. D'Innocenzo, V. *et al.* Excitons versus free charges in organo-lead tri-halide perovskites. *Nat. Commun.* **5,** 3586 (2014).
5. Hsiao, Y.-C. *et al.* Fundamental physics behind high-efficiency organo-metal halide perovskite solar cells. *J. Mater. Chem. A* **3,** 15372–15385 (2015).
6. Ahn, N., Kang, S. M., Lee, J.-W., Choi, M. & Park, N.-G. Thermodynamic regulation of $CH_3NH_3PbI_3$ crystal growth and its effect on photovoltaic performance of perovskite solar cells. *J. Mater. Chem. A* **3,** 19901–19906 (2015).
7. Eperon, G. E., Burlakov, V. M., Docampo, P., Goriely, A. & Snaith, H. J. Morphological Control for High Performance, Solution-Processed Planar Heterojunction Perovskite Solar Cells. *Adv. Funct. Mater.* **24,** 151–157 (2014).
8. Yin, W.-J., Shi, T. & Yan, Y. Unusual defect physics in $CH_3NH_3PbI_3$ perovskite solar cell absorber. *Appl. Phys. Lett.* **104,** 063903 (2014).
9. Wu, X. *et al.* Trap States in Lead Iodide Perovskites. *J. Am. Chem. Soc.* **137,** 2089–2096 (2015).
10. Duan, H.-S. *et al.* The identification and characterization of defect states in hybrid organic–inorganic perovskite photovoltaics. *Phys. Chem. Chem. Phys.* **17,** 112–116 (2015).
11. Kim, J., Lee, S.-H., Lee, J. H. & Hong, K.-H. The Role of Intrinsic Defects in Methylammonium Lead Iodide Perovskite. *J. Phys. Chem. Lett.* **5,** 1312–1317 (2014).
12. Matteocci, F. *et al.* High efficiency photovoltaic module based on mesoscopic organometal halide perovskite. *Prog. Photovoltaics Res. Appl.* **19,** n/a–n/a (2014).
13. Razza, S. *et al.* Perovskite solar cells and large area modules (100 cm2) based on an air flow-assisted PbI2 blade coating deposition process. *J. Power Sources* **277,** 286–291 (2015).
14. Mastroianni, S. *et al.* Analysing the effect of crystal size and structure in highly efficient $CH_3NH_3PbI_3$ perovskite solar cells by spatially resolved photo- and electroluminescence imaging. *Nanoscale* **7,** 19653–19662 (2015).
15. Song, Z. *et al.* Investigation of degradation mechanisms of perovskite-based photovoltaic devices using laser beam induced current mapping. in (eds. Eldada, L. A. & Heben, M. J.) **9561,** 956107 (2015).
16. Dionigi, C. *et al.* Fabrication and properties of non-isolating γ-alumina meso-foam. *J. Alloys Compd.* (2016). doi:10.1016/j.jallcom.2016.01.075
17. Tessarolo, M. *et al.* Predicting thermal stability of organic solar cells through an easy and fast capacitance measurement. *Sol. Energy Mater. Sol. Cells* **141,** 240–247 (2015).
18. Seeland, M., Rösch, R. & Hoppe, H. in *Stability and Degradation of Organic and Polymer Solar Cells* 39–70 (John Wiley & Sons, Ltd, 2012). doi:10.1002/9781119942436.ch3
19. Vaenas, N., Konios, D., Stergiopoulos, T. & Kymakis, E. Slow photocharging and reduced hysteresis in low-temperature processed planar perovskite solar cells. *RSC Adv.* **5,** 107771–107776 (2015).

20. Conings, B. *et al.* An easy-to-fabricate low-temperature TiO2 electron collection layer for high efficiency planar heterojunction perovskite solar cells. *APL Mater.* **2,** 081505 (2014).
21. Jeon, N. J. *et al.* Solvent engineering for high-performance inorganic-organic hybrid perovskite solar cells. *Nat. Mater.* **13,** 1–7 (2014).
22. Eperon, G. E., Burlakov, V. M., Docampo, P., Goriely, A. & Snaith, H. J. Morphological Control for High Performance , Solution- Processed Planar Heterojunction Perovskite Solar Cells. 1–7 (2013). doi:10.1002/adfm.201302090
23. Saliba, M. *et al.* Influence of thermal processing protocol upon the crystallization and photovoltaic performance of organic-inorganic lead trihalide perovskites. *J. Phys. Chem. C* **118,** 17171–17177 (2014).
24. Leijtens, T., Lauber, B., Eperon, G. E., Stranks, S. D. & Snaith, H. J. The Importance of Perovskite Pore Filling in Organometal Mixed Halide Sensitized TiO 2 -Based Solar Cells. *J. Phys. Chem. Lett.* **5,** 1096–1102 (2014).
25. Dualeh, A. *et al.* Impedance spectroscopic analysis of lead iodide perovskite-sensitized solid-state solar cells. *ACS Nano* **8,** 362–373 (2014).
26. Pathak, S. *et al.* Atmospheric In fl uence upon Crystallization and Electronic Disorder and Its Impact on the Photophysical Properties of Organic À Inorganic Perovskite Solar Cells. *ACS Nano* (2015).
27. Solar, P. *et al.* Vacuum-Assisted Thermal Annealing of $CH_3NH_3PbI_3$ for Highly Stable and. 639–646 (2015).
28. Eperon, G. E. *et al.* The Importance of Moisture in Hybrid Lead Halide Perovskite Thin Film Fabrication. *ACS Nano* 9380–9393 (2015). doi:10.1021/acsnano.5b03626
29. Sheikh, A. D. *et al.* Atmospheric effects on the photovoltaic performance of hybrid perovskite solar cells. *Sol. Energy Mater. Sol. Cells* **137,** 6–14 (2015).
30. Yang, J., Siempelkamp, B. D., Liu, D. & Kelly, T. L. Investigation of $CH_3NH_3PbI_3$ Degradation Rates and Mechanisms in Controlled Humidity Environments Using in Situ Techniques. *ACS Nano* **9,** 1955–1963 (2015).
31. Abate, A. *et al.* Lithium salts as 'redox active' p-type dopants for organic semiconductors and their impact in solid-state dye-sensitized solar cells. *Phys. Chem. Chem. Phys.* **15,** 2572 (2013).
32. Hawash, Z., Ono, L. K., Raga, S. R., Lee, M. V. & Qi, Y. Air-Exposure Induced Dopant Redistribution and Energy Level Shifts in Spin-Coated Spiro-MeOTAD Films. *Chem. Mater.* **27,** 562–569 (2015).
33. Ng, A. *et al.* Efficiency enhancement by defect engineering in perovskite photovoltaic cells prepared using evaporated PbI_2/CH_3NH_3I multilayers. *J. Mater. Chem. A* **3,** 9223–9231 (2015).
34. Galisteo-López, J. F., Anaya, M., Calvo, M. E. & Míguez, H. Environmental Effects on the Photophysics of Organic–Inorganic Halide Perovskites. *J. Phys. Chem. Lett.* **6,** 2200–2205 (2015).
35. Tian, Y. *et al.* Mechanistic insights into perovskite photoluminescence enhancement: light curing with oxygen can boost yield thousandfold. *Phys. Chem. Chem. Phys.* DOI:10.1039/C5CP04410C (2015). doi:10.1039/C5CP04410C
36. Ren, Z. *et al.* Thermal Assisted Oxygen Annealing for High Efficiency Planar $CH_3NH_3PbI_3$ Perovskite Solar Cells. *Sci. Rep.* **4,** 6752 (2014).
37. Yin, W.-J., Chen, H., Shi, T., Wei, S.-H. & Yan, Y. Origin of High Electronic Quality in Structurally Disordered $CH_3NH_3PbI_3$ and the Passivation Effect of Cl and O at Grain Boundaries. *Adv. Electron. Mater.* **1,** n/a–n/a (2015).
38. De Quilettes, D. W. *et al.* Impact of microstructure on local carrier lifetime in perovskite solar cells. *Science.* **348,** 683–686 (2015).

CHAPTER IV:

VIBRATIONAL PROPERTIES OF METHYLAMMONIUM LEAD IODIDE

1. Introduction

The technology of perovskite solar cells based on the hybrid organic/inorganic perovskite absorber materials with the ABX_3 structure (A=organic cation; B=Pb and X=Cl, Br, I; where the cation is embedded in a PbX_6 octaherda) have been in the focus of the dye sensitized and organic photovoltaics research community for the past four years.[1,2]

Due to the fascinating optical and electrical properties of this material, which were discussed previously, the optimization of the devices, their stability and low cost fabrication have fueled the need for a deeper understanding of the fundamental physics of the material.

With this in mind it is important to understand which kinds of interactions are ruling the transport of the charge carriers in the organo-lead halide perovskites. Charge lifetime, separation and transport remarkable timescale questions the essence of these properties which lie in the unique structure and dynamics of the perovskite octahedral framework and the bulky organic cation.

The vibrational response of these systems can provide very useful information on the interaction of the organic and inorganic counterparts of the perovskite material. This interaction in turn gives rise to phonon-phonon, electron-phonon, spin-phonon interaction which may prove to lie in the basics of the remarkable intrinsic properties of the organic lead halide perovskites. Furthermore, recent publications suggest that charge transport in the perovskite systems has polaronic nature,[3,4] thus obtaining a more insightful knowledge on the phonon interactions is essential.

Extensive theoretical calculations have been reported on the interaction and relationship of the cation and octahedra,[5–8] however there is little experimental data on the vibrational properties of the perovskite. Experimental data on the full vibrational spectra of MAPI are relatively few with publications reporting certain spectral intervals of the IR spectra.[7,9–11] Additionally, there have also been several published Raman studies taking into account resonant Raman data up to 500 cm^{-1}. [12–15]

In order to provide a full vibrational study of Cl-doped MAPI (from here on addressed only as MAPI), the infrared and Raman spectrum in the frequency range 30-3400 cm^{-1} in the temperature interval form 80-360K, covering all three crystal phases was recorded. The study and the investigation of the dynamics behind both, high and low temperature phase transitions were performed. Investigation in to all three phases of the MAPI and the nature and mechanism of the phase transition should provide important insight in to the constraints of the cation, and the distortion of the inorganic frame. This in turn can answer serious questions about the charge separation and transfer properties of the material. Hydrogen bonding (H-bond), which has already been proposed by several research groups as an imperative to ferroelectric response and spontaneous polarization,[16,17] can undoubtedly have a crucial influence to device operation. Recently, the effect of temperature on the photovoltaic parameters,[18] as well as charge carrier dynamics[19] have

been performed with the intention of understanding the change in device operation with temperature.

The deeper insight into the vibrational fingerprint of the MA cation, such as mapping the timescale of the motion and potential barriers of the oscillators involved in the cation rotation, as well as probing the infrared and Raman spectroscopy response throughout the phase transitions from cubic to tetragonal to orthorhombic, can provide essential information on the charge interaction and transport through the material. When coupled with powerful computational tools the experimental results from phonon interactions and cation dynamics can facilitate the methodology of manipulation of basic structural components of the perovskite materials such as cation and metal exchange to serve towards further optimization of the PSC technology.

The situation of the cation interacting with the inorganic framework complicates the description of the vibrational characteristics of the system, giving rise to series of overlapping bands, resonance effects, and anharmonicity and phonon interactions. Since orientational disorder, static or dynamic or both, must be present in the crystal as a consequence of the non-coincidence of the crystallographic site and the molecular cation symmetries,[20] investigating the temperature dependence of the frequency of vibrational modes provides insight on the nature and the mechanism behind the phase transition. Moreover, photoinduced IR absorption measurements can identify the existence of polarons and further contribute to the understanding of the charge transport properties. The obtained novel results present fundamental step forward, towards a full overview of the liberating and limiting factors of charge transport in this perovskite material.

1.1. Material Structure

The research interest in the perovskite solar cell, since the first publication, has produced many research lines in order to both quantitatively and qualitatively account for the high efficiency of these types of cells. Exploring the tunability of the band gap of the $CH_3NH_3PbI_3$ (MAPI), publications on Cl and Br doped $CH_3NH_3PbI_3$ solar cells, as well as pure $CH_3NH_3PbBr_3$ (MAPB) followed soon after.[21,22] Namely, the band gap of the $CH_3NH_3PbI_3$ has been experimentally reported to be in the range 1.5-1.6 eV, Cl doped $CH_3NH_3PbI_3$ has a similar band gap around 1.55, and the Cl or I doped $CH_3NH_3PbBr_3$ band gap can be fine-tuned in the range 1.55-2.30 eV depending on dopant atomic concentration.[23]

Since the material structure in general represents a combination of both organic and inorganic parts and properties, the optical and electrical characteristics of this material are undoubtedly connected to its structure. The first structural and spectroscopic instigation of this specific group of organic inorganic perovskite materials was reported several decades ago.[24,25] The methylammonium lead iodide crystal structure was determined to have 3 structural phases;[25] high temperature cubic phase T_{C1}=327.4K with a *Pm*3*m* symmetry, room temperature tetragonal with *I*4/*mcm* symmetry which transitions to low temperature orthorhombic phase at T_{C2}=162.2K with $Pna2_1$ symmetry. Models of the structure of the 3 crystal phases of MAPI are presented in Figure 1. The symmetry of the cation however does not correspond to the summitry of the inorganic framework and it is classified with the symmetry group C_{3v} of an isolated cation. Due to this natural complexity of the $CH_3NH_3PbI_3$ molecule which does not possess a center of symmetry, all of the normal modes will be both IR and Raman active.

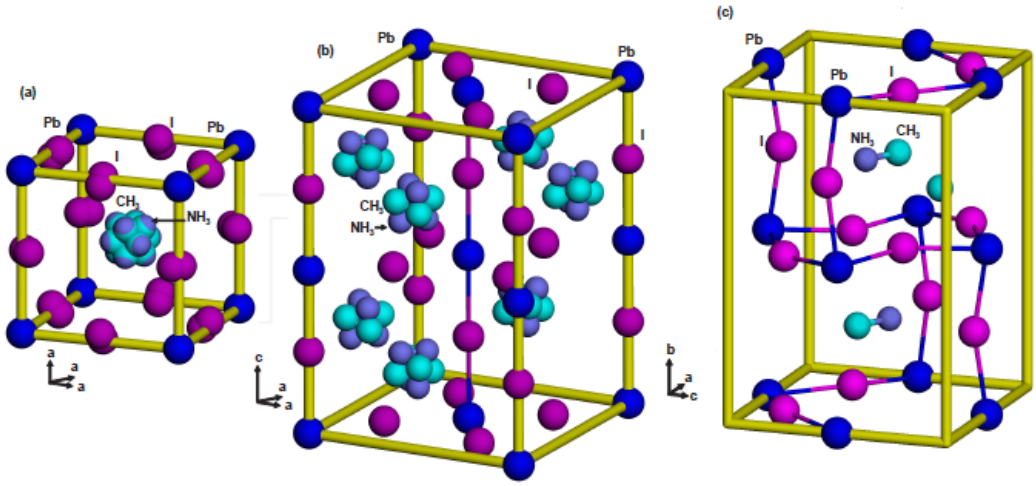

Figure 1. Model of crystal structure of the $CH_3NH_3PbI_3$ in the different crystal phases: a) cubic; b) tetragonal; c) orthorhombic.[26]

2. Experimental-Materials and Methods

All chemicals except for the ones stated otherwise, were acquired from Aldrich, Fluka and used without further purification.

2.1. Material Preparation

The Cl doped $CH_3NH_3PbI_3$ perovskite material has been prepared from solution according to published procedure.[27] Methylammonium iodide CH_3NH_3I was prepared by mixing 24 ml of methylamine solution (33 wt% in absolute ethanol) with 100 ml of ethanol and 10 ml of 57% HI acid. The solution was stirred for 2 hours, then transferred into a rotary evaporator and kept at 70°C until a crystalline powder formed. The crystalline powder was washed and recrystallized from ethanol and the formed methylammonium iodide was dried in a furnace at 60°C for 16 hours. The CH_3NH_3I and $PbCl_2$ were dissolved in a 3:1 molar ratio in N,N-dimethylformamide (DMF) to form a 40 wt% Cl-doped $CH_3NH_3PbI_3$ perovskite precursor solution.

2.2. Material Characterization

Optical absorption. The MAPI solution was deposited by spin coating on clean glass slides (washed by subsequent ultrasonic baths of water, acetone and isopropanol and treated with O_2 plasma) and annealed at 95°C in a nitrogen filled glove box with relative humidity of 20±3% for 70 min. PMMA coating (Allresist 671.05) was deposited on top by spin coating before transferring the sample for measurement. Absorption measurements were performed with JASCO V-550 UV-Vis spectrometer with PMMA-coated glass slides as a reference.

X-Ray detraction (XRD) measurement. Sample preparation was identical to the previously described sample preparation without the deposition of PMMA. After preparation the sample was immediately transferred for measurement. The crystal structure was characterized by performing off-specular scans with the incident angle fixed to 0.8°. Measurements were carried out by using a SmartLab-Rigaku diffractometer, equipped with a rotating anode (Cu Kα λ = 1.54180 Å) followed by a parabolic mirror, to collimate the incident beam, and a series of variable slits (placed before and after the sample position).

Far-infrared (Far-IR) absorption. The MAPI solution was deposited by spin coating on a 0.5mm thick non-doped Si substrate which was previously cleaned in subsequent ultrasonic baths of water, acetone and isopropanol and treated with O_2 plasma prior to deposition. The perovskite film was burned at 95°C in a nitrogen filled glove box with relative humidity of 20±3% for 2 hours. PMMA coating (Allresist 671.05) was deposited on top by spin coating before transferring the sample for measurement. Far-IR absorption spectra were obtained by using a Bruker 113v FT-IR interferometer equipped with Hg lamp, DTGS detector with scan velocity 0.1 kHz, 2 cm^{-1} resolution averaging over 256 scan. In order to optimize the quality of the spectra in the Far-IR spectral range we have investigated (25-450cm^{-1}), at each temperature, four spectra were collected by using four distinct mylar beamsplitters (50 μm, 12 μm, 6 μm and 3.5 μm). A clean Si substrate was used as a reference, since PMMA has no vibrational response in this frequency region. Temperature dependent measurements were performed mounting the sample on the cold finger (with a 6 mm aperture hole) of a flow cryostat with HDPE windows with the MAPI in direct contact with the copper cold finger. The temperature was monitored by ITC4 Oxford temperature controller.

Mid-infrared (Mid-IR) absorption. Samples for the mid IR absorption measurement were prepared in the same way as described in the Far-IR sample preparation section sans the deposition of the PMMA. The measurement was performed with Bruker Vertex 70 interferometer using a DLaTGS detector and a KBr beamsplitter. The sample was placed with a direct contact on the cold finger (with a 5 mm aperture hole) of a flow cryostat with KBr windows. Clean substrate was used as a reference prior to sample measurement. The recorded spectral region was 400-4000 cm^{-1} with a scan velocity of 10 kHz and spectral resolution of 4 cm^{-1}. The temperature was monitored by ITC4 Oxford temperature controller. The baseline removal and band fitting (mixed Lorentzian-Gaussian function) of the collected spectra was performed by Opus 7.2.

Fourier transform Raman (FT Raman) measurements. MAPI solution was drop casted on clean glass substrates and annealed at 95°C in a nitrogen filled glove box with relative humidity of 20±3% for 20 hours to ensure compete perovskite formation and solvent evaporation. The material was scratched and placed in a custom made brass sample holder by tightly filling a cylindrical hole of 1x1 mm (height x diameter). The sample holder was mounted in a flow cryostat in direct contact with the copper cold finger. The temperature was controlled by ITC4 Oxford temperature controller. Measurement was performed with Bruker RFT 100 exciting with a 1064 nm Nd/YAG diode pumped c.w. laser. The size of the laser spot on the sample was 1 mm in diameter. The spectra were collected in backscattered geometry with a liquid nitrogen cooled Ge diode detector; 5mm aperture and a quartz beamsplitter were used. The scan velocity was 5 kHz, resolution 4 cm^{-1} and the laser power was kept at 25 mW. To ensure good signal to noise ratio more than 4000 scans were collected for each temperature. The band fitting (mixed Lorentzian-Gaussian function) was performed by Opus 6.2

Photoluminescence (PL) measurement. The sample preparation is identical to the sample preparation for the absorption measurement described previously in this section. Continuous wave PL measurement was performed by Micro-Raman Renishaw 1000

system with λ_{ex}=488 nm. Laser power density of 430 mW/cm^2 was attenuated with a filter to prevent thermal degradation of the sample.

Photoinduced Absorption (PIA). The sample preparation for the PIA measurement was identical to the sample preparation for the Far-IR. The measurement was performed by Bruker 113v FT-IR interferometer in vacuum, equipped with Hg lamp and DTGS detector. Photoexcitation was achieved with c.w. Ar+ multiline laser with power density of 40 mW/cm^2 (for further details on the experiment and theoretical background please refer to the Appendix section). Temperature dependent measurements were performed mounting the sample on the cold finger (with a 6 mm aperture hole) of a flow cryostat with HDPE windows with the MAPI in direct contact with the copper cold finger. The temperature was monitored by ITC4 Oxford temperature controller.

3. Results and Discussion

Reports on the diversity on solar cell parameters with respect to cell configuration, as well as the material preparation and crystalline size,[13] have indicated that the electronic properties of the MAPI are strongly influenced by specific experimental conditions during the formation of the perovskite. In order to corroborate the study of the vibrational properties of the material, the investigation was supported not only by device preparation and characterization as described in Chapter II and III, but furthermore, absorption, PL and XRD measurements at room temperature. The results presented in Figure 2 and Figure 3 correspond very well to published results of the proper material structure.[13,28]

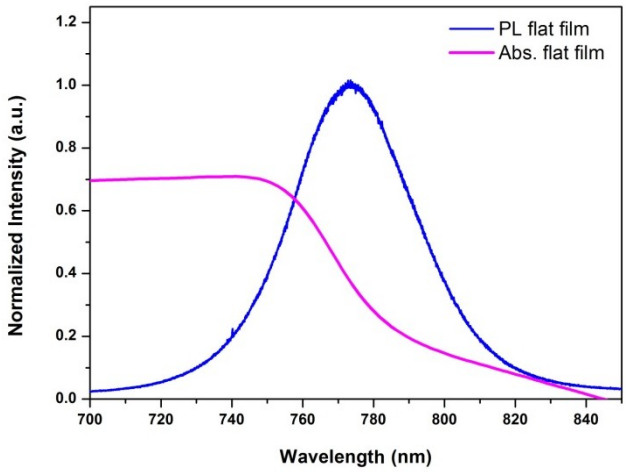

Figure 2. PL and optical absorption of a MAPI film.

Furthermore, it is important to note that all the investigation is conducted on a solution processed material as prepared for solar cell application, which is important since the polycrystalline perovskite material used in optoelectronic devices can be subjected to defects and impurities[29] and effects due to grain size and boundaries which can affect the charge generation and transport.[30]

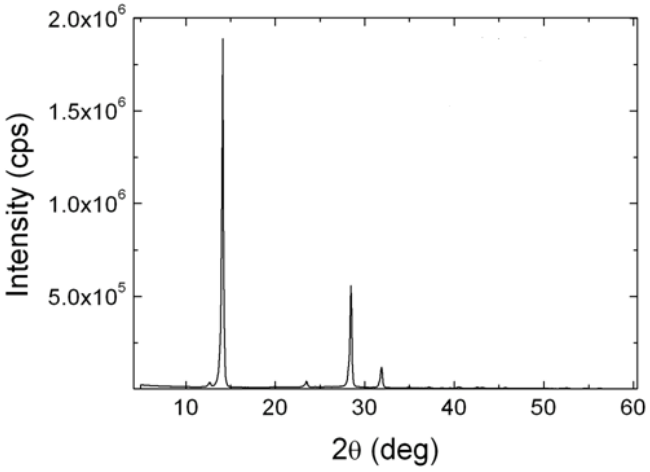

Figure 3. X-ray diffraction pattern of the MAPI structure.

3.1. Temperature Dependent Infrared Spectra

IR spectra were collected from MAPI films deposited on Si substrates (refer to Section 2.1 and 2.2. for details). The IR spectra for all three phases of the MAPI are reported in Figure 4. The data is consistent with published experimental work regarding the mid IR region of both orthorhombic[11] and the tetragonal phase.[31] The assignment of the vibrational modes was made on the bases of previous published and recent (unpublished) computational results.[7,12,32] According to previous work on methylammonium halides[33,34] the internal modes of the MA cations are found at high frequencies, whereas at lower frequency only the torsional motion of the MA cation can be observed above 400 cm^{-1} for all MAX crystals (X=Cl, Br, I). For the perovskite MAPI, the full vibrational assignment of both external and internal cation modes and lattice vibrations can be divided in four spectral regions:

1. Below 450 cm^{-1}: inorganic + librations + MA torsion
2. Between 800-1200 cm^{-1}: internal MA motion (bending modes + CN stretching)
3. Between 1200-1700 cm^{-1}: internal MA motion (bending modes)
4. Above 2700 cm^{-1}: internal MA motion (CH and NH stretching)

The Far-IR spectra of the MAPI are reported in Figure 4a. The vibrational spectra in the low frequency region are due to the motion of the inorganic cage and the MA cation libration motion. The latter are simply “roto-translations” within the inorganic cage, around an axis and/or along a certain direction within the inorganic framework reference system. These vibrational modes are not purely associated only to the inorganic or to the MA librations but instead are of mixed nature.

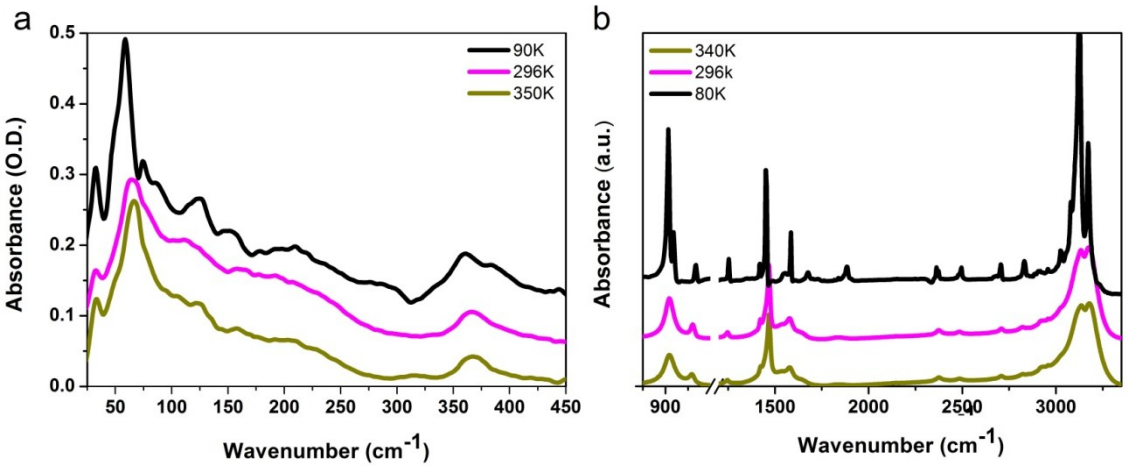

Figure 4. Infrared spectra of MAPI: a) from 25-450cm^{-1} (spectra are stacked for better viewing); b) from 850-3275cm^{-1}(296K and 340K spectra are scaled with respect to the spectra at 80K by 3 times for better viewing).

The modes observed at the low frequency part of the spectra, associated in most part to the inorganic cage, are around 100 cm^{-1} but they have generally no IR activity. At the opposite, the modes of the inorganic cage dominate in the region around 60 cm^{-1} and lower frequencies. Thus, the inorganic cage contributes mostly to the IR activity in the very low frequency region (60 cm^{-1}), while the signals from 70 cm^{-1} up to 150 cm^{-1} are mainly due to MA cation librations. The signals at 350 cm^{-1} of the IR spectrum are assigned to the vibrational torsional motion of the MA cation, which is the internal vibrational mode with the lowest frequency. This low frequency part of the spectra is difficult to resolve considering that both the lattice modes and the external modes of the MA are overlapping in the same region. This region in the vibrational spectra is very important since information on the interaction of the MA with the organic framework can be found here; however the interpretation of the data is relatively ambiguous considering the overlapping of the phonon density of states, thus the following assignment is made on the basis of computational and published Raman data.[7,12]

Regarding the lowest part of the Far-IR spectra in the orthorhombic phase, the bands at 33; a shoulder at 47 and a band at 59 cm^{-1} are assigned to Pb-I bending and roto-vibrational motion of the cation. A variety of modes above 60 cm^{-1} have been theoretically predicted in this frequency region where one expects coupled vibrations of the inorganic cage and external modes of MA as well as pure cation external vibrations. The modes at 74 cm^{-1} and the one at 86 cm^{-1} mainly associated to Pb-I vibrations, the modes at 115 and 124cm^{-1} are roto-translational modes of the organic cation, the 151 cm^{-1} is roto-vibrational motion of the cation. The mode around 210 cm^{-1} has not been predicted by calculation, however it has been observed in the IR spectra of similar systems with MA cations,[35] regardless, it cannot be excluded that this mode might appear due to local defects (impurities and or vacancies) or extended defects (grain boundaries) in the material. The broad band around 360 cm^{-1} is cautiously assigned to the torsional vibration of the cation. The mid IR spectra of MA are reported in Figure 5.

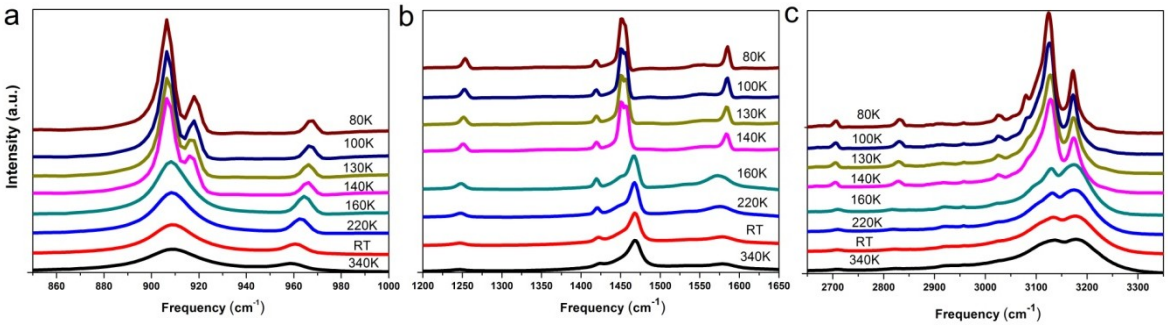

Figure 5. Temperature dependent IR spectra (stacked) in the spectral region from a) 850-1000cm^{-1}; b)1200-1650cm^{-1}; c) 2650-3350cm^{-1}.

In these energy regions only the internal mode vibrations of the MA are expected. The full assignment of the internal modes is reported in Table 1.

Table 1. IR mode assignment of the internal vibrations of the MA in MAPI for all three structural phases.

IR mode	**Orthorhombic 80K**	**Tetragonal RT**	**Cubic 340K**
	(cm^{-1})	(cm^{-1})	(cm^{-1})
out-of-phase twisting of the CH_3 and NH_3 group	906	909	909
out-of-phase wagging of the CH_3 and NH_3 group	918		
CN stretching	967	961	959
in-phase twisting of the CH_3 and NH_3 group	1253	1247	1246
umbrella CH_3 bending (symmetric scissoring)	1418	1421	1423
asymmetric scissoring of the CH_3 group	1451	1456	1457
umbrella NH_3 (symmetric scissoring)	1456	1468	1469
asymmetric scissoring of the NH_3 group	1550; 1585	1534; 1579	1532; 1579
CH symmetric stretching	2957	2957	2959
CH asymmetric stretching	3024; 3030	3022	3022
NH symmetric stretching	3079; 3107		
NH asymmetric stretching	3124	3134	3136
NH asymmetric stretching	3172	3178	3178

It is clearly seen from Figure 4b that in addition to normal mode vibrations we see a variety of overtones and combinations, however since their frequency dependence is not investigated in light of offering more information to the internal vibration of the MA or the coupling with the inorganic framework, their assignment is deemed of less importance for the current study. The temperature dependent IR spectrum provides information on the change in molecular bonds and phase transition mechanism, granting insight into the

interaction between the cation and the framework. As evident form Figure 5 all modes undergo a clear shift and narrowing upon the T_{C2} phase transition, as well as, an increase in intensity with lowering of the temperature. Additionally, several modes experience a clear band splitting as a result of reduction of freedom of rotation and symmetry reduction when crossing from a higher symmetry phase such as the tetragonal to the orthorhombic.[36] The experimental results place the phase transition T_{C2} around 150K. The lower temperature for the tetragonal to orthorhombic phase transition with respect to pure MAPI it's not unusual for the Cl-doped system.[30]

A more detailed inspection of the vibrational frequency shifts of around 10 cm^{-1} and more for almost all internal vibrations of the MA, throughout the entire temperature range (80-360K), indicate highly anharmonic crystal vibrations which is not unusual for similar organic-inorganic systems.[37,38] These pronounced changes indicate that the approximation of a harmonic potential when describing the vibrational modes is insufficient.

The second region of the IR spectra (Figure 5a) is clearly associated to the bending of the CNH and NCH bond angles. According to theoretical simulations[32] any deviation from the symmetry, as due to defects, thermal motion (still present at 80 K) and anharmonic effects are expected to mix these coordinates.

The band at 968 cm^{-1} is assigned to C-N stretching modes which softens with increasing temperature and undergoes a continuous shift and line broadening throughout the entire temperature range as presented in Figure 6c.

In the IR spectrum, three main bands are observed in the orthorhombic phase at 906, 918 and 967 cm^{-1}. The first band is assigned to the twisting of the CH_3 and NH_3 groups which move "out-of-phase" with respect to a hypothetical axis within the MA cation. The second band can be mainly assigned to wagging where the CH_3 and the NH_3 group move "out-of-phase". The detailed inspection of the temperature changes of the IR modes shows clear splitting of the "wagging" and "twisting" band. The splitting indicates changes in the hydrogen bonding which can restrict the motion of these groups and a certain differentiation and freezing of the vibrational motion at T_{C2} is observed. There is an abrupt line broadening of the out-of-phase twisting of the CH_3 and NH_3 mode above 150K confirming that there is a sharp change in the motion of CH_3 and NH_3 about the C-N axis which seems to be much less constrained in the tetragonal phase. The abrupt changes of the position of the twisting and wagging of the CH and NH modes confirms the first order phase transition from orthorhombic to tetragonal phase. These changes and line broadening can be associated with the prominent role of the organic cation on the phase transition. The temperature changes of the peak position and FWHM of MA internal modes are presented in Figure 6.

The third frequency region is associated with the bending of the CNH and CHN bond angles. In the IR spectrum, four vibrational signals at 1253 cm^{-1}, 1418 cm^{-1}, 1451 cm^{-1}, 1585 cm^{-1} are found. The band at 1253 cm^{-1}, corresponds to a twisting mode, where the CH_3 and the NH_3 groups twist "in-phase" with respect to a hypothetical screw axis. The band at 1418 cm^{-1} is associated with the umbrella modes of the CH_3 group or symmetric scissoring. The band at 1451 cm^{-1}, has two components, because of its asymmetric shape, and it is associated to asymmetric scissoring modes of the CH_3 group. The CH_3 bending modes show hardening with the increase of temperature indicating changes in the CH bond strength, which increases upon heating. The mode at 1585 cm^{-1} is mainly due to NH_3 asymmetric scissoring modes. A noticeable anomaly of this mode (Figure 6d) is present in the tetragonal phase. The mode hardens and the linewidth is slightly decreasing, the same anomalous behavior is present in the Raman spectra and will be discussed latter.

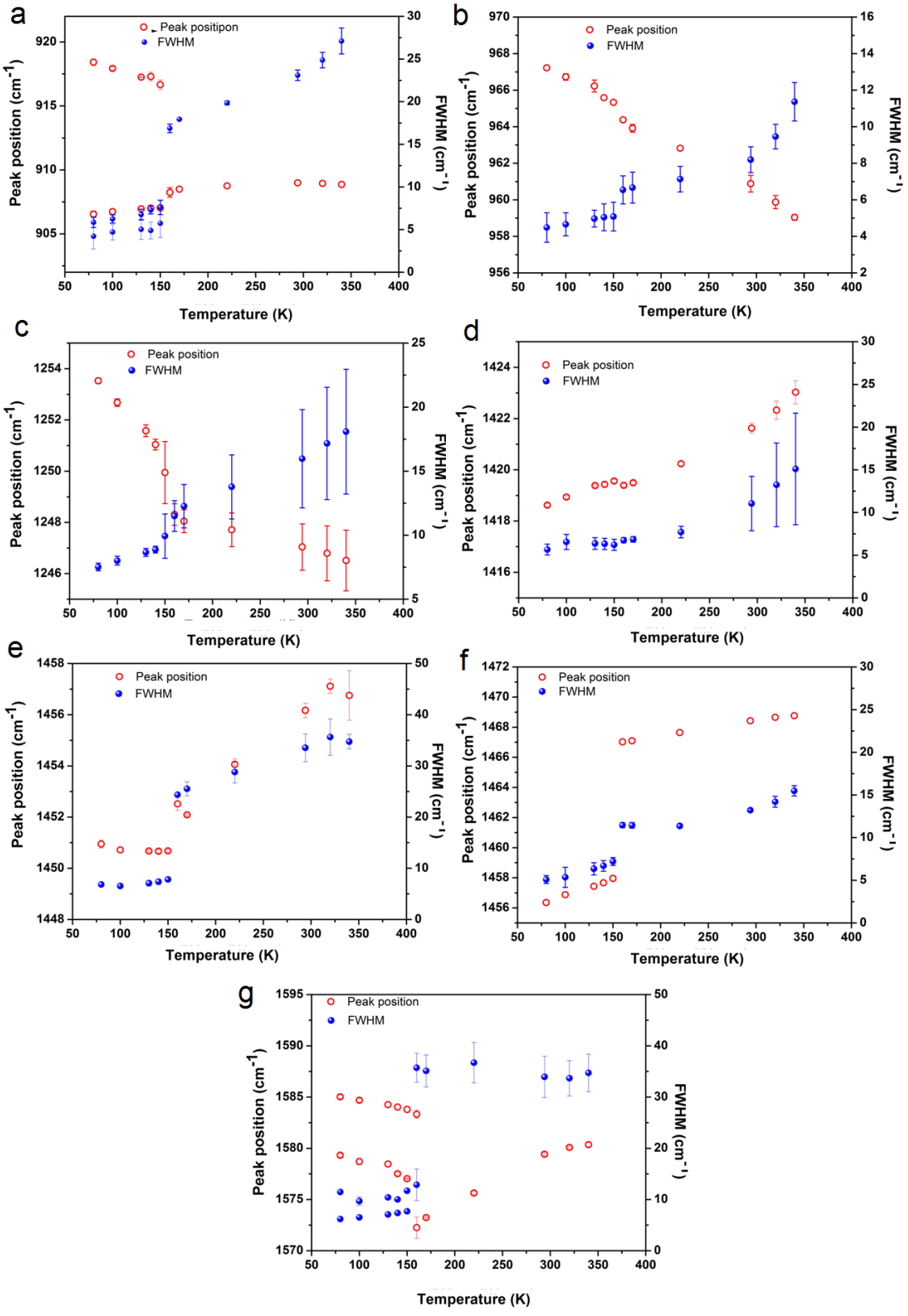

Figure 6. IR peak position and FWHM of MA internal modes: a) MA out of phase twisting and wagging; b) C-N stretching; c) MA in phase twisting; d) CH_3 sym. bending; e) CH_3 asym. bending; f) NH_3 sym. bending; d) NH_3 asym. bending.

Of great importance for the MAPI and its microscopic as well as macroscopic properties is the hydrogen bond. Hydrogen bonding (H-bond) has been reported for a variety or organic-

inorganic perovskite materials[39,40] and recent IR spectra have confirmed the presence of medium to strong H-bond in $MAPbX_3$.[31] The change in the vibrational signature of the NH modes is a clear evidence of the H-bond strength which increases with decreasing temperature, a marker of cation ordering. Both NH sym. and asym. bending modes show abrupt shifts at T_{C2} as evident from Figure 5b and Figure 6 f and g. The sym. NH_3 bending mode shifts to lower frequencies for about 10 cm^{-1} indicating an increase of H-bond going from tetra to ortho. Similar behavior is observed for the asym. NH_3 bending mode which splits as a result of symmetry change and freezing of oscillator motion. This mode softens with increase of temperature till T_{C2} after which continues to harden in the tetragonal to cubic transition. The hardening of the CH_3 bending modes as well, shows that changes in the bond strengths affect the CH_3 part of the MA and confirm the complexity of the interaction of the MA and the inorganic cage. The CH_3 end of the MA is most likely less but not completely unaffected by interaction with the PbI_6 in its vibrational motion.

In the fourth region of the spectra presented in Figure 5c, three main bands can be observed, at 3079, 3124 and 3172 cm^{-1}. The band at 3079 cm^{-1} is assigned to the NH symmetric stretching. The most intense band found experimentally at 3124 cm^{-1} can be assigned to asymmetric stretching. The sp^3 C-H stretching modes are known to show energies in the 2800-3000 cm^{-1} spectral range so they can be tentatively assigned to the low intensity modes present at 2957 and 3030 cm^{-1}, with the latter mode (asym. stretch) splitting in the orthorhombic phase. Thus, it seems that the IR spectrum in this frequency region is essentially associated to the NH stretching. The band found at 3172 cm^{-1} could be associated to NH stretching however in light of the large splitting between the components (~50 cm^{-1}) its assignment appears unlikely. Since the intensity of this band is non negligible it is improbable that this mode is an overtone, and thus it can be tentatively assigned to the NH stretching of MA cations in some disordered material region.

As a consequence of the hydrogen bonding the NH stretching region has been shown to lower in frequency in comparison to that of an isolated molecule. Indeed, the measurements identify two similarly intense broad bands in the tetragonal and cubic phase corresponding to the NH stretching vibrations. It is difficult to resolve single optical modes since these bands are most likely composed of several overlapping bands as evident from their asymmetric shape. However, decreasing the temperature ensures a line narrowing which enables the identification of three modes, which show a continuous shift towards lower frequency with decreasing temperature. The two main NH stretching bands also change their relative intensity. The mode splitting and changes of the NH stretching and rocking modes has already been reported in similar systems.[41,42] The large vibrational shifts and line broadening for the NH modes going from ortho to tetra indicate MA interaction with the PbI_6 octahedra. This demonstrates that just an intermediate strength of interaction is mainly responsible for the dynamics and phase transitions of order–disorder type. The pronounced changes in the MA twisting and wagging modes at transition indicate that the cation plays a major role in the phase transition which is accompanied by inorganic cage distortion.

Regarding the phase from tetragonal to cubic (T_{C1}) phase, there is no evidence of an abrupt change but rather both the lineshift and broadening appear to be continuous. This can be due to fact that a clear change to cubic phase is not observable in this material, as recently suggested.[43]

3.2. Temperature Dependent Raman Spectra

The non resonant Raman spectrum of MAPI in the 45 to 3400 cm^{-1} range and in the temperature interval from 80K till 360K is reported in Figure 7 and Figure 8. The laser excitation of 1.16 eV, at which the material is transparent (well below the optical band gap of the MAPI of 1.6 eV), ensures that no degradation and/or PbI_2 formation will occur, as proposed by Ledinsky *et al*.[44]

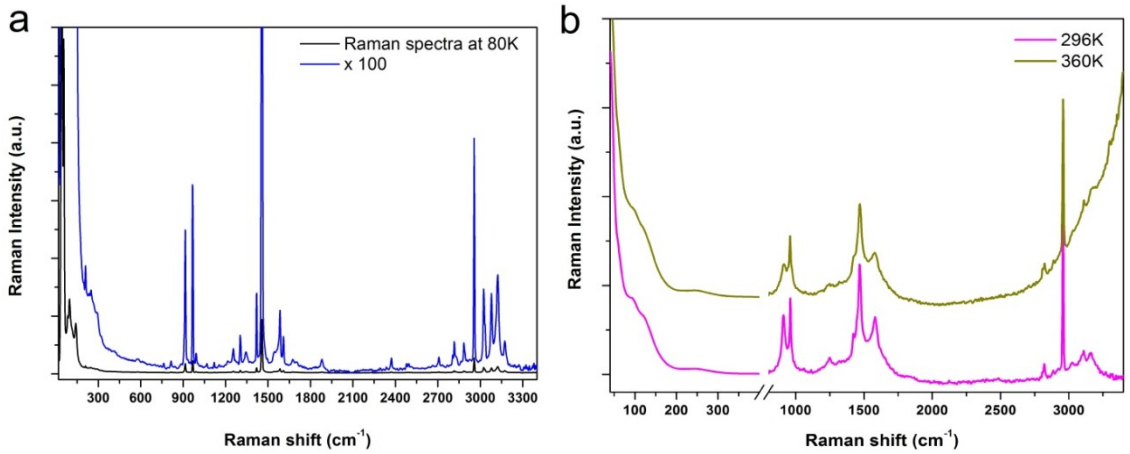

Figure 7. MAPI Raman spectra: a) orthorhombic phase; b) tetragonal and cubic phase, the spectra are stacked and the intensities before and after spectral break are adjusted for better viewing.

The measurement provided the temperature evolution of the vibrational modes of the MAPI. The normal modes of the MA are corresponding very well with the theoretical prediction[32] and the band frequencies observed with the IR spectroscopy as reported in Table 2.

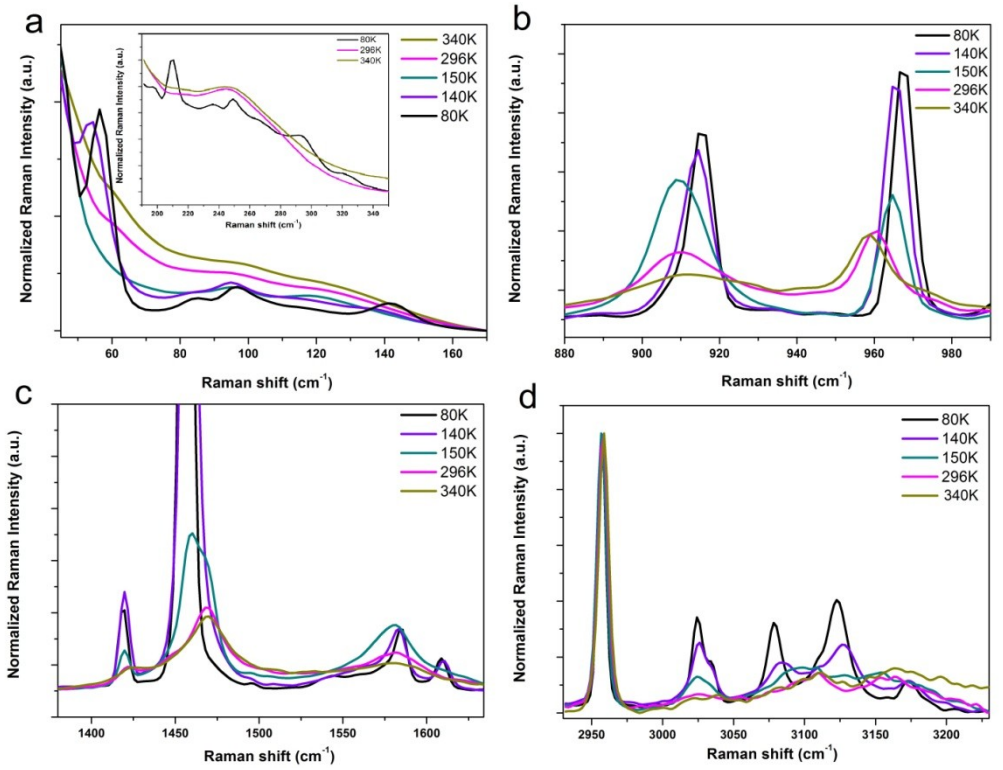

Figure 8. Temperature dependent Raman spectra of MAPI in the frequency region: a) 45-170 cm^{-1}; inset 190-350 cm^{-1}; b) 880-990 cm^{-1}; c) 1350-1650 cm^{-1}; d) 2900-3250 cm^{-1}.

Table 2. Raman mode assignment of the internal vibrations of the MA in MAPI for all three structural phases.

Raman mode	Orthorhombic 80K	Tetragonal RT	Cubic 360K
	(cm^{-1})	(cm^{-1})	(cm^{-1})
out-of-phase wagging of the CH_3 and NH_3 group	915	910	910
C-N stretching	967	960	958
in-phase twisting of the CH_3 and NH_3 group	1255	1246	1245
umbrella CH_3 bending (symmetric scissoring)	1418	1421	1423
umbrella NH_3 (symmetric scissoring)	1456	1468	1469
asymmetric scissoring of the NH_3 group	1542; 1585; 1609	1582	1583
CH symmetric stretching	2956	2958	2959
CH asymmetric stretching	3024; 3032	3029	3030
NH symmetric stretching	3078	3108	3111
NH asymmetric stretching	3122	3168	3171
NH asymmetric stretching	3172		

The specific shifts of the internal modes of the MA with temperature follow the same trend as already described in the previous section on IR spectroscopy. The frequency shift and the line broadening of several well resolved modes are presented in Figure 9.

The good quality of the low frequency region in the orthorhombic phase allows the identification of several modes which again correspond well to the IR modes presented in Figure 4a. The appearance of at least 7 new modes in the orthorhombic phase in the Raman spectra has already been observed for $MAPbCl_3$ and it has been attributed to the break-down of the symmetry and to the distortion of the $PbCl_6$ octahedra.[37]

At 80K in the orthorhombic phase we can clearly indentify several peaks. The band at 56 cm^{-1} is due to PbI_2 bending, this mode softens with temperature and after the phase transition it is no longer identifiable (Figure 9a), either because of reduced intensity or due to shift to lower frequencies which because of the experimental cutoff of the detector, is not possible to observe. The bands at 84 cm^{-1} and 97 cm^{-1} (Figure 9b) are most likely contributions from the Pb-I stretching coupled with MA librations. Bands at 112 cm^{-1} and 142 cm^{-1} (Figure 9c) are associated with libration modes of MA. At the phase transition to the tetragonal phase, the latter three modes can still be resolved, however due to the large line broadening, determination of peak position and linewidth is more difficult. Several modes with lower intensity are observed from 200 to 350 cm^{-1}. The mode around 210 cm^{-1} is observed again in the Raman spectra, this mode softens and broadens with temperature approaching the phase transition to tetragonal and in the tetragonal phase it is no longer present, thus attributing its existence to impurities or PbI_2 is less likely. Additional weak bands are observed in the region up to 350 cm^{-1}. These signals can probably be identified as torsional modes of material domains with different degree of order as suggested in literature.[15]

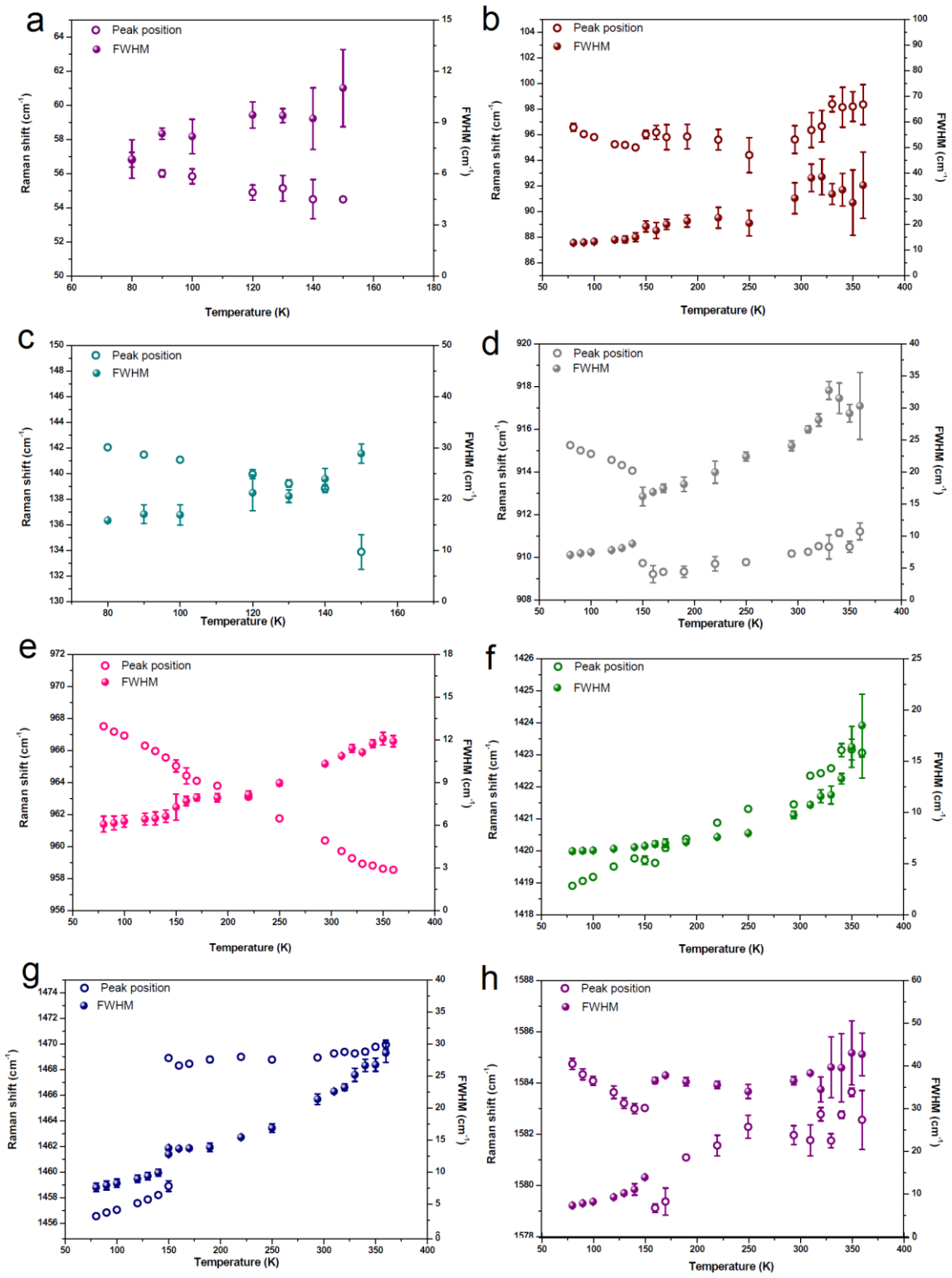

Figure 9. Peak position and FWHM temperature dependence of Raman modes: a) Pb-I bending at 56 cm^{-1}; b) Pb-I stretching at 97 cm^{-1}; c) MA libration at 142 cm^{-1}; d) CH_3 and NH_3 out-of-phase wagging at 915 cm^{-1}; e) C-N stretching at 967 cm^{-1}; f) CH_3 sym. bending at 1418 cm^{-1}; g) NH_3 sym. bending at 1456 cm^{-1}; h) NH_3 asym. bending at 1585 cm^{-1}.

It is noteworthy to mention that the experimental signal at 1304 cm^{-1} (Figure 7a) is not predicted by any vibrational mode, thus it is unreasonable to consider this peak as an

harmonic peak of the "pristine" material, however it's possible that this band is a result of some surface modes or impurities. As in the IR spectrum, the bands below 2900 cm^{-1} are overtones, and a band at 3172 cm^{-1} is observed again, however this band broadens and disappears after the phase transition in the tetragonal phase making questionable the assumption of associating this band with a NH stretching of MA cations in some impurity material domains.

Interestingly the CH stretching modes seem to show the least temperature dependence, especially the CH symmetric stretching mode which practically doesn't shift with temperature (Figure 8d). This indicates that these vibrations are particularly free and feel no restrictions regardless of the phase transition, and the CH symmetric stretching is affected by neither phonon interaction nor lattice expansion.

From the temperature dependence of the Raman spectra it can be observed that there are no major changes in the spectra going from tetragonal to the cubic phase. All bands of the cation internal modes continuously broaden and decrease in intensity, especially the twisting and wagging modes. The only mode which maintains both the peak position and linewidth throughout both phase transitions is the sym. CH stretching mode. This means that the cubic phase is most likely an average of the tetragonal with different MA orientation. These results are indicative that the character of this phase transition is more displacive rather than first order, which has already been reported for $MAPbBr_3$[45] where the MA has disordered character and the octahedron is mainly unaffected by the cation motion.[20] The Raman spectral data are also in accordance with XRD analysis showing that above 330K the MAPI adopts a pseudo-cubic rather than a cubic phase.[46]

The good quality of the spectra and the reliable results of the Raman measurement enable the extraction of important information of the MA dynamics and the physical interactions of the phonons which are presented in the next sections.

3.3. Cation Dynamics

The strong anharmonic contribution to the vibrational modes can be explained through the change in the temperature which changes the population of the energy levels of the modes, and since the levels are not equidistant the average position of the atoms changes, meaning that this change in the lattice parameters is a direct consequence of the anharmonic potential.[47] The self-diffusion mechanism is a fluctuation process in which the static or dynamic displacement of a molecule or of an atom associated with the orientational disorder or the diffuse thermal fluctuation, is characterized by jumping from one orientation to another, that is, a jump from one potential well to another. Since the orientational correlation time is the mean reorientational time of the atoms to jump from one potential well to another, the potential barrier can be extracted from the line broadening.[48,49] However the clear presence of anharmonicity in the vibrational spectra of the MAPI no longer allows the consideration that the line broadening of the modes is due only to orientational relaxation, but also vibrational relaxation, meaning that the activation energy cannot be calculated using an Arrhenius plot.[48,49] For phonon modes for which the condition of $\omega^2\tau_c^2 >> 1$ is satisfied (where ω is the harmonic frequency of the mode and τ_c is the orientational correlation time), the linewidth can be approximated to account for the vibrational relaxation (anharmonic effects) and the reorientational relaxation:

$$\Gamma = a + bT + c\exp\left(-\frac{E_a}{kT}\right) \quad (1)$$

where a, b and c are constants related to broadening arising from structural and compositional defects, anharmonic contribution (approximated as a linear term) and the orientational mechanism, respectively; Γ is the linewidth, k is Boltzmann constant, E_a is the activation energy and T is the absolute temperature.

Since the evidence of cation interaction with the inorganic framework through hydrogen bond was discussed in the previous sections, this interaction could be responsible for different potential barriers for the reorientation of different modes and different relaxation times with different halide ions.[25] The strength of the H-bond and the extent of interaction with the inorganic cage can be evaluated, and the extraction of the activation energy for the reorientation of different internal modes, can give insight into the phase transition and the orientational dynamics of the cation. This detailed mapping of the reorientational mechanism in the MAPI can allow efficient material tailoring and manipulation on an atomic level to suit and impact desired device application and efficiency.

However, close attention needs to be paid to the abrupt shifts of the phonon modes at the phase transition which clearly indicates that we have two different energy barriers and two different regimes of phonon interaction in different phases. For the purpose of this investigation only the orthorhombic and tetragonal phase were taken in consideration. The activation energy was extracted from the fit of the FWHM experimental data of the Raman modes presented in Figure 9. The fitted curves and parameters are presented in Figure 10 and Table 3.

The MA cation has two types of orientational disorder; one is the orientation of the C-N axis relative to the crystal axes and the other related to the rotation around the C-N axis. The value of the activation energy which the bending vibrational modes of the MA are probing can prove insightful in the energetic limitations driving the cation motion. As evidenced from Table 3, the activation energies of the orientational movement for all vibrations are in the same order of magnitude. However, certain changes are seen between the height of the potential (barrier) between the orthorhombic and tetragonal phases. As evidenced (Table 3), the activation energy probed by the CH_3 bending modes is lower in comparison with the NH_3 bending modes indicating that the CH_3-end of the cation is less hindered due to probably weaker interaction with the cage.

These values are closely comparable to some previously observed values for rotation of the MA about the C-N axis.[9,20] The NH_3 umbrella vibration indicates that the orientation of the cation is most likely H-bond driven, the activation energy in the orthorhombic phase is similar to the more complex motions of twisting and wagging and close to values reported for the reorientation of the C-N axis itself.[7,50] High value of the activation energy for the reorientation of the MA libration mode in the orthorhombic phase indicates that the roto-translational motion is relatively restricted. The activation energies derived from the analysis of all vibrational modes are smaller in the tetragonal phase, thus we can conclude that in the high temperature phase the activation energy is significantly reduced and hence there is no indication of cation ordering. These values indicate weak H-bond in the tetragonal and a medium-strong in the orthorhombic phase.

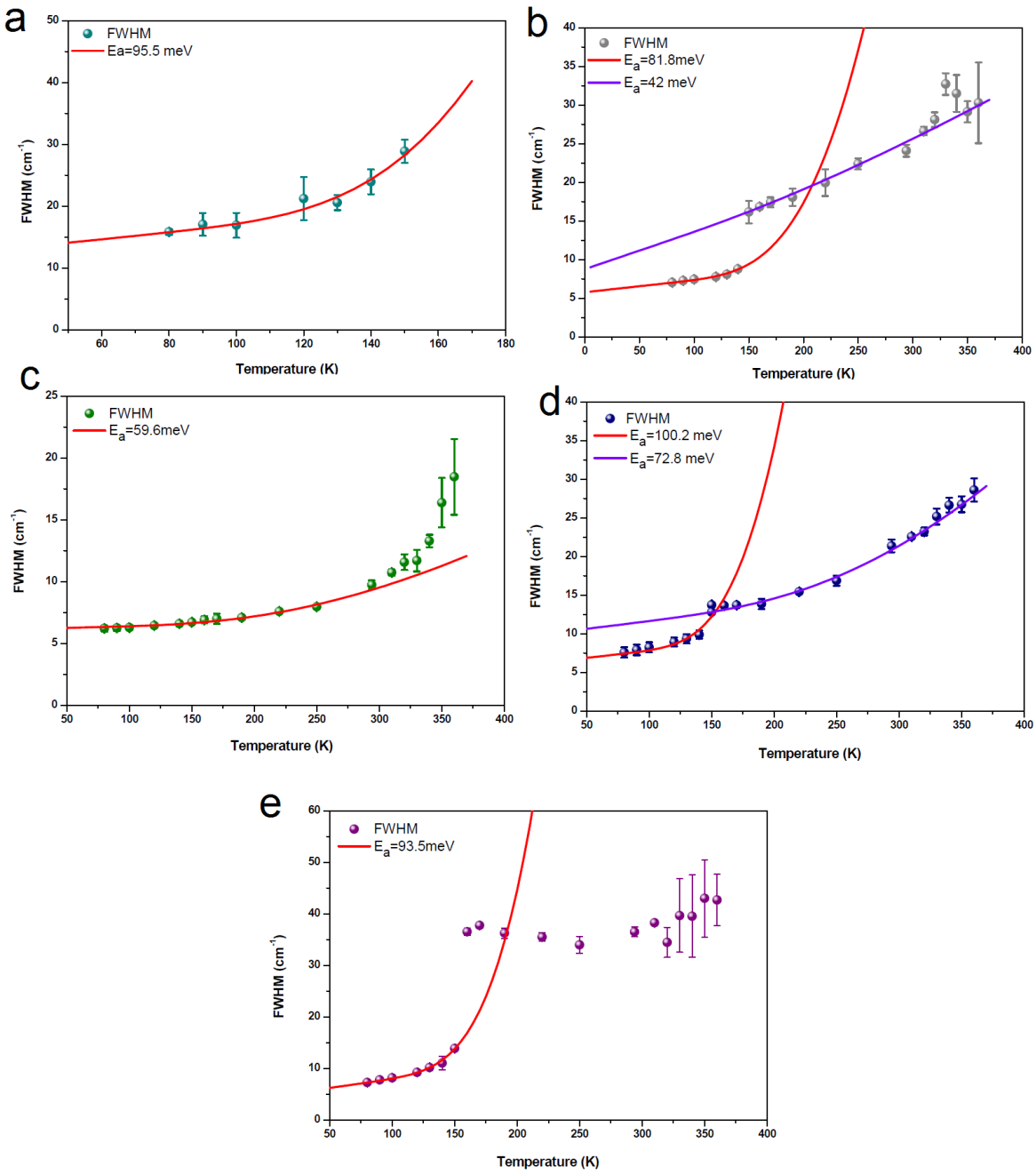

Figure 10. Temperature dependence of the FWHM of Raman modes, full lines represent fit according to equation (1) for extraction of E_a of: a) MA libration at 142 cm^{-1}; b) CH_3 and NH_3 out-of-phase wagging at 915 cm^{-1}; c) CH_3 sym. bending at 1418 cm^{-1}; d) NH_3 sym. bending at 1456 cm^{-1}; e) NH_3 asym. bending at 1585 cm^{-1}.

Table 3. Activation energy of MAPI vibrational modes

Raman mode	E_a **(meV)**	a **(cm^{-1})**	b **($cm^{-1}K^{-1}$)**	c
Orthorhombic phase				
MA libration 142 cm^{-1}	95.5 ± 10.5	11.30	0.056	9170
CH_3 and NH_3out-of-phase wagging	81.8± 2.1	5.80	0.015	785
umbrella CH_3 bending (sym. scissoring)	59.6 ± 8.3	6.13	0.002	20.6
umbrella NH_3	100.2 ± 6.2	6.00	0.018	8332
asym. scissoring of the NH_3 group	93.5±10.6	4.48	0.035	6078
Tetragonal phase				
CH_3 and NH_3out-of-phase wagging	42.0± 6.7	8.78	0.048	15.7
umbrella CH_3 bending (sym. scissoring)	59.6 ± 8.3	6.13	0.002	20.6
umbrella NH_3	72.8 ± 6.3	9.65	0.018	109.4
asym. scissoring of the NH_3 group	anomalous			

From the values of the parameter *b* in Table 3, which indicates the anharmonic contribution to the mode line broadening, the MA wagging suffers larger contribution of anharmonicity with the increase of the temperature i.e. in the tetragonal phase. This result is not surprising considering that the Umklapp processes of phonon-phonon interaction increase with temperature. Furthermore, the high values of the parameter *c* associated with the orientational mechanism suggest that the orientational mechanism has a stronger contribution to the mode dynamics for the modes involving the NH motion. The activation energies for several modes were not extracted due to anomalous line broadening. The decrease of linewidth with increasing temperature is most evident in the asym. scissoring of the NH_3 bending mode (Figure 6d and Figure 10e). Such anomalous behavior has been reported for other perovskite systems and the change in the phonon lifetime has been attributed to spin-phonon,[51] electron-phonon and phonon-phonon interactions.[52] However, we cannot exclude that the line fitting was prone to errors due to fact that the Raman signal most likely arises from contributions of several quasi degenerate modes and not of a single vibration mode. The relaxation time of the phonon modes from equation (2) agrees well with the times extracted from the IR modes in the same manner.

$$\tau_R = \frac{1}{\pi c \Gamma(T)} \tag{2}$$

where *c* is the speed of light and *Γ(T)* is the temperature dependent FWHM of the phonon mode. These data are in good comparison to recent time resolved IR study,[53] and are one order of magnitude shorter compared to recent neutron scattering study.[54] The reorientational relaxation times in the low temperature phase are significantly longer in comparison to the tetragonal and cubic phase. Having in mind that the anharmonicity has a large contribution to the line broadening we can conclude that in the high temperature phases the reorientational relaxation is quite fast exceeding one order of magnitude difference from the orthorhombic phase.

3.4. Phonon-phonon Interaction

To quantify the phonon-phonon interaction from the peak position dependence of the temperature, two terms have to be taken into consideration;[47,55] an implicit frequency shift ΔE which is determined by the thermal volume expansion; and an explicit contribution ΔA which is determined by the thermal population of vibrational levels.

$$\omega(T) = \omega_0 + \Delta E + \Delta A \tag{3}$$

where ω_0 is the harmonic frequency, and

$$\Delta E = \omega_0 \left(e^{-\gamma \int_0^T \beta(T')dT'} - 1 \right) \tag{4}$$

where β is volume thermal expansion coefficient and γ is mode dependent Gruneisen parameter. To quantitatively investigate the anharmonic contribution from the 3 and 4 phonon processes to the vibrational modes, the approach of Klemens[55] was considered. Namely, the Raman optical phonon decays in two acoustical phonons of opposite wave vectors q belonging to the same branch, if the calculation is restricted to the quadric term, the explicit contribution of the anharmonicity becomes:

$$\Delta A = C\left[1 + \frac{2}{e^{\frac{\hbar\omega_0}{2k_BT}} - 1}\right] + D\left[1 + \frac{3}{e^{\frac{\hbar\omega_0}{3k_BT}} - 1} + \frac{3}{\left(e^{\frac{\hbar\omega_0}{3k_BT}} - 1\right)^2}\right] \tag{5}$$

where k_b is Boltzmann constant, $\hbar$ the reduced Planck constant, ω_0 is the harmonic frequency, T is the absolute temperature and the constants C and D represent the contribution of the 3 and 4 phonon processes, respectively.

In most solids $\Delta E < 0$ i.e. lattice dilation results in mode softening. Given that accurate values for the mode dependent Gruneisen parameter and values for the expansion coefficient in the orthorhombic phase are not available from literature and cannot be calculated with the available experimental data, it's not possible to extract the percentage contribution of ΔE or ΔA to the anharmonicity of the modes, nor fit the data accurately. Never the less, from Figure 6 and Figure 9 it is evident that most internal modes are hardening with the increase in temperature indicating a significant anharmonic contribution. However, since the volume expansion does not influence the broadening of the linewidth, the anharmonicity contribution due to the phonon relaxation can be expressed through the temperature dependence of the FWHM of the phonon modes.

To quantify the phonon-phonon interaction, equation (6) is used, in which for the vibrational mode line broadening the anharmonic contribution from three and four phonon relaxation processes is taken into consideration.

$$\Gamma(T)=\Gamma_0+A\left[1+\frac{2}{e^{\frac{\hbar\omega_0}{2k_BT}}-1}\right]+B\left[1+\frac{3}{e^{\frac{\hbar\omega_0}{3k_BT}}-1}+\frac{3}{\left(e^{\frac{\hbar\omega_0}{3k_BT}}-1\right)^2}\right] \quad (6)$$

Equations (5) and (6) contain the same terms describing the contribution of the 3 and 4 phonon processes. The temperature independent term Γ_0 arises from phenomena such as: defects, isotopic mixture and or resolution of measurement, whereas, the constants A and B address the phonon interaction contributions equivalently to the C and D constants from equation (5). The anharmonicity constants extracted from the experimental data by fitting equation (6) are plotted in Figure 11 and are presented in Table 4.

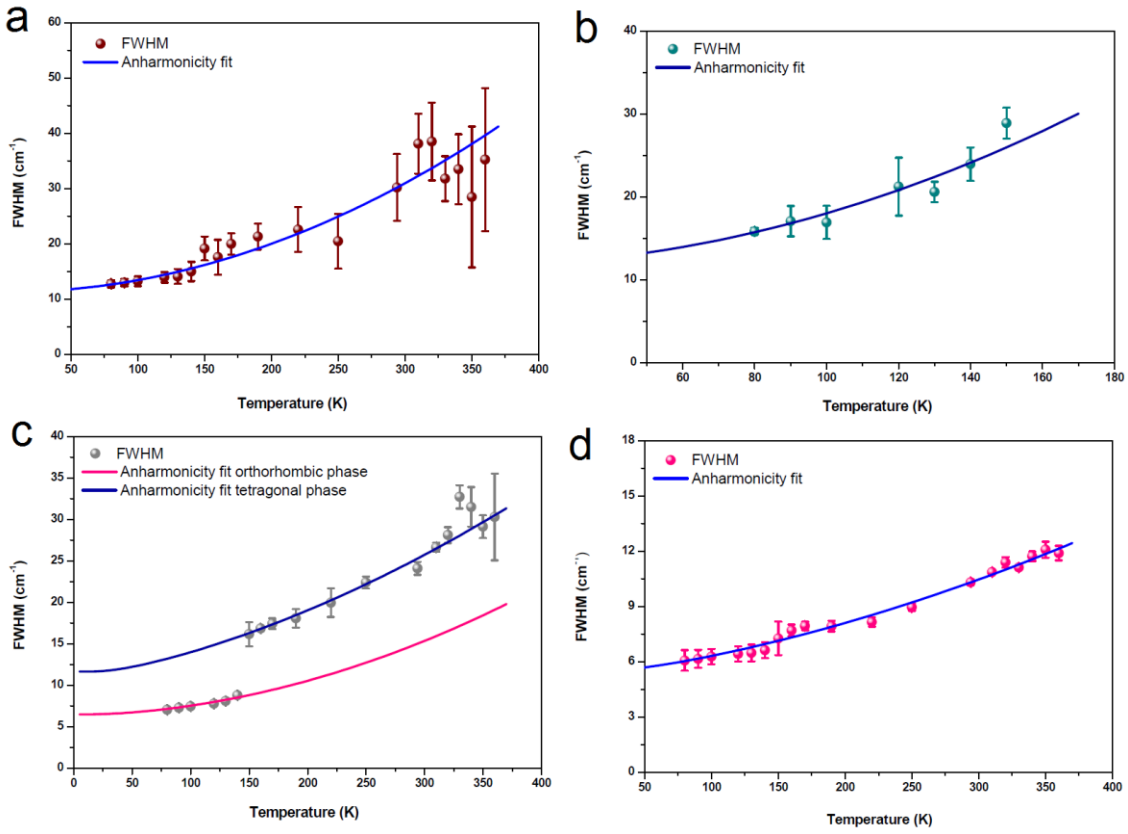

Figure 11. Temperature dependence of the FWHM of Raman modes, full lines represent fit according to equation (6) for extraction of the anharmonic contribution of: a) Pb-I stretching at 97cm^{-1}; b) MA libration at 142 cm^{-1}; c) MA out-of-phase wagging at 915 cm^{-1}; d) of C-N stretching at 967 cm^{-1}.

From Table 4 and Figure 11 it can be seen that the anharmonic behavior is dominated by the 3 phonon interactions while the contribution of the 4 phonon processes to the anharmonicity of the modes is generally small. Larger anharmonic contribution is seen in the wagging mode, while in general the internal modes have larger anharmonicity. The C-N stretching mode shows the same anharmonic contribution throughout all three phases. These results imply that the phonon-phonon interaction is much stronger for the MA modes with respect to PbI modes, and especially for the internal modes of the MA. Taking

into account the phonon energy behavior with increasing temperature, the shift to higher energies of many internal modes indicates an anomalous behavior, thus one cannot exclude anharmonic contribution due to other phonon coupling interactions. This assumption can be supported by the impossibility of the model to provide a quality fit of the libration mode at 142 cm^{-1} (Figure 11b).

It is important to note that the approach of Klemens[55] takes into account only normal phonon-phonon processes while the Umklapp processes are not considered. With the increase of temperature the number of phonons increases and with it the probability of inelastic scattering of the phonons increases as well, meaning that the number of decay channels could be much higher especially in the high temperature phase with the increase of Umklapp processes. The anharmonicity contribution with the increase of temperature could change resulting in a larger contribution of the anharmonic decay in the tetragonal and cubic phase compared to the orthorhombic than what has been extracted from the experimental data. This is an important physical phenomenon to take into account when arriving at conclusions of the thermal conductivity. In fact, the measured thermal conductivity shows that the MAPI is very thermally resistive in the tetragonal and cubic phases, while its conductivity starts to rise at the tetra to ortho transition and reaches a maximum well in the orthorhombic phase.[56] The Umklapp phonon-phonon interaction is practically frozen at low temperature and is the main contributor for the resistivity at high temperatures (while the normal process interaction has negligible effect on the thermal conductivity), thus the measured thermal conductivity of the MAPI should decrease in the high temperature phases. Considering the increase in strength of the H-bonding in the orthorhombic, it is possible that the thermal conductivity increases also due to the formation or strengthening of H-bonds which has been reported for polymers.[57]

Table 4. Anharmonicity constants for MAPI vibrational modes.

Raman mode	**Orthorhombic phase**			**Tetragonal phase**		
	Γ_0 **(cm^{-1})**	***A***	***B***	Γ_0 **(cm^{-1})**	***A***	***B***
Pb-I stretch 97cm^{-1}	11.3	0	0.01	11.3	0	0.01
MA libration 142cm^{-1}	11.6	0	0.01	-	-	-
MA out-of-phase wagging	6.2	0.17	0.15	10.0	1.52	0.13
C-N stretch	4.9	0.45	0.07	4.9	0.45	0.07

In an attempt to provide viable explanation of the charge transport properties in the hybrid halide perovskites, the formation of large polarons has recently been discussed in as the main physical phenomenon governing the electron diffusion length, mobility, electron-hole recombination rate and their temperature dependence.[3] Furthermore, attempts have been made to calculate the electron mobility from electron scattering of longitudinal optical (LO) phonons,[4] however, the effective mass and electron-phonon coupling constant (α) of the large polaron present a rough estimation and are yet to be correctly estimated due to a lack of experimental data. In sight of the fact that the anharmonicity considerably increases α and the polaron effective mass, the anharmonic correction to the polaron binding energy could have significant contribution especially for LO phonon energy $\hbar\omega \leq 10$ meV.[58] Having in mind that the LO phonon energies have been found in this energy region,[4] the contribution of the anharmonic potential should be taken into account in future investigation and calculation of the charge transport phenomena in the MAPI. Thus the phonon-phonon interaction study and the experimental results on the anharmonic effects of

the phonon modes of MAPI should provide fundamental insight also toward a more complete charge transport model.

3.5. Phase Transition Implication on Polarization

Poglitch and Webber[25] proposed that the ordered MA in the inorganic cage induces a acentric unit cell which could result in ferroelectric or antiferroelectric ordering. Insight into the polarizability of the perovskite has been proposed as an important issue for the deeper understanding of the stability of the molecular ordering with temperature and the ability of the molecules to change their alignment.[59] Since there is no evidence of MA ordering in the tetragonal or cubic phase of the MAPI, any polarization assigned to the spontaneous orientation of certain material domains is negligible with respect to the bulk. However, in the orthorhombic phase there is an evidence of a continuous ordering of the MA with the increase of the H-bonding and several previous studies have found negligible polarization in the tetragonal phase of only few $\mu C/cm^2$,[17,60,61] whereas, ferroelectric polarization is expected in the orthorhombic phase through the MA ordering. Further analysis of the internal vibrational modes of the cation are made by employing the pseudospin-phonon coupling model which has been applied in investigating similar perovskite systems which go through a ferroelectric phase transition of the order–disorder type.[41,62] The temperature dependence of the phonon frequency ω_i before and after the ferroelectric transition T_C follows two different tendencies:

$$\omega_i^2(T) = \omega_{0,i}^2 - aT + b(T_C - T)^{\beta} \quad \text{for} \quad (T_C > T) \tag{7}$$

$$\omega_i^2(T) = \omega_{0,i}^2 - aT \quad \text{for} \quad (T_C < T) \tag{8}$$

where T_C=150K (tetra/ortho transition temperature), a and b are constants and β is a critical parameter close to 0.5 for a linear dependence on pseudospin coordinates, and 0.5–1.0 for a quadratic dependence. The linear dependence is associated to interaction mainly via hydrogen bonding between MA cations and anionic sublattice. The second case with $\beta > 0.5$ relates to electrostatic interactions.

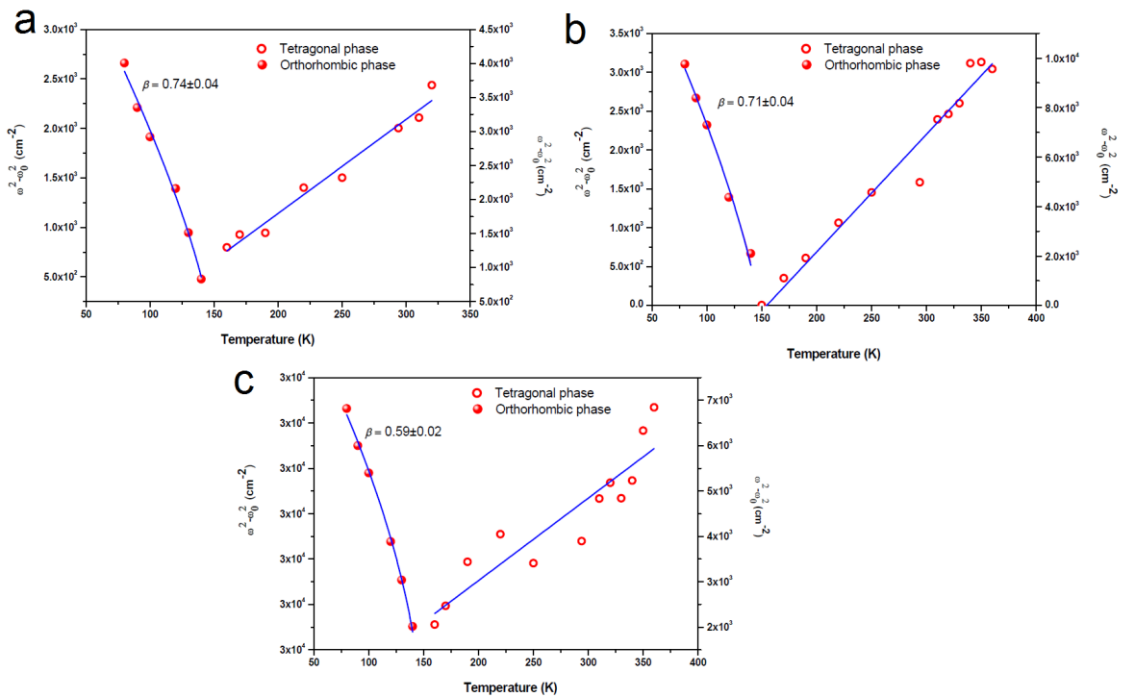

Figure 12. Temperature dependence of pseudospin coordinates of a) MA wagging mode; b) CH_3 sym. bending mode; c) NH_3 sym. bending mode. Full lines indicate results of fitting according to equation (7) in the orthorhombic phase and (8) in the tetragonal phase.

The temperature dependence of the square wavenumber for the MA wagging mode is reported in Figure 12a. It can be seen that for the NH_3 bending mode (Figure 12c) the parameter β has a lower value with comparison to the CH_3 bending mode (Figure 12b) and the MA wagging mode. It is possible that the ordering of the cation is more H-bond driven at the NH_3-end of the MAPI. Considering that the average value for the critical parameter β is 0.68±0.08, the increase in H-bond strength is probably not the only contribution in the ordering of the MAPI which is consistent with the medium-strong H-bond. Further electrostatic interaction could be at play such as interaction between the dipoles of two neighboring MA enabled by iodine vacancies.[63] Fitting the data across the tetragonal phase results in a straight line behavior in agreement with the model as presented in Figure 12.

3.6. Photoinduced Infrared Absorption

The evidence of strong anharmonicity and anomalous behavior of certain phonon modes with temperature and its implication to electron-phonon coupling was discussed in Section 3.4. Further investigation into the existence of polarons was performed by measuring the steady state photoinduced infrared absorption (PIA) of the MAPI. The theoretical background and experimental setup for the PIA are described in the Appendix section. By photoinducing charges in the material and measuring the IR absorption spectra, the coupling of the free careers with the lattice can be measured.[64] The photogeneration of electron-hole pairs could eventually distort the lattice around the photoinjected charges, which in turn might give rise to a modification of the electronic structure.[65] This experimental method allows the detection of only long lived photoexcited species, with lifetime in the order of milliseconds.

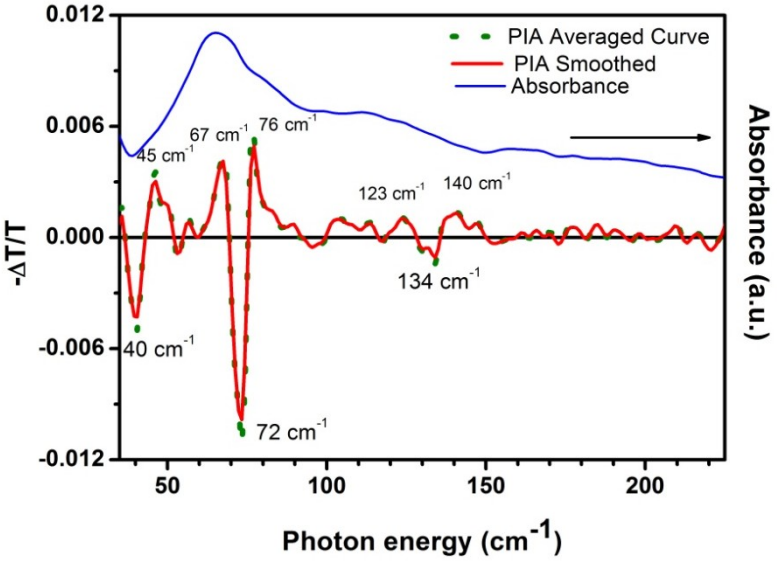

Figure 13. PIA spectrum of MAPI at 295K (red line); Absorption spectrum of MAPI at 295K (black line)

The bleaching of normal vibrations and appearance of new bands, which in general could be present in the Raman spectra (due to braking of symmetry, modification of the IR selection rules might surface), will arise due to the photogenerated polaronic distortion in the lattice as evidenced in many cuprate perovskites and $BaBiO_3$.[65,66] However, from the symmetry of the MAPI, it is well known and experimentally evidenced from Section 3.1. and 3.2. in this chapter, that all normal vibration are both IR and Raman active. Nevertheless, any appearance of new bands in the PIA spectra can be discussed in consideration of polaronic signature.

The PIA measurements are not trivial to perform. The penetration depth of the photons in the visible and the IR is quite different, thus in order to make sure that the entire film is photoexcited it is essential to work with samples of relatively small thickness (less than 300 μm). Furthermore the laser power needs to be sufficiently low in order not to heat up the sample or to photodegrade it. Considering these experimental constrictions the PIA spectra of MAPI was performed at RT and the measurement is presented in Figure 13.

From Figure 13 it is evident that several characteristic features are present. An evident bleaching of at two modes accompanied with the appearance of at least 4 absorption peaks. As a result of the charge-lattice coupling, change in energy of IR active modes of the undistorted lattice due to the charge-lattice interaction will cause bleaching of the peaks (reduction of oscillator strength) corresponding to the bare phonon, and the appearance of peaks of the lattice vibration at the distorted site. The observation of bleaching in the PA spectrum can also be associated with a screening effect associated with the photogeneration of mobile carriers. The two bleached modes can been associated to the Pb-I vibrations in the orthorhombic phase (Section 3.1). The band appearing at 45 cm^{-1} can be associated to a band reported at 47 cm^{-1} in the orthorhombic phase, while the bands at 67 cm^{-1} and 76 cm^{-1} have not been assigned or observed neither in the IR or the Raman spectra, but it has been proposed from computational data that they lie in the lattice vibrational region.[11,32] The modes at 123 and 140 cm^{-1} are very close to modes at 124 and 142 cm^{-1} assigned to the MA librational modes in the orthorhombic. Thus, there are at least several photoinduced bands at room temperature that correspond to IR active vibrations of the orthorhombic phase, suggesting that the lattice deformation around the carriers is

similar to the low temperature phase. The observed modes are clear indication of presence of polaronic behavior.[67]

A signal that could be interpreted as photodeformation was detected form the PIA measurement 170K. The spectra reported in Figure 14 do not correspond to the typical PIA representation, where the ratio of laser on vs. laser off spectra are reported showing the changes that occurs between two equilibrium conditions with and without photoinduced carriers (during the illumination the photogenerated carriers are constant and decay completely when laser is turned off). In this case, the spectra are obtained by comparing the spectra after different laser exposure time (in steps of 10 minutes of irradiation) with the one collected before illumination. Namely, as presented in Figure 14 several large bands appear to increase in intensity with exposure time, at 150, 200 and 230 cm^{-1} indicating a phototransformation of a relatively large part of the investigated material. The phototransformation could be a result of an irreversible degradation of the sample due to heating effects, however, when the temperature of the sample was increased by 20K to 190K, the phototransformation effect disappeared and the PIA spectral response returned to the initial form. This result is quite peculiar since the intensity of the photoinduced changes is around 20%. The observed photoinduced transformation can have great implication on the solar cell properties, thus further extended investigations are essential in yet another phenomenon of the MAPI.

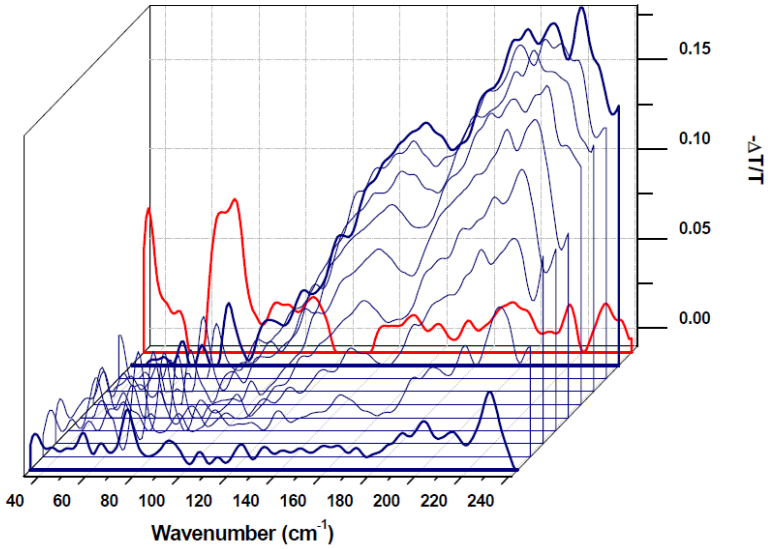

Figure 14. PIA spectra of MAPI with time at 170K (black line); PIA spectrum of MAPI at 190K (red line).

4. Conclusion

Understanding the role of the cation motion and vibrational response of the MAPI can ensure essential knowledge of the connection between the structural optical and electronic properties. Although the advances in computational methods have extreme value for probing the physical peculiarities of this unique perovskite system, experimental data are indispensable in forming a full physical image. The IR and Raman spectra throughout the 3 crystalline phases of the MAPI are recorded, and assignments of vibrational modes have been made in very good correlation with the simulations. The relaxation times of relevant cation modes should fulfill the understanding of the vibrational response of the material which could be linked with the material electronic properties and device physics. From both IR and Raman spectra vs. temperature there are evidences of medium to strong H-bond only in the orthorhombic phase; H-bond is responsible for the increase of the spontaneous polarization and the possible onset of ferroelectricity in the ortho phase. The PIA measurements clearly indicate the presence of polarons in the tetragonal phase of MAPI as was observed in many other perovskite materials. The strong anharmonicity of most of the phonon modes and phonon-phonon interaction can strongly influence the characteristics and behavior of polarons. Polarons, as reported by Juarez-Perez *et al.,*[68] are associated with a large dielectric constant that acts in screening Coulomb attraction and consequently reducing the recombination of photogenerated carriers. It is clear that investigating the vibrational spectroscopy response of the hybrid perovskite materials provides fundamental input to the physical interaction governing the charge transport and recombination. Furthermore, the intriguing results of MAPI phototransformation suggests that the complete understanding of the dynamical process and the device physics are still missing, thus providing a fruitful field for extended research.

5. Bibliography

1. Snaith, H. J. Perovskites: The Emergence of a New Era for Low-Cost, High-Efficiency Solar Cells. *J. Phys. Chem. Lett.* **4,** 3623–3630 (2013).
2. Park, N.-G. Perovskite solar cells: an emerging photovoltaic technology. *Mater. Today* **18,** 65–72 (2015).
3. Zhu, X.-Y. & Podzorov, V. Charge Carriers in Hybrid Organic–Inorganic Lead Halide Perovskites Might Be Protected as Large Polarons. *J. Phys. Chem. Lett.* **6,** 4758–4761 (2015).
4. La-o-vorakiat, C. *et al.* Phonon Mode Transformation Across the Orthohombic–Tetragonal Phase Transition in a Lead Iodide Perovskite $CH_3NH_3PbI_3$: A Terahertz Time-Domain Spectroscopy Approach. *J. Phys. Chem. Lett.* **7,** 1–6 (2016).
5. Mosconi, E., Amat, A., Nazeeruddin, M. K., Grätzel, M. & De Angelis, F. First-principles modeling of mixed halide organometal perovskites for photovoltaic applications. *J. Phys. Chem. C* **117,** 13902–13913 (2013).
6. Quarti, C., Mosconi, E. & De Angelis, F. Interplay of Orientational Order and Electronic Structure in Methylammonium Lead Iodide: Implications for Solar Cells Operation. *Chem. Mater.* **26,** 6557–6569 (2014).
7. Mosconi, E., Quarti, C., Ivanovska, T., Ruani, G. & De Angelis, F. Structural and electronic properties of organo-halide lead perovskites: a combined IR-spectroscopy and ab initio molecular dynamics investigation. *Phys. Chem. Chem. Phys.* **16,** 16137 (2014).
8. Motta, C. *et al.* SI: Revealing the role of organic cations in hybrid halide perovskite $CH_3NH_3PbI_3$. *Nat. Commun.* **6,** 7026 (2015).
9. Onoda-Yamamuro, N., Matsuo, T. & Suga, H. Calorimetric and IR spectroscopic studies of phase transitions in methylammonium trihalogenoplumbates (II)†. *J. Phys. Chem. Solids* **51,** 1383–1395 (1990).
10. Glaser, T. *et al.* Infrared Spectroscopic Study of Vibrational Modes in Methylammonium Lead Halide Perovskites. *J. Phys. Chem. Lett.* **6,** 2913–2918 (2015).
11. Pérez-Osorio, M. A. *et al.* Vibrational Properties of the Organic–Inorganic Halide Perovskite $CH_3NH_3PbI_3$ from Theory and Experiment: Factor Group Analysis, First-Principles Calculations, and Low-Temperature Infrared Spectra. *J. Phys. Chem. C* **119,** 25703–25718 (2015).
12. Quarti, C. *et al.* SI: The Raman Spectrum of the $CH_3NH_3PbI_3$ Hybrid Perovskite: Interplay of Theory and Experiment. *J. Phys. Chem. Lett.* **5,** 279–284 (2014).
13. Grancini, G. *et al.* The Impact of the Crystallization Processes on the Structural and Optical Properties of Hybrid Perovskite Films for Photovoltaics. *J. Phys. Chem. Lett.* **5,** 3836–3842 (2014).
14. Park, B. *et al.* Resonance Raman and Excitation Energy Dependent Charge Transfer Mechanism in Halide-Substituted Hybrid Perovskite Solar Cells. *ACS Nano* **9,** 2088–2101 (2015).
15. Gottesman, R. *et al.* Photoinduced Reversible Structural Transformations in Free-Standing $CH_3NH_3PbI_3$ Perovskite Films. *J. Phys. Chem. Lett.* **6,** 2332–2338 (2015).
16. Lee, J.-H., Bristowe, N. C., Bristowe, P. D. & Cheetham, A. K. Role of hydrogen-bonding and its interplay with octahedral tilting in $CH_3NH_3PbI_3$. *Chem. Commun.* **51,** 6434–6437 (2015).
17. Stroppa, A., Quarti, C., De Angelis, F. & Picozzi, S. Ferroelectric Polarization of $CH_3NH_3PbI_3$: A Detailed Study Based on Density Functional Theory and Symmetry Mode Analysis. *J. Phys. Chem. Lett.* **6,** 2223–2231 (2015).
18. Zhang, H. *et al.* Photovoltaic behaviour of lead methylammonium triiodide

perovskite solar cells down to 80 K. *J. Mater. Chem. A* **3,** 11762–11767 (2015).
19. Milot, R. L., Eperon, G. E., Snaith, H. J., Johnston, M. B. & Herz, L. M. Temperature-Dependent Charge-Carrier Dynamics in $CH_3NH_3PbI_3$ Perovskite Thin Films. *Adv. Funct. Mater.* **25,** 6218–6227 (2015).
20. Wasylishen, R. E., Knop, O. & Macdonald, J. B. Cation rotation in methylammonium lead halides. *Solid State Commun.* **56,** 581–582 (1985).
21. Lee, M. M., Teuscher, J., Miyasaka, T., Murakami, T. N. & Snaith, H. J. Efficient Hybrid Solar Cells Based on Meso-Superstructured Organometal Halide Perovskites. *Science.* **338,** 643–647 (2012).
22. Noh, J. H., Im, S. H., Heo, J. H., Mandal, T. N. & Seok, S. Il. Chemical Management for Colorful, E ffi cient, and Stable Inorganic − Organic Hybrid Nanostructured Solar Cells. **2,** 28–31 (2013).
23. Suarez, B. *et al.* Recombination Study of Combined Halides (Cl, Br, I) Perovskite Solar Cells. *J. Phys. Chem. Lett.* **5,** 1628–1635 (2014).
24. Weber, D. $CH_3NH_3PbX_3$, a Pb(II)-System with Cubic Perovskite Structure. *Zeitschrift für Naturforsch.* **33b,** 1443–1445 (1978).
25. Poglitsch, A. & Weber, D. Dynamic disorder in methylammoniumtrihalogenoplumbates (II) observed by millimeter-wave spectroscopy. *J. Chem. Phys.* **87,** 6373 (1987).
26. Oku, T. *Solar Cells - New Approaches and Reviews*. (InTech, 2015). doi:10.5772/58490
27. Ball, J. M., Lee, M. M., Hey, A. & Snaith, H. J. Low-temperature processed meso-superstructured to thin-film perovskite solar cells. *Energy Environ. Sci.* **6,** 1739 (2013).
28. Yu, H. *et al.* The Role of Chlorine in the Formation Process of '$CH_3NH_3PbI_{3-x}$ Cl_x' Perovskite. *Adv. Funct. Mater.* n/a–n/a (2014). doi:10.1002/adfm.201401872
29. Wu, X. *et al.* Trap States in Lead Iodide Perovskites. *J. Am. Chem. Soc.* **137,** 2089–2096 (2015).
30. D'Innocenzo, V. *et al.* Excitons versus free charges in organo-lead tri-halide perovskites. *Nat. Commun.* **5,** 3586 (2014).
31. Glaser, T. *et al.* SI Infrared Spectroscopic Study of Vibrational Modes in Methylammonium Lead Halide Perovskites. *J. Phys. Chem. Lett.* **6,** 2913–2918 (2015).
32. Ivanovska, T., Quarti, C., Grancini, G., Petrozza, A., De Angelis, F., Miliani, A., Ruani, G. Unpublished data. *Manuscr. under Prep.*
33. Waldron, R. D. The IR Specra of Three Solid Phases of Methyl Ammonium Chloride. *J. Chem. Phys.* **21,** 734–741 (1953).
34. Théorêt, A. & Sandorfy, C. The infrared spectra of solid methylammonium halides—II. *Spectrochim. Acta Part A Mol. Spectrosc.* **23,** 519–542 (1967).
35. Varma, V., Bhattacharjee, R., Vasan, H. N. & Rao, C. N. R. Infrared and Raman spectroscopic investigations of methylammonium haloantimonates(III), $[N(CH_3)_4{-}nH_n]_3Sb_2X_9$ (n =0–3, X=Cl or Br), through their phase transitions. *Spectrochim. Acta Part A Mol. Spectrosc.* **48,** 1631–1646 (1992).
36. Bator, G., Jakubas, R. & Baran, J. Vibrational study of the structural phase transitions in the $(CH_3ND_3)_3Sb_2Br_9$ (d-MABA) crystals by infrared spectroscopy. *Vib. Spectrosc.* **25,** 101–113 (2001).
37. Maalej, A. *et al.* Phase transitions and crystal dynamics in the cubic perovskite $CH_3NH_3PbCl_3$. *Solid State Commun.* **103,** 279–284 (1997).
38. Mączka, M., Ptak, M. & Macalik, L. Infrared and Raman studies of phase transitions in metal–organic frameworks of $[(CH_3)_2NH_2][M(HCOO)_3]$ with M=Zn, Fe. *Vib. Spectrosc.* **71,** 98–104 (2014).
39. Tarasiewicz, J., Jakubas, R. & Baran, J. Infrared studies of phase transitions in

ferroelectric $(C_5H_5NH)_5Bi_2Br_{11}$. *Vib. Spectrosc.* **40,** 55–65 (2006).
40. Prasad, P. S. R. & Bist, H. D. Vibrational spectroscopic study of the structural phase transitions in Perovskite layer compounds $(CH_3NH_3)_2CdCl_4$. *J. Phys. Chem. Solids* **50,** 1033–1040 (1989).
41. Carpentier, P., Lefebvre, J. & Jakubas, R. Raman studies of the ferroelectric phase transitions in $(CH_3NH_3)_5Bi_2Cl_{11}$ (MAPCB). I. The internal vibrations of the methylammonium cation. *J. Phys. Condens. Matter* **4,** 2985–2999 (1992).
42. Yadav, R. *et al.* Dielectric and Raman investigations of structural phase transitions in $(C_2H_5NH_3)_2CdCl_4$. *Phys. Chem. Chem. Phys.* **17,** 12207–12214 (2015).
43. Quarti, C. *et al.* Structural and optical properties of methylammonium lead iodide across the tetragonal to cubic phase transition: implications for perovskite solar cells. *Energy Environ. Sci.* 2–8 (2016). doi:10.1039/C5EE02925B
44. Ledinský, M. *et al.* Raman Spectroscopy of Organic–Inorganic Halide Perovskites. *J. Phys. Chem. Lett.* **6,** 401–406 (2015).
45. Mashiyama, H., Kawamura, Y., Magome, E. & Kubota, Y. Displacive Character of the Cubic-Tetragonal Transition in $CH_3NH_3PbX_3$. *J. Korean Phys. Soc.* **42,** 1026–1029 (2003).
46. Stoumpos, C. C., Malliakas, C. D. & Kanatzidis, M. G. Semiconducting Tin and Lead Iodide Perovskites with Organic Cations: Phase Transitions, High Mobilities, and Near-Infrared Photoluminescent Properties. *Inorg. Chem.* **52,** 9019–9038 (2013).
47. Lucazeau, G. Effect of pressure and temperature on Raman spectra of solids: anharmonicity. *J. Raman Spectrosc.* **34,** 478–496 (2003).
48. Carabatos-Nédelec, C. & Becker, P. Order-disorder and structural phase transitions in solid-state materials by Raman scattering analysis. *J. Raman Spectrosc.* **28,** 663–671 (1997).
49. da R. Andrade, P. & Porto, S. P. S. On linewidth of phonons associated to a disorder mechanism. *Solid State Commun.* **13,** 1249–1254 (1973).
50. Onoda-Yamamuro, N., Matsuo, T. & Suga, H. Dielectric study of $CH_3NH_3PbX_3$ (X = Cl, Br, I). *J. Phys. Chem. Solids* **53,** 935–939 (1992).
51. Srinu Bhadram, V., Rajeswaran, B., Sundaresan, A. & Narayana, C. Spin-phonon coupling in multiferroic RCrO 3 (R-Y, Lu, Gd, Eu, Sm): A Raman study. *EPL (Europhysics Lett.* **101,** 17008 (2013).
52. Gupta, R., Pai, G. V., Sood, A. K., Ramakrishnan, T. V. & Rao, C. N. R. Raman scattering in charge-ordered Pr 0.63 Ca 0.37 MnO 3 : Anomalous temperature dependence of linewidth. *Europhys. Lett.* **58,** 778–784 (2002).
53. Bakulin, A. a. *et al.* Real-Time Observation of Organic Cation Reorientation in Methylammonium Lead Iodide Perovskites. *J. Phys. Chem. Lett.* **6,** 3663–3669 (2015).
54. Leguy, A. M. a. *et al.* The dynamics of methylammonium ions in hybrid organic–inorganic perovskite solar cells. *Nat. Commun.* **6,** 7124 (2015).
55. Klemens, P. G. Anharmonic Decay of Optical Phonons. *Phys. Rev.* **148,** 845–848 (1966).
56. Pisoni, A. *et al.* Ultra-Low Thermal Conductivity in Organic–Inorganic Hybrid Perovskite $CH_3NH_3PbI_3$. *J. Phys. Chem. Lett.* **5,** 2488–2492 (2014).
57. Zhang, L., Ruesch, M., Zhang, X., Bai, Z. & Liu, L. Tuning thermal conductivity of crystalline polymer nanofibers by interchain hydrogen bonding. *RSC Adv.* **5,** 87981–87986 (2015).
58. Kussow, A.-G. Large Polaron in an Anharmonic Crystal Lattice. *Int. J. Mod. Phys. B* **23,** 19–38 (2009).
59. Mattoni, A., Filippetti, A., Saba, M. I. & Delugas, P. Methylammonium Rotational Dynamics in Lead Halide Perovskite by Classical Molecular Dynamics: The Role of

Temperature. *J. Phys. Chem. C* **119,** 17421–17428 (2015).
60. Fan, Z. *et al.* Ferroelectricity of $CH_3NH_3PbI_3$ Perovskite. *J. Phys. Chem. Lett.* **6,** 1155–1161 (2015).
61. Filippetti, A., Delugas, P., Saba, M. I. & Mattoni, A. Entropy-Suppressed Ferroelectricity in Hybrid Lead-Iodide Perovskites. *J. Phys. Chem. Lett.* 4909–4915 (2015). doi:10.1021/acs.jpclett.5b02117
62. Bator, G., Baran, J., Jakubas, R. & Sobczyk, L. The structure and vibrational spectra of some ferroelectric and ferroelastic alkylammonium halogenoantimonates(III) and bismuthates(III). *J. Mol. Struct.* **450,** 89–100 (1998).
63. Eames, C. *et al.* Ionic transport in hybrid lead iodide perovskite solar cells. *Nat. Commun.* **6,** 7497 (2015).
64. Calvani. Optical properties of polarons. **161,** 133–136 (1993).
65. Ruani, G. & Taliani, C. in *Igarss 2014* (ed. Nasu, K.) **124,** 63–71 (Springer Berlin Heidelberg, 1997).
66. Taliani, C., Pal, A. J., Ruani, G., Zamboni, R. & Masini, R. Evidence of charge localization from photoinduced infrared absorption in BaBiO3. *Bull. Mater. Sci.* **14,** 533–538 (1991).
67. Emin, D. Optical properties of large and small polarons and bipolarons. *Phys. Rev. B* **48,** 13691–13702 (1993).
68. Juarez-Perez, E. J. *et al.* Photoinduced Giant Dielectric Constant in Lead Halide Perovskite Solar Cells. *J. Phys. Chem. Lett.* **5,** 2390–2394 (2014).

CHAPTER V:
GENERAL CONCLUSIONS AND FUTURE OUTLOOK

The need to improve the solar cell technology is as ongoing as the energy consumption itself. The fundamental research in efficiency improvement of the photovoltaics is inseparably confronted by the idea of not only efficient but low-cost energy production. Even though the Sun is a free energy source, the industrialization and the advance of the solar cell technology rely on the manufacturing processes and components which utilize non renewable resources and materials. To this end, a continuing research has developed around the third generation photovoltaics in the past 20 years.

Employing low-cost and earth abundant materials, the organic and hybrid organic-inorganic solar cells have emerged as a low-cost and low-energy consumption production technology. However, despite the promising energy outlook this photovoltaic technology is still under fundamental material and device research in order to get closer, efficiency and stability wise, the authority of the crystalline silicon solar cells.

The work presented in the thesis is focused on precisely this type of fundamental investigation of both device optimization and material studies; from the dye sensitized solar cell to the perovskite solar cells. The basic research outline can be divided in two main subjects, the dye sensitized solar cell optimization and the material investigation and optimization of perovskite solar cells.

The first part of the research was focused on improving and optimizing the photoanode mesoporous TiO_2 films by improving the electron transport through improving the electron-hole separation and reducing the recombination. Two efficient methods for photoanode optimization were proposed and implemented. The employment of a TiO_2 colloidal nanoparticle solution as a photoanode post-treatment was found to increase the power conversion efficiency of the solar cell for 10%, thus granting the possibility of utilization of this post-treatment method vs. the application of $TiCl_4$. The obtained results of the photoanode and solar cell characterization indicate that the post-treatment is successfully reducing the electron recombination through shallow trap states, which in turn is beneficial for the electron transport through the TiO_2.

Further investigation of the mechanisms for electron transport enhancement through the mesoporous TiO_2, lead to the construction of composite SWCNT/TiO_2 photoanodes. The composite photoanodes were investigated with respect to the SWCNT loading and employed in three different solar cell architectures (dye sensitized, solid state dye sensitized, and perovskite solar cells). It was found that the conductivity of the photoanodes increased by two orders of magnitude, however specific mechanical and electronic properties prevent the translation of this conductivity enhancement to efficiency enhancement in a solar cell configuration. The possibility of the SWCNT to act as recombination centers, the Fermi level equilibration and the influence of the metallic nanotubes are all discussed as possible foes behind the observed relatively low efficiency improvement.

Nevertheless, a trend of enhancement of the short circuit current for solar cell employing composite photoanodes with low SWCNT loadings (around 0.1% SWCNT/TiO_2) was confirmed for all solar cell types. The highest efficiency improvement was obtained for dye sensitized solar cells (both with liquid and solid electrolyte) when the composite electrodes were also submitted to the TiO_2 colloidal nanoparticle solution post-treatment.

These two methods of photoanode improvement had the strongest effect on the efficiency increment for the solid state dye sensitized solar cell, whereas for the perovskite solar cell, a trend of the composite photoanode performance enhancement was evident only for cells with good perovskite coverage (overlayer formation due to huger concentration of perovskite solution).

The evolution of the perovskite solar cells in recent years ignited the research interest in both the solar cell and the perovskite material itself. The investigation of different perovskite solar cell architectures is presented with the focus on the optimization and degradation of planar perovskite solar cells. The results of extensive optimization were presented, highlighting a mechanism of O_2 curing involving the MAPI which inevitably leads to high solar cell efficiencies of more than 10%, with best cells around 12%. Furthermore, the investigation was parallely performed on solar cells employing a high and low temperature processed TiO_2 compact layer. The initial results obtained show that the low temperature processing of the compact layer is constraining neither the efficiency, nor the stability of the solar cells.

One of the main contributions for the optimization of the perovskite solar cells and its stability could very well prove to be the physical understanding of the fundamental kinetic and dynamic charge interactions and material properties.

To be able to look deeper into the fundamental properties of the MAPI and answer the ongoing questions of superior electronic and charge transport properties, a full vibrational study of all the phases of the MAPI was performed. Detailed analysis of the anharmonic properties (with respect to phonon and charge interactions) was presented and analysis of the cation dynamic was obtained. A strong evidence of polaronic behavior was observed which could prove to be the answer to the above mentioned questions. The $CH_3NH_3PbI_3$ belongs to a group of hybrid organic-inorganic perovskite materials which opens a wide possibility of structure manipulation with the aim of tailoring the material properties. Exchanging the cation, as well as the metal or halide ion, results in the change of electronic properties which can be appropriately harvested, which means that the acquired results on the order-disorder dynamics of the MA cation, probing the strength of the H-bond which in turn implies interactions with the PbI_6 framework and its distortion, is of fundamental importance.

Considering the youth of the perovskite solar cell technology, the presented research lines are all under more extensive and ongoing research. Further insight into the mechanism behind the O_2 curing effect can have great implication on the device optimization and its stability, additionally the equivalency of both low and high temperature processed perovskite solar cells can not only introduce wider implementation of the perovskite solar cell technology, but additionally reduce the production cost.

Finally, the understanding of the underlining physical processed behind the charge generation and transport in the MAPI should prove essential for material modification and chemical tailoring to suit the appropriate devise structure and application.

APPENDIX

1. Research Methods and Techniques

The material and device preparation are presented in each chapter with regard to a concrete experiment. However, despite various experimental techniques for the study of both material and device properties, several techniques were applied and studied more extensively. The next section provides a more detailed description of the theoretical boarhound of the main research techniques employed for the solar cell and material investigation.

1.1. Electrical Characterization of Solar Cells

1.1.1. Current –Voltage Characterization

The main characterization technique of any type of solar cell is the measurement of the current-voltage (*I-V*) curve. When the cell is connected to variable resistance, an ampermeter measures the current running through the circuit and a voltmeter measures the voltage at the contacts of the cell. A typical *I-V* curve is presented in Figure 1a.

The short circuit current I_{SC} is the current generated when the cell contacts are connected (short circuited), meaning that the potential difference between them is zero and the resistance in the cell zero. If a cell has high efficiency meaning that the series resistance and saturation current are negligible and the shunt resistance is high, then according to equation (4) in Chapter I:

$$I_{SC} \approx I_{ph} \tag{1}$$

If we change the value of the resistance between zero and infinity the current and the voltage will change between the I_{SC} and 0 and 0 and V_{OC}, respectively. The power output of the solar cell which is defined as $P = IV$ will take on values which will change with the change of the current and voltage. At a certain point the power will have a maximum value which will correspond to a certain maximum power point current I_{mpp} and maximum power point voltage V_{mpp}. As a result of this physical behavior an important solar cell parameter is defined:

$$FF = \frac{I_{mpp}V_{mpp}}{I_{SC}V_{OC}} \tag{2}$$

This parameter is called fill factor *FF* and it's a nondimensional unit which maximum value is 1 and it's usually expressed in percent. The fill factor changes with the change in the series and shunt resistance. Niamey, a smaller series resistance and a higher shunt resistance result in higher *FF*. The increase in the fill factor results in a more "square" form of the *I-V* curve. The change in the form of the *I-V* curve with the change in series and shunt resistance is presented in Figure 1b and c.

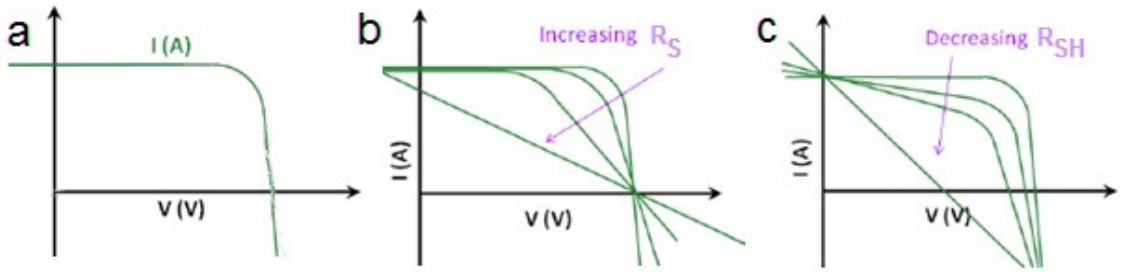

Figure 1. a) Typical Current-Voltage (*I-V*) curve of a solar cell; b) Influence of the increasing the series resistance R_S on the *I-V* characteristic and *FF*; c) Influence of the increasing the series resistance R_{SH} on the *I-V* characteristic and *FF*.

The solar cell efficiency of conversion of solar to electrical energy η, or also denoted in literature as power conversion efficiency (PCE), is defined as the relationship between the power output of the cell and the intensity of the incident light on the active surface of the solar cell:

$$\eta = \frac{P_m}{E \cdot A} \tag{3}$$

where P_m is the maximum power output, A is the active (illuminated) area of the solar cell and E is the incident light. The efficiency of the solar cell depends on multiple factors and accounts for all the losses that occur within the solar cell due to reflection, recombination, series resistance ect.[1,2]

When representing current-voltage plots of solar cells usually instead of the current, the current density is displayed, additionally since certain solar cell technologies such as the perovskite solar cells have a current-voltage response which is sensitive on the scan rate and direction; it is common practice to report on these values as well. The current voltage measurement is mainly performed under illumination; however the *I-V* response in dark conditions can also provide information on the series and shunt resistance of the solar cell.

1.1.2. Open Circuit Voltage Decay

Open circuit voltage decay (OCVD) is a large perturbation technique used in determination of electron lifetime in nanocrystalline dye sensitized solar cells. It is a steady state measurement that provides continuous reading of the electron lifetime as a function of the V_{OC}. Upon illumination of a solar cell which is kept at open circuit, the free electron density in the photoanode is affected by electron injection into the conduction band of the titania and recombination of the photogenerated electrons with the electrolyte.[3,4] When the illumination is interrupted the decay of the V_{OC} is recorded. The OCVD technique is practically a dark measurement, meaning that the recombination with the dye in not registered. Additionally it is important to point out that OCVD measurement time frame in liquid DSC is quite long (>50 ms) so only information on the recombination of the electrons with the oxidized electrolyte is measured. Electron lifetime measured by OCVD considers not only the trapping/detrapping events in the semiconductor but also the different possibilities for interfacial charge transfer.

The electron density n of the nanocrystalline photoanode increases with photogeneration of electrons, and decreases by recombination at a rate $U(n)$. The decay of the electron density is therefore defined as:

$$\frac{dn}{dt} = -U(n) \tag{4}$$

thus, the electron lifetime is:

$$\tau_n^{-1} = -\frac{1}{n}\frac{dn}{dt}. \tag{5}$$

Under stationary conditions the V_{OC} can be written as:

$$V_{OC} = \frac{kT}{q}\ln\left(\frac{n}{n_0}\right) \tag{6}$$

From the previous two equations the electron lifetime is:

$$\tau_n = -\frac{k_b T}{e}\left(\frac{dV_{oc}}{dt}\right)^{-1} \tag{7}$$

where k_b is the Boltzmann , T is the absolute temperature and e is the elementary electrical charge. Employing equation (7) the electron lifetime can be directly extracted from the measurement of the decay of the V_{OC}.[3]

1.2. Vibrational Spectroscopy of Materials

Raman and Infrared (IR) spectroscopy are vibrational spectroscopy techniques which investigate the vibrational, rotational and other low-frequency modes of a system. These well established techniques study the molecular structures of organic and inorganic materials. Depending on the nature of the vibration, which is determined by the symmetry of the molecule or crystal, vibrations may be active in the infrared and or in the Raman or silent. These techniques represent a powerful tool not only in determining the material structure but moreover, analyzing the vibrational modes evolution through their linewidth, position and intensity, by changing certain structural or environmental parameters, the IR and Raman spectroscopy can be used to extract various intrinsic information of the analyzed material.[5] The vibrational response of the material can provide very useful data on the crystalline size; relaxation time of modes which in turn relies on rotational dynamics; and anharmonic contributions such as phonon-phonon, electron-phonon and spin-phonon interactions.

1.2.1. Raman Spectroscopy

When monochromatic light is falls on a molecule or a crystal, the incident photons get scattered, absorbed or transmitted. The most probable scattering process will be elastic scattering where the photon doesn't change its energy and this is called Rayleigh scattering. However, only a small percent of scattered photons (usually 1 in 10^7) will undergo inelastic scattering and the scattered light will be shifted in frequency from the incident light. This scattering process is called Raman scattering.

In quantum mechanical terms when a photon of energy hv_0 gets absorbed by the material it excites the molecule to an virtual state (different from any stationary state) which after relaxation reemits a photon with the same energy and returns to the original (ground) state, thus Rayleigh scattering is observed. However, when photon absorption results in an excitation from ground (or first vibrational) state to a virtual state, and after a relaxation time of around 100 fs a photon is emitted with a different energy from the initial one, Raman scattering is observed. A schematic energy diagram of the scattering processes is represented in Figure 2.

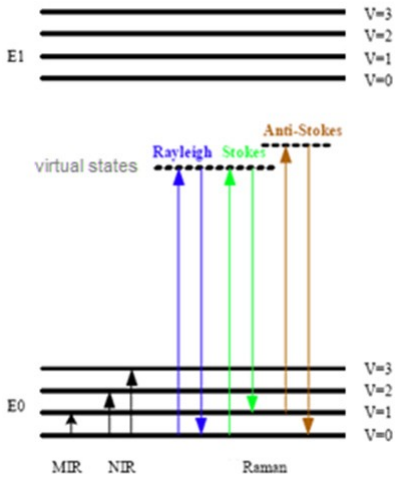

Figure 2. Schematic representation of vibrational and virtual energy levels and description of photon absorption and emission energies for IR and Raman scattering mechanisms.

If excitation occurs from the ground state which at room temperature is heavily populated the relaxation process will return the molecule to the first vibrational state and the emitted photon will have energy $h(v\text{-}v_m)$. These Raman lines are more intense due to the higher probability that system was initially in the ground state, and are called Stokes. However, since some molecules will initially be in the first vibrational state, after the absorption of the incident photon they will relax into ground state through the emission of a photon of energy $h(v+v_m)$, these Raman lines are called anti-Stokes.[6]

1.2.2. Infrared Spectroscopy

The IR spectroscopy is based on the absorption of IR light. The interaction of infrared radiation with a vibrating molecule is possible only if, due to the interaction with the electromagnetic wave, the first derivative of the dipole moment with respect to normal vibrational coordinates is different from zero :

$$\left(\frac{\partial P}{\partial q}\right) \neq 0 \qquad (8)$$

which results in an IR active mode.[5,6]

When a photon of certain energy gets absorbed is excites the molecule from the ground to an excited vibrational state, where the frequency of the absorption bands is proportional to the difference between the vibrational ground and excited states $v_m=v_1\text{-}v_0$ (see Figure 2).

1.2.3. Photoinduced Infrared Absorption (PIA)

PIA represents a measurement of photoinduced changes in the infrared absorbance spectra. The continuous wave PIA can give information on reversible short time photogenerated phase transformations and strong electron-phonons interactions i.e. polarons. The measurement principle is based on recording the transmission spectra with and without laser illumination of the sample using a stabilized Fourier transform infrared spectrometer.[7,8] A scheme of the experimental setup is presented in Figure 3.

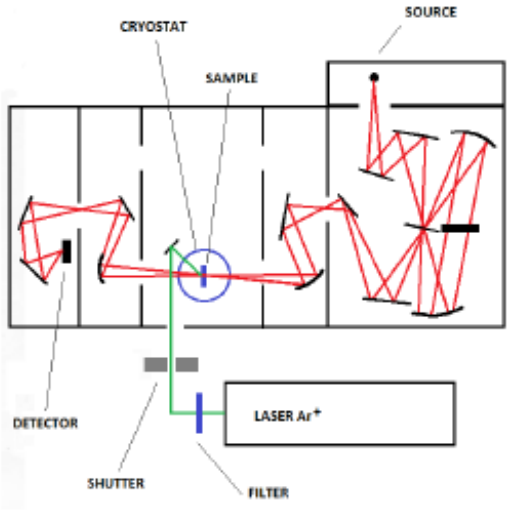

Figure 3. Schematic of a PIA measurement setup.

Experimentally a relatively low laser power density is used to avoid thermal effects and long spectral series of IR measurements with the laser ON/OFF are performed, in order to obtain high signal/noise ratio reducing possible drift of the experimental apparatus response. The measurement is carried out by acquiring the subsequent ON/OFF (laser illumination) absorption spectra ($I_{OFF1}(\omega)$-$I_{ON1}(\omega)$-$I_{OFF2}(\omega)$-$I_{ON2}(\omega)$-$I_{OFF3}(\omega)$-$I_{ON3}(\omega)$-....). The PIA measurements are afterwards processed:

$$I_{OFF}(\omega) = \sum I_{OFFi}(\omega); \qquad I_{ON}(\omega) = \sum I_{ONi}(\omega) \tag{9}$$

And the photoinduced spectra are presented as a fractional variation of the transmittance due to photoinduction:

$$-\Delta T(\omega)/T(\omega) = I_{OFF}(\omega)/I_{ON}(\omega) - 1 \tag{10}$$

1.3. Light Induced Scanning Techniques

Light induces scanning techniques are based on interaction of photons with the material forming signals such as photoluminescence and laser beam induced photocurrent.

1.3.1. Laser Scanning Confocal Microscopy

Laser Scanning Confocal Microscopy (LSCM) allows the selective investigation of the morphology of the active layer in working devices. The spatially resolved photoluminescence (PL) rises from the photons emitted by radioactive recombination.[9] In the LSCM, illumination and detection are confined to a single, diffraction-limited, point in the specimen, a small focal volume within, or on the surface of the material. Working in confocal configuration means the detected emission signal from the excited material is acquired through a pinhole, which is blocking all the out of focus light. The detected light represents a pixel in the digitally transformed image. Scanning across the sample, a map of the area (collection of pixels) can be constructed. The final resolution achieved by the instrument is governed by the wavelength of light, the objective lenses, and the properties of the specimen itself.[10] A scheme of the light path in LSCM is presented in Figure 4.

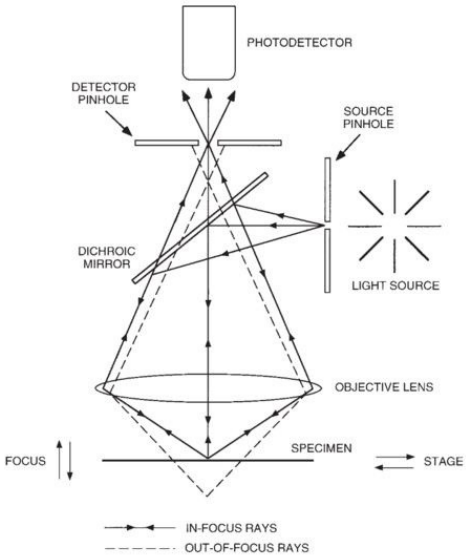

Figure 4. The light path in LSCM mesurement[10]

1.3.2. Laser Beam Induced Photocurrent

Laser Beam Induced Photocurrent (LBIC) enables us to analyze the morphology of the active layer through its charge generation, separation and transport efficiency, by the means of mapping the intensity of the photocurrent over the cell surface. A schematic of an LBIC measurement setup is presented in Figure 5. The obtained maps are used for localization and qualitative as well as quantitative classification of local defects existing in the solar cell structure. The measurement principle is based on point by-point scanning of a focused monochromatic light beam across the surface of the device under test, which is held under short-circuit conditions. Photon absorption of the incident light leads to generation of a photocurrent, which is then registered. This technique can reveal the electrical barriers within the working devices and real electrical defects within the active layer, which can be correlated with the parameters of the working device.[9,11] The comparison between the LSCM and LBIC provides a relationship between the sub-micrometric morphological features of the active layer and the local photovoltaic response of the device.

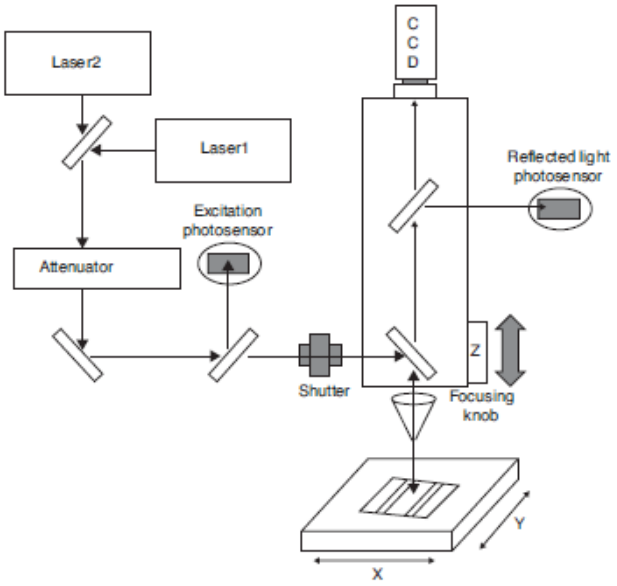

Figure 5. Schematic of a LBIC measurement setup[9]

2. Bibliography

1. Nelson, J. in *The Physics of Solar Cells* 1–16 (Imperial College Press (Distributed by World Scientific Publishing Co.), 2003). doi:10.1142/9781848161269_0001
2. Wurfel, P. in *Physics of Solar Cells* 109–136 (Wiley-VCH Verlag GmbH). doi:10.1002/9783527618545.ch6
3. Zaban, A., Greenshtein, M. & Bisquert, J. Determination of the Electron Lifetime in Nanocrystalline Dye Solar Cells by Open-Circuit Voltage Decay Measurements. *ChemPhysChem* **4,** 859–864 (2003).
4. Bisquert, J., Zaban, A., Greenshtein, M. & Mora-Serot, I. Determination of Rate Constants for Charge Transfer and the Distribution of Semiconductor and Electrolyte Electronic Energy Levels in Dye-Sensitized Solar Cells by Open-Circuit... *J. Am. Chem. Soc.* **126,** 13550–13559 (2004).
5. Schrader, B. *Infrared and Raman Spectroscopy-Methods and Applications*. *Infrared and Raman Spectroscopy - Methods and Applications* (1995). doi:10.1016/0924-2031(00)00065-5
6. Larkin, P. J. *'IR and Raman Spectroscopy - Principles and Spectral Interpretation'. Vasa* (2011). doi:10.1016/b978-0-12-386984-5.10001-1
7. Mihailovic, D. in *Polarons in Advanced Materials* 547–567 (Springer Netherlands, 2007). doi:10.1007/978-1-4020-6348-0_13
8. Taliani, C., Pal, A. J., Ruani, G., Zamboni, R. & Masini, R. Evidence of charge localization from photoinduced infrared absorption in BaBiO3. *Bull. Mater. Sci.* **14,** 533–538 (1991).
9. Seeland, M., Rösch, R. & Hoppe, H. in *Stability and Degradation of Organic and Polymer Solar Cells* 39–70 (John Wiley & Sons, Ltd, 2012). doi:10.1002/9781119942436.ch3
10. Paddock, S. W. in *Confocal Microscopy* 1–34 (Humana Press). doi:10.1385/1-59259-722-X:1
11. Holt, D. B. & Yacobi, B. G. Extended Defects in Semiconductors: Electronic Properties, Device Effects and Structures. **3,** 2009–2010 (2007).